

This work is licensed under a Creative Commons Attribution 4.0 International License

<https://creativecommons.org/licenses/by/4.0/>



# **Lipid-based drug delivery systems for inflammatory and fibrosis therapies**

Inaugural dissertation  
of the Faculty of Science,  
University of Bern

presented by

Marianna Carone

from Italy

Supervisor of the doctoral thesis:  
Prof. Dr. Paola Luciani

Department of Chemistry, Biochemistry and Pharmaceutical Sciences

**Lipid-based drug delivery systems for inflammation and fibrosis  
therapies**

Inaugural dissertation  
of the Faculty of Science,  
University of Bern

presented by

Marianna Carone

from Italy

Supervisor of the doctoral thesis:

Prof. Dr. Paola Luciani

Department of Chemistry, Biochemistry and Pharmaceutical Sciences

Accepted by the Faculty of Science.

Bern, 27.04.2023

The Dean  
Prof. Dr. Marco Herwegh



## Table of Contents

<b>Chapter 1: Background and purpose</b> .....	4
1. Introduction to inflammation and fibrosis .....	5
2. Mucosal drug delivery .....	5
3. Mucus as critical barrier to drug delivery .....	6
4. Considerations for developing mucosal drug delivery .....	7
5. Materials for mucosal drug delivery .....	9
5.1 Hydrogels .....	10
5.2 Liposomes .....	12
5.3 Liquid crystals .....	15
6. Aim of the thesis .....	17
7. References .....	20
<b>Chapter 2: Temperature-triggered in situ forming lipid mesophase gel for local treatment of ulcerative colitis</b> .....	23
1. Introduction .....	24
2. Materials and methods .....	26
3. Results and discussion.....	30
4. Conclusions .....	42
5. References .....	43
<b>Chapter 3: Composite layer-by-layer liposomal gel for mucosal delivery of pirfenidone</b> ....	46
1. Introduction .....	47
2. Materials and methods .....	48
3. Results and discussion.....	53
4. Conclusions .....	59
5. References .....	61
<b>Chapter 4: Design and use of lipid mesophase to formulate 3D-printed oral dosage form</b> ..	63
1. Introduction .....	64
2. Materials and methods .....	66
3. Results and discussion.....	70
4. Conclusions .....	82
5. References .....	84
<b>Chapter 5: Conclusions and Outlook</b> .....	87
Appendix.....	91

A1. Temperature-triggered in situ forming lipid mesophase gel for local treatment of ulcerative colitis .....	92
A2. Composite layer-by-layer liposomal gel for mucosal delivery of pirfenidone .....	101
A3. Design and use of lipid mesophase to formulate 3D-printed oral dosage form .....	106
References .....	110
Abbreviations .....	111
Acknowledgments.....	113
Declaration of consent .....	114
<b>Curriculum vitae</b> .....	115

# **Chapter 1**

## **Background and purpose**

## 1. Introduction to inflammation and fibrosis

Inflammation is the body's initial response to invading pathogens or endogenous signals such as damaged cells, involving the activation of the immune system to clear the damaged tissue and prevent the spread of infection<sup>1</sup>. Prolonged or chronic inflammation in the affected organ can lead to fibrosis, a progressive condition characterized by the deposition of extracellular matrix. Fibroblasts and other mesenchymal cell types across the body, including hepatic stellate cells, undergo activation and differentiation in response to chronic inflammation, laying down scar tissue<sup>2</sup>. While scar tissue can help support damaged tissue, it can also impede organ function and ultimately lead to organ failure.

Inflammation is recognized as a major cause of disease, with chronic infection and inflammation contributing to about 15% of human cancers<sup>3</sup>. Organ fibrosis is responsible for around 45% of deaths in industrialized countries<sup>4</sup>, with about 800,000 deaths per year, and this number is expected to increase with the rise in life expectancy<sup>5</sup>. There is a significant clinical need for new treatments without severe systemic side effects, as only two drugs have been approved as antifibrotics in Europe and the US, both for the management of idiopathic pulmonary fibrosis<sup>6</sup>.

The targeting of inflammation and fibrosis at the site of tissue damage through drug delivery systems holds significant promise for the development of effective treatments for chronic inflammatory diseases. This thesis focuses on developing drug delivery systems that can effectively target inflammatory and fibrotic diseases by exploiting the mucosal surfaces. Mucosal surfaces are protective barriers that prevent the entry of harmful pathogens and toxins into the body, while also playing a critical role for maintaining immune homeostasis. When chronic inflammation occurs in these surfaces, it can cause significant tissue damage and contribute to the development of chronic diseases, such as inflammatory bowel disease (IBD) and intestinal fibrosis.

## 2. Mucosal drug delivery

Mucosal drug delivery refers to the delivery of drugs through mucosal surfaces, which are highly specialized tissues that line various body cavities, including the mouth, lung,



gastrointestinal tract, and reproductive organs. These surfaces are characterized by a rich supply of blood vessels, lymphatic vessels, and easy access, making them attractive targets for drug delivery<sup>7</sup>. Despite these advantages, one of the major challenges to mucosal delivery is the presence of a mucus layer lining the mucosal epithelium. Mucus is a viscous hydrogel secreted by the intraepithelial cells that lines on the surface of mucosal tissues<sup>8</sup>. Due to its steric barrier and adhesion properties, mucus acts as a dynamic semipermeable barrier and its main functions include lubrication and hydration of the epithelia, exchange of nutrients, water, gases, and hormones while preventing pathogen and foreign particulate entry<sup>9</sup>. A functioning mucus barrier is essential for health, protecting the body's surface from pathogens, irritants, and drying out. Dysregulation of mucus production or composition can impair its barrier function and increase the risk of infection and disease. Examples of diseases related to mucus dysregulation include cystic fibrosis<sup>10,11</sup>, IBD<sup>12,13</sup> and colorectal cancer<sup>14</sup>. Therefore, while it is essential in protecting the underlying epithelium, it may represent a barrier to drug delivery. Indeed, the drug carriers must overcome environmental cues such as ionic strength, mucus mesh, pH, and mucus clearance, and reach the underlying cell layers of the mucosal tissue<sup>15</sup>. Understanding the mechanisms by which mucus acts as a selective barrier as well as the mechanisms of mucoadhesion is of great value in the design of effective systems for mucosal drug delivery.

### 3. Mucus as critical barrier to drug delivery

While exerting protective functions, mucus acts as a barrier, reducing the permeation of drugs and potentially affecting their efficacy. Indeed, the bioactive molecules must overcome multiple barriers that can be classified as steric, dynamic, and interactive<sup>16</sup> (**Figure 1**). Mucus is composed primarily of water (95%), glycoproteins (2-5%), and a small amount of lipids, electrolytes, cell components, and immune factors (1-5%)<sup>17-20</sup>. The network generated by the mucins, the major functional components of the extracellular mucus, forms a size exclusion filter which regulates the diffusion of molecules; especially, it has been shown that small molecules are capable of freely diffusing the mucus layer, while larger compounds - like proteins - did not penetrate the network<sup>22</sup>. Furthermore, the intrinsic viscosity and the unstirred water layer may contribute to the generation of a steric barrier as well. Mucus acts as physicochemical interactive barrier, whereby multiple low-affinity interactions are formed between mucus and bioactive molecules. For example, hydrophobic interactions may occur

between the protein of mucin or the lipidic components of the mucus and bioactive molecules, thus limiting their diffusion especially for hydrophobic compounds<sup>23</sup>. Additionally, mucus acts as a dynamic barrier as it is constantly cleared and renewed. This turnover time sets a limit to the diffusion of molecules through the barrier, thus restricting their mucosal absorption.

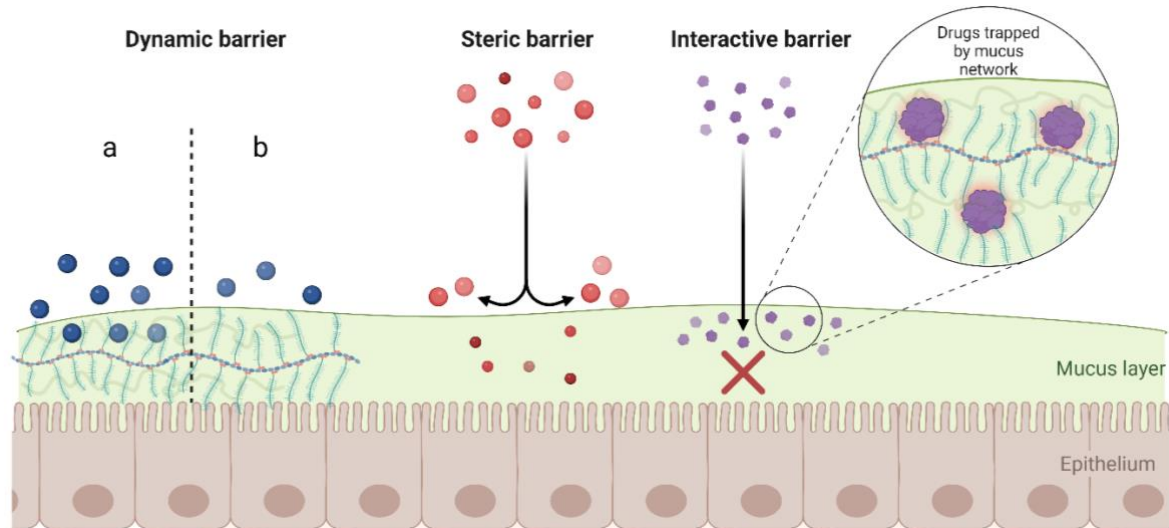


**Figure 1:** Representation of the dynamic, steric and interactive barrier of mucus. Drug particles (blue) interact with the outermost layer of mucus (a), drug particles being cleared due to the mucus turnover (b). Steric barrier: small particles can freely diffuse through the mucus network while blocking the entry of larger drug particles. Interactive barrier: drug particles interact with mucus components.

#### 4. Considerations for developing mucosal drug delivery

The development of mucosal drug delivery requires the considerations of several key factors. One crucial factor is the compatibility of the delivery system with the specific mucosal environment to ensure effective and safe delivery. For example, pH and viscosity of the mucus can impact the adhesion and stability of the delivery system. Additionally, the drug delivery system must adhere for an adequate period of time to guarantee efficient delivery. The release profile of the drug must be carefully controlled to minimise toxicity, and the drug carrier must be biocompatible and well-tolerated by the patient. Moreover, the approval process for mucosal drug delivery involves demonstrating that the system meets relevant regulatory requirements and guidelines, including safety, efficacy and quality control. Overall, the design and development of drug delivery systems require a multi-disciplinary approach, involving expertise in drug delivery, materials science, pharmacology, and regulatory affairs.

Mucoadhesive polymers, surface modification of nanoparticles, manipulation of zeta potential and self-nanoemulsifying drug delivery systems are some of the strategies used to enhance

drug permeation across mucus<sup>15</sup>. In the upcoming section, I will share the guiding principles I followed for materials selection during my doctoral studies and examine the interaction between polymer and mucus.

### *Mucoadhesive polymers*

A mucoadhesive polymer is a type of polymer that has the ability to adhere to mucosal surfaces, such as the digestive or reproductive tract. The specific mechanism of adhesion depends on several factors, including the chemical composition of the polymer, the viscoelastic properties of mucus, and the surface properties of the polymer. Some of the common mechanisms of adhesion are listed below:

1. Hydrogen bonding: the polymer contains functional groups that can form hydrogen bonds with mucus components. This mechanism is common in polysaccharides such as polyacrylic acid<sup>24</sup>.
2. Electrostatic interaction: the polymer and mucus have opposite charges. This mechanism is common in polymers such as the positively charged polyelectrolyte chitosan<sup>25</sup>(*vide infra*, **Figure 3**).
3. Van der Waals forces: this involves weak non-covalent interactions between the polymer and mucus molecules. This mechanism is common in hydrogels<sup>26</sup>.

The mechanism of adhesion of mucoadhesive polymers is complex and depends on several factors, but the goal is to achieve strong and long-lasting adhesion to the mucosal surface.

### *Surface modification of nanoparticles*

Among the various strategies of surface modification, nanoparticles as drug carriers can be functionalised with mucoadhesive polymers. These nanoparticles are designed to improve the bioavailability and therapeutic efficacy of drugs, by increasing the residence time and reducing systemic exposure of the drug. Some examples of mucoadhesive polymer-coated nanoparticles include (1) chitosan-coated nanoparticles for ocular delivery<sup>27-30</sup>, used to deliver drugs such as anti-inflammatory agents and antibiotics for the treatment of eye diseases (2) polyethylene glycol (PEG)-coated nanoparticles, which are used for vaginal delivery<sup>31</sup> (3) alginate-coated nanoparticles, used for oral delivery<sup>32</sup> and are effective in treating digestive tract disease such as IBD<sup>33</sup>, and (5) polyvinyl acetate (PVA)-coated nanoparticles which are strongly immobilized in human cervicovaginal mucus<sup>34</sup>, thus increasing the retention time.

### *Altering zeta potential*

Dispersion of particles in a liquid medium leads to the functional groups on their surface interacting with the surrounding medium, resulting in the development of a surface charge. This surface charge attracts oppositely charged ions, resulting in the formation of two layers of ions on the particle's surface in a colloidal system: the stern layer, consisting of ions tightly bound to the surface, and the diffuse layer, consisting of ions loosely bound to the surface. The Zeta potential refers to the electrical potential at the slipping plane where the diffuse layer meets the surrounding liquid. In the context of mucosal delivery, altering the zeta potential of drug carriers can influence their ability to penetrate the mucus barrier. For example, positively charged particles can interact with the negatively charges mucus – due to sialic acid and sulfonic acid- which can result in immobilization of particles in the mucus due to ionic interactions<sup>35</sup>. Conversely, negatively charged nanoparticles may diffuse more freely in mucus compared to positively charged nanoparticles due to repulsive interaction<sup>36</sup>. However, the diffusion of particles through the mucus can depend on a number of other factors and may not always be a guarantee of improved mucus penetration.

#### *Self-nanoemulsifying drug delivery systems*

The term ‘self-emulsifying’ refers to the ability of systems to spontaneously form a stable nano emulsion upon dilution in an aqueous environment, such as the gastrointestinal tract<sup>37</sup>. In mucosal delivery, these systems can disrupt the structure of mucus, reducing its viscosity and improving the permeation of drugs. It has been hypothesized that the core mechanism relies on the reduced interactions between the hydrophobic surface of the emulsion and the hydrophilic regions of mucin fibers<sup>38</sup>. Furthermore, the emulsion can also increase the solubility and stability of the drug, enhancing its bioavailability as well<sup>39</sup>. Overall, self-nanoemulsifying systems offer a promising solution for improving the delivery and efficacy of drugs, especially for those with low solubility and permeability through the mucosal surfaces.

## 5. Materials for mucosal drug delivery

My doctoral studies involved an extensive exploration of three types of materials for their potential as mucosal drug delivery systems: hydrogels, liposomes, and liquid crystals. The primary objective of this research was to enhance the bioavailability of drugs both locally (as discussed in Chapters 2 and 3) and systemically (as discussed in Chapter 4).

The mucoadhesive properties of hydrogels are attributed to the combination of surface and diffusional phenomena that contribute to the formation of interchain bridges between the polymer and the biological medium, resulting in strong adhesion to mucosal surfaces<sup>40</sup>. This technology has undergone significant evolution, leading to the development of numerous multifunctional hydrogels, including nanocomposites. Specifically, Chapter 3 of this dissertation details the development of a hybrid liposome-hydrogel nanocomposite. In contrast, lipid lyotropic liquid crystals rely on mucus dehydration for mucoadhesion, and the strength of the mucoadhesive joint is dependent on the material's ability to absorb water from the mucosa<sup>41</sup>. In the following paragraphs, I introduce each material used in my research and contextualize their utility as drug delivery systems.

## 5.1 Hydrogels

Hydrogel is a hydrophilic three-dimensional polymer network that has the ability to absorb and retain large amounts of water or biological fluids, making it swell and form a gel-like materials<sup>42</sup>. The high-water content (ranging from 70-99%) provides excellent biocompatibility while the presence of a polymer network gives mechanical properties. The stiffness can be tuneable, matching the desired consistency of the material. Similarly, the crosslinked network protects the encapsulated material from the penetration of various proteins<sup>43</sup>, and it is thus believed to protect molecules from degradation by diffusing enzymes. This characteristic is particularly appealing for macromolecules – proteins or antibodies – which represent an increasing percentage of new drugs approved<sup>44</sup>.

Depending on their ionic charge (neutral, anionic, cationic or ampholytic), their method of preparation (e.g., homo- or multi-polymers) or their source, hydrogels may be classified in different categories. For example, based on their source, they are classified into two broad categories: natural and synthetic. Natural hydrogels are made from naturally occurring polymers, such as chitosan or alginate. Synthetic hydrogels are made from synthetic polymers, such as PVA, polyethylene glycol (PEG), or polyacrylamide. These hydrogels have well-defined mechanical properties and can be designed to meet specific requirements, as degradation rate or on demand release profile. Each type of hydrogel has its own unique advantages and limitations, and the choice of hydrogel type depends on the specific application and requirements.

*Natural hydrogels* Alginate is an anionic polymer generally extracted from brown algae (*Phaeophyceae*). It is a linear polysaccharide comprising of  $\beta$ -D-mannuronate (M) and its C5-epimer  $\alpha$ -L-glucuronate (G) residues (**Figure 2**). The G residues contribute to intermolecular cross-linking in presence of divalent cations (e.g.,  $Zn^{2+}$ ) to form an egg-box structure, responsible for the formation of the alginate hydrogel. The distribution of these two residues within the alginate chain play a key role in determining the properties of alginate hydrogels, such as elasticity, stiffness, and degradation rate<sup>45,46</sup>. Generally, the mechanical properties are improved as the G-block length and molecular weight increase<sup>46</sup>.

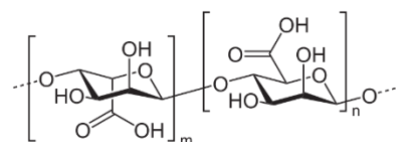


**Figure 2:** Structure of alginate.

Chitosan is a cationic polymer obtained by partial deacetylation (about 50%) of chitin in alkaline conditions<sup>47</sup>. It is a linear polysaccharide composed of randomly distributed  $\beta$ -(1-4)-linked D-glucosamine and N-acetyl-D-glucosamine units<sup>48</sup>(**Figure 3**). Chitosan can be crosslinked both covalently and ionically when in contact with specific polyanions<sup>49</sup>. The advantage of using chitosan is not only restricted to the intrinsic biodegradability, but also to the antibacterial properties and presence of the polar groups able to form H bonding with other compounds.

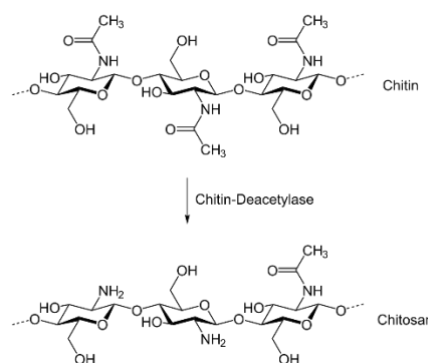


**Figure 3:** Structure of chitosan.

*Synthetic hydrogels* PVA is a biocompatible polymer made from the hydrolysis of polyvinyl acetate. It is extensively used in biomedical applications including the production of contact lenses or artificial joints. Furthermore, modifying the surface of drug carriers with PVA can provide particles with the ability to penetrate through mucus<sup>15</sup>. However, PVA has restricted application in drug delivery as it lacks the ability to efficiently load drugs and control their release in a controlled manner<sup>50</sup>. PEG is another synthetic polymer extensively used in the biomedical field for its hydrophilicity and relative inertness<sup>51</sup>, particularly used as a 3D scaffold for tissue engineering.

### *Applications of hydrogels*

Hydrogels have demonstrated great utility across many branches of biomedical applications, especially in the areas of drug delivery, *in vitro* cell culture and regenerative medicine - where their excellent biocompatibility and biodegradability play a major role. Hydrogels can be

designed to evoke both systemic and local drug delivery of various therapeutic agents, including small molecules, biomolecules, and cells. Indeed, they can serve as drug delivery platform able to respond to the microenvironments via *in situ* assembly, controllable degradation<sup>52</sup>, and on demand drug release from encapsulated nanocarriers<sup>53</sup>. However, a continuing challenge is represented by the fast and uncontrolled release of drugs from the 3D network, which may lead to undesired side effects and toxicity. Different approaches are used to minimise this effect, for example the use of liposome hydrogel systems<sup>54,55</sup>. In this approach, liposomes encapsulate the bioactive agent, and the drug-liposome system is further integrated within the hydrogel matrix, which provides a physical barrier that facilitates both the protection of liposomes from degradation and increases their stability. The combination of these two components, liposome hydrogel systems offer a way to achieve both targeted drug delivery and controlled release. In conclusion, these features make hydrogels a versatile material for the development of drug delivery systems for a variety of therapeutic applications.

## 5.2 Liposomes

Amphiphilic lipids can spontaneously self-assemble into a wide range of structures, including for example liposomes and micelles. This self-assembly is driven by the hydrophobic effect, which originates from the tendency of the hydrophobic tails to avoid water by clustering together, thus minimizing their exposure to the aqueous environment<sup>56</sup>. In the case of liposomes, the hydrophobic tails of the phospholipids associate together to form the inner core of the bilayer, while the hydrophilic heads remain in contact with the aqueous environment. The type of self-assembled structure formed depends primarily on the structure of the amphiphiles. For monopolar, amphiphilic molecules such as phospholipids, it is possible to estimate the expected type of structure via the packing parameter (CPP). CPP can be calculated from the area of the headgroup, the length of the alkyl chain and its volume<sup>57</sup>. The structures formed range from spherical or ellipsoidal ( $CPP \leq 1/3$ ), cylindrical simple ( $CPP \leq 1/2$ ), or lamellar ( $CPP = 1$ ). Liposomes are formed when the packing parameter is between 0.5 and 1. The concentration of the amphiphile (critical aggregating concentration), the temperature of the dispersion, the ionic strength and pH of the solution also play a major role.

The main steps involved in the preparation of liposomes, according to the classical dry lipid film method, are the dissolution of phospholipids in organic solvents and the further hydration. After the evaporation of the organic solvent, the phospholipids molecules rearrange into bilayers that separate very slowly upon hydration. During the hydration step, it is possible to

obtain liposomes of different shapes and size. Depending on how fast the bilayers separate, it is possible to differentiate slow bilayer separation and fast bilayer separation leading to multilamellar and unilamellar vesicles, respectively (**Figure 4**)<sup>58-60</sup>. The liposomes' size is mainly determined by the kinetics of membrane size growth; however, there is a minimum membrane size for each phospholipid below which liposome formation is energetically unfavourable<sup>61</sup>.

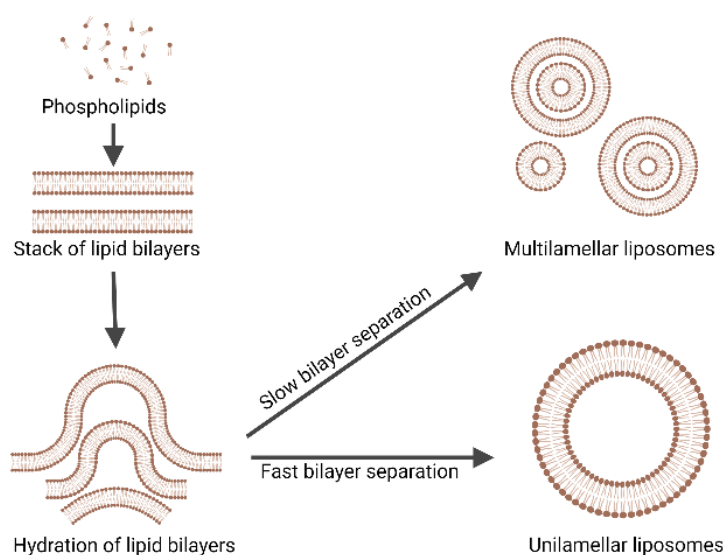


**Figure 4:** Formation of multilamellar and unilamellar liposome.

Liposomes can be classified based on their size and number of lamellae in small unilamellar vesicles (SUV) when the vesicles are unilamellar with a size is less than 100 nm, whereas they are defined large unilamellar vesicles (LUV) when liposomes are larger than 100 nm. Lastly, giant unilamellar vesicles are known as GUV with a size range greater than 1000 nm. Vesicles with an onion-like structure are referred to as oligolamellar when the number of lamellae is between 2-5, while those with more than 5 layers are called multilamellar vesicles (MLV). Vesicles consisting of multiple non-concentric bilayers are known as multivesicular vesicles (MVV)<sup>62</sup>. The liposomal classification is schematically represented in **Figure 5**. Vesicle size and lamellarity affect the pharmacokinetic profile, stability, and bioavailability of liposomes. Therefore, the amount of drug encapsulated is determined by both size and number of lamellae.



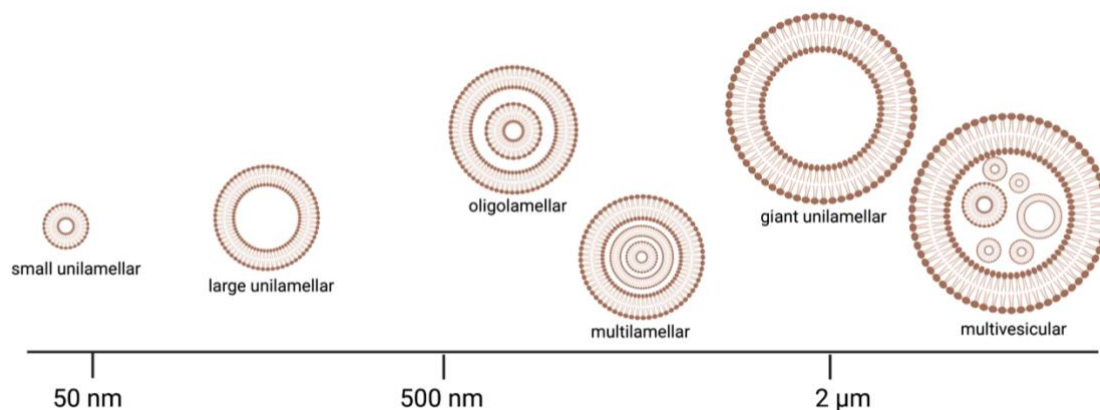


**Figure 5:** Schematic overview of liposomes' classification.

### *Applications of liposomes*

Amphiphilic molecules' ability to self-organise can offer advantages such as increased solubilisation, sustained release, and protection against enzymatic degradation and hydrolysis of the drug. Liposomes, with their biocompatibility and biodegradability, were the first drug delivery system approved for clinical use<sup>63</sup>. They are well-investigated nanocarriers for targeted drug delivery with the potential to improve drug stability and solubilization and to increase the drug's half-life along with overcoming resistance against chemotherapeutics<sup>64</sup>. As a drug delivery system, liposomes can encapsulate both lipophilic and hydrophilic drugs. Lipophilic drugs are entrapped in the lipid bilayer while the hydrophilic and water-soluble molecules can be incorporated into the aqueous core. Additionally, a variety of macromolecules such as DNA and proteins can also be incorporated into the inner core<sup>65,66</sup>. Once injected in the bloodstream, conventional liposomes are subjected to opsonization with serum components and uptake by the mononuclear phagocyte system resulting in rapid clearance<sup>67</sup>. To improve the therapeutic efficacy, liposomes were first modified with a hydrophilic polymer, PEG. While the steric stabilization strongly resulted in prolonged circulation times, PEGylated liposomes lack specificity. To increase their selectivity, the liposomal surface can be modified with specific ligands, such as antibodies, receptors, or cell adhesion molecules<sup>68</sup>. In conclusion, liposomal drug delivery systems represent a versatile and dynamic technology with the potential of improving therapeutic treatments for various diseases.

### 5.3 Liquid crystals

To minimize water-oil interactions, lipids spontaneously self-assemble into a wide range of structures, as described above. The ensuing architectures can be as simple as for the spherical liposomes, but they can result also in more complex liquid crystalline phases with different geometries. The specificity of each structure is directly dependent on external perturbation, such as changes in temperature or pH<sup>69</sup>.

In this paragraph, we focus on lipidic lyotropic liquid crystals. These systems are constituted by molecules derived from fatty acids, which are amphiphilic in nature and capable of self-assembly in the presence of solvents. The lipid molecules in these systems are dynamic and behave like a viscous liquid, yet they nonetheless maintain a level of overall order like that of a crystalline solid.

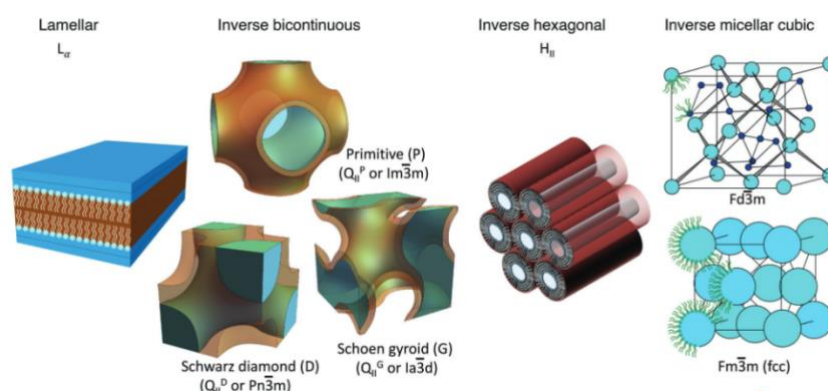


**Figure 6:** Examples of lipid mesophases structures. Figure is adapted from Adv Mater 31, 1–19 (2019) with permission.

Upon the addition of water, phospholipids, monoglycerides and galactolipids form lyotropic liquid crystals<sup>69</sup>. As shown in **Figure 6**, typical lipid liquid crystalline phases are lamellar ( $L_\alpha$ ), inverse micellar cubic, inverse hexagonal (H) and inverse bicontinuous (Q). At the left of the diagram is the lamellar phase, consisting of a two-dimensional stack of amphiphilic bilayers separated by water. In the hexagonal phase, the lipids form cylindrical inverse micelles packed in a hexagonal lattice. Three types of bicontinuous cubic phases are Schoen gyroid (Ia3d) with threefold connectivity of aqueous channels, the Schwarz double diamond (Pn3m) with fourfold connectivity and the double primitive (Im3m) with sixfold connectivity. Typically, as the water content increases, the sequence of bicontinuous cubic phases go in the order Ia3d-Pn3m-Im3m<sup>70</sup>. This pattern is generally observed, although it is rare for all three cubic phases to be present in a single pure lipid-water system<sup>71</sup>. Lastly, the inverse micellar phase consists of spheroidal

micelles arranged in Fd3m or Fm3m symmetry. Typically, majority of the lipids exhibit these phases only in presence of oil-based components, such as tocopherol or limonene<sup>72</sup>.

Scientists have generated a variety of phase diagrams for a specific lipid or a mixture of lipids, which describe the presence of various phases in relation to parameters such as the content of solvents, temperature, and pressure<sup>69</sup>. For example, within the monoacylglycerol family, monolinolein (MLO) is one of the most well-known. MLO is formed by a single linoleoyl chain linked to a glycerol head group by an ester bond (**Figure 7a**). Commercially available, MLO may be obtained in two forms, as mixed glyceride or as distilled lipid; the latter is preferred for pharmaceutical applications owing to the high purity<sup>73</sup>.

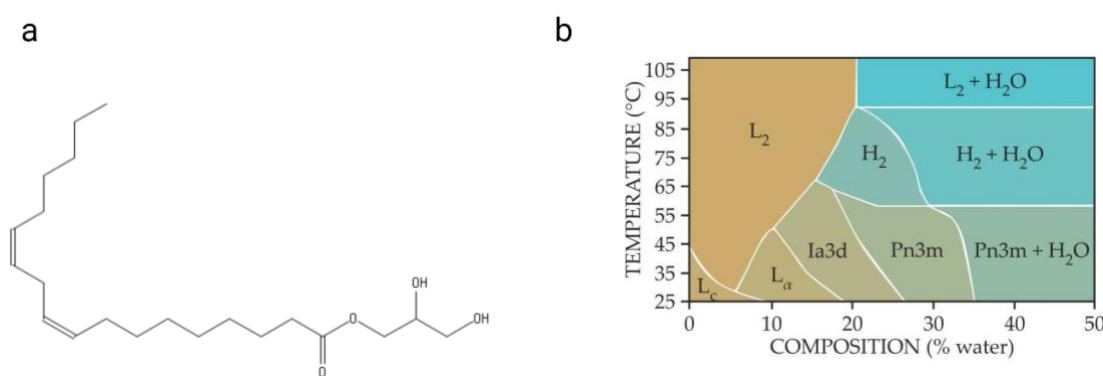


**Figure 7:** (a) Chemical structure of monolinolein; (b) the phase diagram of MLO for different water content or temperature values. Panel b is reproduced from Simone Aleandri, Raffaele Mezzenga; The physics of lipidic mesophase delivery systems, *Physics Today* 2020; 73 (7): 38–44. <https://doi.org/10.1063/PT.3.4522>, with the permission of the American Institute of Physics.

**Figure 7b** shows the phase diagram of MLO as an example of a monoglyceride-water mixture. At room temperature and upon addition of water, the lamellar crystalline phase of MLO shows first a transition to an  $Ia3d$  and later to a  $Pn3m$  phase. Indeed, the addition of water is responsible for a reorganization of the geometry which starts from lamellar to a 3D bicontinuous cubic phase following the order  $Ia3d$  -  $Pn3m$  phase, the latter stable also in excess of water. On the other hand, starting from a water content of 19% and increasing the temperature, the system undergoes a transition from  $Ia3d$  to hexagonal phase (H). As for the  $pn3m$  phase, the excess of water remains confined outside the H structure and the resulting phase is in a thermodynamic equilibrium with the bulk water<sup>74</sup>. The ability to change phase - while remaining thermodynamically stable - makes these systems particularly suitable for several applications such as drug delivery<sup>72</sup>.

### *Applications of liquid crystals*

Liquid crystals, particularly lipidic lyotropic liquid crystals, have generated considerable interest in drug delivery, as biocompatible and thermodynamically stable material with outstanding controlled release properties of certain phases<sup>75</sup>. Crucial to the benefits of mesophases is that many of the lipids are nontoxic and classified as GRAS (generally recognized as safe) compounds. Due to the amphiphilic nature, they represent a versatile material able to incorporate bioactive molecules with different size and polarity including biologicals and nucleic acids while protecting them from hydrolysis or oxidation<sup>76-78</sup>. The release of such bioactive molecules is diffusion-based therefore strictly dependent on the structure of the specific phase, and on the size and lipophilicity of the drug. Hydrophilic compounds and small water-soluble proteins are located in the aqueous channels, consequently their mobility is related to the dimensionality of the lipidic mesophase<sup>79</sup>. On the other hand, the hydrophobic encapsulants must partition out of the bilayer into the aqueous compartment and travel via the channels in order to be released from the structure<sup>72,80</sup>. It is therefore important to understand the self-assembled structures to relate them to the diffusion of the encapsulated drugs. At present, Camurus, a Swedish pharmaceutical company, is working on several technologies that utilize a lipidic precursor capable of transforming into lipidic mesophase when it comes in contact with water. Moreover, lipidic lyotropic liquid crystals are being investigated for intravenous<sup>81,82</sup> and topical<sup>83,84</sup> application. They are bioadhesive materials able to adhere to the wet mucosa thanks to a mucus dehydration-based mechanism<sup>85</sup>, thus they are used for mucosal<sup>86 83,84</sup> applications, too<sup>86</sup>. Furthermore, they can be formulated as long-lasting injectable depots for example subcutaneously<sup>87,88</sup> or spray-dried to produce solid oral dosage forms<sup>89</sup>.

## 6. Aim of the thesis

The aim of this thesis was to identify lipid-based drug delivery systems for the treatment of inflammatory and fibrosis diseases. The thesis can be divided into three main parts.

Ulcerative colitis is a chronic inflammatory bowel disease, and it strongly affects patients' quality of life. The harsh side effects of the current therapies call for new treatment strategies that could maximize the drug concentration at the site of inflammation with minimal systemic exposure. Capitalizing on the biocompatible and biodegradable structure of lipid mesophases, in **Chapter 2**, we developed a temperature-triggered *in situ* forming lipid gel specifically for

topical treatment of ulcerative colitis. The lipid mesophase can host and release drugs of different polarity, tofacitinib or tacrolimus, in a sustained manner and adheres to the mucosal colon wall for more than 6 h, an ideal time to avoid leakage and to improve bioavailability. The developed formulation can be self-administered and overall can improve patient compliance, ameliorating colitis and minimizing adverse effects associated with a systemic therapy.

Inflammatory bowel disease is the main cause of intestinal fibrosis and strictures, major contributors to morbidity and healthcare cost. Therefore, a pharmacological treatment to prevent fibrosis and strictures in the gastrointestinal tract would be transformational for patient care. Local fibrotic diseases, such as intestinal fibrosis and endometriosis, have few effective therapeutic options available. While there has been some progress in developing pharmacological treatments for fibrosis, only two drugs, pirfenidone, and nintedanib, have been approved, both for the treatment of idiopathic pulmonary fibrosis (IPF). Except for IPF, there are no antifibrotic drugs for any other indication. However, exploratory studies have shown that pirfenidone has the potential to be repurposed for other fibrotic pathologies in multiple organs. To this aim, in **Chapter 3**, our research focuses on developing a liposome-based system to deliver pirfenidone, specifically for the treatment of intestinal fibrosis and endometriosis. By surface capping liposomes with commercially available biopolymers, we obtained ultrahigh drug loading and tunable release profiles over a time range compatible with intestinal and vaginal delivery. Furthermore, to improve the topical applicability of such system and the long-term physical stability, the liposome-based system was homogeneously incorporated into a zinc alginate hydrogel.

Lipid-based formulations offer an attractive approach for enhancing the oral bioavailability of lipophilic and water insoluble drugs. However, their use in solid oral tablet form has proven challenging due to the lack of flexibility of lipids required to produce stable and uniform tablets. Our focus in **Chapter 4** was on developing a 3D printable lipid mesophase that enables the production of oral dosage forms with high lipid content for the effective delivery of water-insoluble drugs through self-emulsification. Our approach involved selecting a lipid mixture called S80, which is rich in polyenylphosphatidylcholines (>75%) and has demonstrated ability to deactivate profibrogenic hepatic stellate cells, the primary collagen-producing cells in hepatic fibrogenesis. We developed lipid matrices with specific material and self-emulsification properties by exploring the relationship between nanostructure and mechanical

properties. Further, we evaluated the ability of these matrices to enhance the solubility of obeticholic acid, a semi-synthetic analogue of bile acid known for its poor water solubility.

## 7. References

1. A current view on inflammation. *Nat Immunol* **18**(8), 825 (2017).
2. Zhao, X., Kwan, J. Y. Y., Yip, K., Liu, P. P. & Liu, F. F. Targeting metabolic dysregulation for fibrosis therapy. *Nat Rev Drug Discov* **19**, 57–75 (2020).
3. Greten, F. R., Grivennikov, S. I. Inflammation and Cancer: Triggers, Mechanisms, and Consequences. *Immunity* **51**, 27–41 (2019).
4. Henderson, N. C., Rieder, F., Wynn, T. A. Fibrosis: from mechanisms to medicines. *Nature* **587**, 555–566 (2020).
5. Oakley, F., Gee, L. M., Sheerin, N. S., Borthwick, L. A. Implementation of pre-clinical methodologies to study fibrosis and test anti-fibrotic therapy. *Curr Opin Pharmacol* **49**, 95–101 (2019).
6. Lamb, Y. N. Nintedanib: A Review in Fibrotic Interstitial Lung Diseases. *Drugs* **81**, 575–586 (2021).
7. Watchorn, J., Clasky, A. J., Prakash, G., Johnston, I. A. E., Chen, P. Z., Gu, F. X. Untangling Mucosal Drug Delivery: Engineering, Designing, and Testing Nanoparticles to Overcome the Mucus Barrier. *ACS Biomater Sci Eng* **8**, 1396–1426 (2022).
8. Werlang, C., Cárcarmo-Oyarce, G., Ribbeck, K. Engineering mucus to study and influence the microbiome. *Nat Rev Mater* **4**, 134–145 (2019).
9. Cone, R. A. Barrier properties of mucus. *Adv Drug Deliv Rev* **61**, 75–85 (2009).
10. Finkbeiner, W. E., Zlock, L. T., Morikawa, M., Lao, A. Y., Dasari, V., Widdicombe, J. H. Cystic fibrosis and the relationship between mucin and chloride secretion by cultures of human airway gland mucous cells. *Am J Physiol Lung Cell Mol Physiol* **301**, 402–414 (2011).
11. Henke, M. O., John, G., Germann, M., Lindemann, H., Rubin, B. K. MUC5AC and MUC5B Mucins Increase in Cystic Fibrosis Airway Secretions during Pulmonary Exacerbation. *Am J Respir Crit Care Med* **175**, 816–821 (2012).
12. Heazlewood, C. K., Cook, M. C., Eri, R., Price, G. R., Tauro, S. B., Taupin, D., Thornton, D. J., Png, C. W., Crockford, T. L., Cornall, R. J., Adams, R., Kato, M., Nelms, K. A., Hong, N. A., Florin, T. H., Goodnow, C. C., McGuckin, M. A. Aberrant Mucin Assembly in Mice Causes Endoplasmic Reticulum Stress and Spontaneous Inflammation Resembling Ulcerative Colitis. *PLoS Med* **5**, 0440–0460 (2008).
13. Buisine, M. P., Desreumaux, P., Leteurtre, E., Copin, M. C., Colombel, J. F., Porchet, N., Aubert, J. P. Mucin gene expression in intestinal epithelial cells in Crohn's disease. *Gut* **49**(4), 544–51 (2001).
14. Betge, J., Schneider, N. I., Harbaum, L., Pollheimer, M. J., Lindtner, R. A., Kornprat, P., Ebert, M. P., Langner, C. MUC1, MUC2, MUC5AC, and MUC6 in colorectal cancer: expression profiles and clinical significance. *Virchows Arch.* **469**(3), 255–65. (2016).
15. Bandi, S. P., Bhatnagar, S., Venuganti, V. V. K. Advanced materials for drug delivery across mucosal barriers. *Acta Biomater* **119**, 13–29 (2021).
16. Boegh, M., Nielsen, H. M. Mucus as a barrier to drug delivery - Understanding and mimicking the barrier properties. *Basic Clin Pharmacol Toxicol* **116**, 179–186 (2015).
17. Gipson, I. K. Mucins of the human endocervix. *Front Biosci* **6**, 1245 (2001).
18. Samet', J. M., Cheng, P.-W. The Role of Airway Mucus in Pulmonary Toxicology. *Environ Health Perspect* **2**, 89–103 (1994).
19. Quraishi, M. S., Jones, N. S., Mason, J. The rheology of nasal mucus: a review. *Clin Otolaryngol Allied Sci* **23**, 403–413 (1998).
20. Chao, C. C. W., Vergnes, J. P., Brown, S. I. Fractionation and partial characterization of macromolecular components from human ocular mucus. *Exp Eye Res* **36**, 139–150 (1983).
21. Soybel, D. I. Anatomy and physiology of the stomach. *Surg Clin North Am* **85**(5), 875–94 (2005).
22. Yildiz, H. M., McKelvey, C. A., Marsac, P. J., Carrier, R. L. Size selectivity of intestinal mucus to diffusing particulates is dependent on surface chemistry and exposure to lipids. *J Drug Target* **23**, 768–774 (2015).
23. Sigurdsson, H. H., Kirch, J., Lehr, C. M. Mucus as a barrier to lipophilic drugs. *Int J Pharm* **453**, 56–64 (2013).
24. Bioscience, M., Goycoolea, F. M., Menchicchi, B., Caramella, C. M., Saporito, F., Lee, S., Stephansen, K., Chronakis, I. S., Hirth, M., Adamczak, M., Waldner, M., Nielsen, H. M., Marcelloni, L. Innovative Methods and Applications in Mucoadhesion Research Macromolecular Bioscience. *Macromol. Biosci* **17**(8) (2017).
25. Cazorla-Luna, R., Martín-Illana, A., Notario-Pérez, F., Ruiz-Caro, R., Veiga, M. D. Naturally Occurring Polyelectrolytes and Their Use for the Development of Complex-Based Mucoadhesive Drug Delivery Systems: An Overview. *Polymers* **13**, 2241 (2021).
26. Hanafy, N. A. N., Leporatti, S., El-Kemary, M. A. Mucoadhesive Hydrogel Nanoparticles as Smart *Biomedical Drug Delivery System* **9**(5), 825 (2019).
27. Shi, S., Zhang, Z., Luo, Z., Yu, J., Liang, R., Li, X., Chen, H. Chitosan grafted methoxy poly(ethylene glycol)-poly( $\epsilon$ -caprolactone) nanosuspension for ocular delivery of hydrophobic diclofenac. *Sci Rep* **12**(5), 11337 (2015).
28. Akhter, S., Anwar, M., Siddiqui, M. A., Ahmad, I., Ahmad, J., Ahmad, M. Z., Bhatnagar, A., Ahmad, F. J. Improving the topical ocular pharmacokinetics of an immunosuppressant agent with mucoadhesive nanoemulsions: Formulation development, in-vitro and in-vivo studies. *Colloids Surf B Biointerfaces* **148**, 19–29 (2016).
29. Onugwu, A. L., Attama, A. A., Petra, O. N., Nnamani, Onugwu, S. O., Onuigbo, S. O., Khutoryanskiy, V. V. Development and optimization of solid lipid nanoparticles coated with chitosan and poly(2-ethyl-2-oxazoline) for ocular drug delivery of ciprofloxacin. *J Drug Deliv Sci Technol* **74**, (2022).
30. Eid, H. M., Naguib, I. A., Alsantali, R. I., Alsalahat, I., Hegazy, A. M. Novel Chitosan-Coated Niosomal Formulation for Improved Management of Bacterial Conjunctivitis: A Highly Permeable and Efficient Ocular Nanocarrier for Azithromycin. *J Pharm Sci* **110**, 3027–3036 (2021).
31. Cu, Y., Booth, C. J., Saltzman, W. M. In vivo distribution of surface-modified PLGA nanoparticles following intravaginal delivery. *Journal of Controlled Release* **156**, 258–264 (2011).
32. Amin, M. K., Boateng, J. Surface functionalization of PLGA nanoparticles for potential oral vaccine delivery targeting intestinal immune cells. *Colloids Surf B Biointerfaces* **222**, (2023).
33. Zhou, J., Li, M., Chen, Q., Li, X., Chen, L., Dong, Z., Zhu, W., Yang, Y., Liu, Z., Chen, Q. Programmable probiotics modulate inflammation and gut microbiota for inflammatory bowel disease treatment after effective oral delivery. *Nat Commun* **13**(1), 3432 (2022).

34. Yang, M., Lai, S. K., Yu, T., Wang, Y. Y., Happe, C., Zhong, W., Zhang, M., Anonuevo, A., Fridley, C., Hung, A., Fu, J., Hanes, J. Nanoparticle penetration of human cervicovaginal mucus: The effect of polyvinyl alcohol. *Journal of Controlled Release* **192**, 202–208 (2014).
35. Dünnhaupt, S., Kammona, O., Waldner, C., Kiparissides, C., Bernkop-Schnürch, A. Nano-carrier systems: Strategies to overcome the mucus gel barrier. *Eur J Pharm Biopharm* **96**, 447–453 (2015).
36. Crater, J. S., Carrier, R. L. Barrier Properties of Gastrointestinal Mucus to Nanoparticle Transport. *Macromol Biosci* **10(12)**, 1473–1483 (2010).
37. Wang, L., Dong, J., Chen, J., Eastoe, J., Li, X. Design and optimization of a new self-nanoemulsifying drug delivery system. *J Colloid Interface Sci* **330**, 443–448 (2009).
38. Dünnhaupt, S., Kammona, O., Waldner, C., Kiparissides, C., Bernkop-Schnürch, A. Nano-carrier systems: Strategies to overcome the mucus gel barrier. *Eur J Pharm Biopharm* **96**, 447–453 (2015).
39. Gursoy, R. N., Benita, S. Self-emulsifying drug delivery systems (SEDDS) for improved oral delivery of lipophilic drugs. *Biomed Pharmacother* **58**, 173–182 (2004).
40. Bayer, I. S. Recent Advances in Mucoadhesive Interface Materials, Mucoadhesion Characterization, and Technologies. *Adv Mater Interfaces* **9(18)**, 2200211 (2022).
41. Rossi, S., Vigani, B., Sandri, G., Bonferoni, M. C., Caramella, C. M., Ferrari, F. Recent advances in the mucus-interacting approach for vaginal drug delivery: from mucoadhesive to mucus-penetrating nanoparticles. *Expert Opin Drug Deliv* **16**, 777–781 (2019).
42. Li, J., Mooney, D. J. Designing hydrogels for controlled drug delivery. *Nat Rev Mater* **1**, 16071 (2016).
43. Su, J., Hu, B. H., Lowe, W. L., Kaufman, D. B., Messersmith, P. B. Anti-inflammatory peptide-functionalized hydrogels for insulin-secreting cell encapsulation. *Biomaterials* **31**, 308–314 (2010).
44. Reichert, J. M. Trends in development and approval times for new therapeutics in the United States. *Nat Rev Drug Discov* **2(9)**, 695–702 (2009).
45. Cao, L., Lu, W., Mata, A., Nishinari, K., Fang, Y. Egg-box model-based gelation of alginate and pectin: A review. *Carbohydr Polym* **242**, 116389 (2020).
46. Lee, K. Y., Mooney, D. J. Alginate: Properties and biomedical applications. *Progress in Polymer Science* **37**, 106–126 (2012).
47. Rinaudo, M. Chitin and chitosan: Properties and applications. *Progress in Polymer Science* **31**, 603–632 (2006).
48. Bhattarai, N., Gunn, J., Zhang, M. Chitosan-based hydrogels for controlled, localized drug delivery. *Adv Drug Deliv Rev* **62**, 83–99 (2010).
49. Prabaharan, M., Mano, J. F. Chitosan-Based Particles as Controlled Drug Delivery Systems. *Drug Deliv* **12**, 41–57 (2004).
50. Huang, X., Brazel, C. S. Analysis of burst release of proxiphylline from poly(vinyl alcohol) hydrogels. *Chem Eng Commun* **190(4)**, 519–532 (2003).
51. Caliari, S. R., Burdick, J. A. A practical guide to hydrogels for cell culture. *Nat Methods* **13**, 405 (2016).
52. Zhang, S., Ermann, J., Succi, M. D., Zhou, A., Hamilton, M. J., Cao, B., Korzenik, J. R., Glickman, J. N., Vemula, P. K., Glimcher, L. H., Traverso, G., Langer, R., Karp, J. M. An inflammation-targeting hydrogel for local drug delivery in inflammatory bowel disease. *Sci Transl Med* **7**, 300 (2015).
53. Oliva, N., Conde, J., Wang, K., Artzi, N. Designing Hydrogels for On-Demand Therapy. *Acc Chem Res* **50**, 669–679 (2017).
54. Grijalvo, S., Mayr, J., Eritja, R., Díaz Díaz, D. Biodegradable liposome-encapsulated hydrogels for biomedical applications: a marriage of convenience. *Biomater Sci* **4**, 555 (2016).
55. Correa, S., Grosskopf, A. K., Klich, J. H., Lopez Hernandez, H., Appel, E. A. Injectable liposome-based supramolecular hydrogels for the programmable release of multiple protein drugs. *Matter* **5**, 1816–1838 (2022).
56. Eibl, H. Phospholipids as Functional Constituents of Biomembranes. *Angew Chem Int* **23**, 257–271 (1984).
57. Israelachvili, J. N., Marcelja, S., Horn, R. G., Israelachvili, J. N. Physical principles of membrane organization. *Q Rev Biophys* **13**, 121–200 (1980).
58. Patil, Y. P., Jadhav, S. Novel methods for liposome preparation. *Chem Phys Lipids* **177**, 8–18 (2014).
59. Reeves, J. P., Dowben, R. M. Formation and properties of thin-walled phospholipid vesicles. *J Cell Physiol* **73**, 49–60 (1969).
60. Angelova, M. I., Dimitrov, D. S. Liposome Electroformation. *Faraday Discuss. Chem. SOC* **81**, 303–311 (1986).
61. Huang, C., Quinn, D., Sadovsky, Y., Suresh, S., Hsia, K. J. Formation and size distribution of self-assembled vesicles. *PNAS* **114(11)**, 2910–2915 (2017).
62. Akbarzadeh, A., Rezaei-Sadabady, R., Davaran, S., Joo, S. W., Zarghami, N., Hanifepour, Y., Samiei, M., Kouhi, M., Nejati-Koshki, K. Liposome: classification, preparation, and applications. *Nanoscale Res Lett* **8(1)**, 102 (2013).
63. Bozzuto, G., Molinari, A. Liposomes as nanomedical devices. *Int J Nanomedicine* **10**, 975–999 (2015).
64. Sercombe, L., Veerati, T., Moheimani, F., Wu, S. Y., Sood, A. K., Hua, S. Advances and Challenges of Liposome Assisted Drug Delivery. *Front Pharmacol* **6**, 286 (2015).
65. Ulrich, A. S. Biophysical Aspects of Using Liposomes as Delivery Vehicles. *Biosci Rep* **22**, 129–150 (2002).
66. Monteiro, N., Martins, A., Reis, R. L., Neves, N. M. Liposomes in tissue engineering and regenerative medicine. *J R Soc Interface* **11(101)**, 20140459 (2014).
67. Hua, S., Wu, S. Y. The use of lipid-based nanocarriers for targeted pain therapies. *Front Pharmacol* **21(4)**, 143 (2013).
68. Hua, S. Targeting sites of inflammation: intercellular adhesion molecule-1 as a target for novel inflammatory therapies. *Front Pharmacol* **4(4)**, 127 (2013).
69. Mezzenga, R., Seddon, M., Drummon, C., Boyd, C. J., Schroder-Turk, G. E., Segalowicz, L. Nature-inspired design and applications of lipidic lyotropic liquid crystals. *Adv Materials* **31**, 1900818 (2019).
70. Assenza, S., Mezzenga, R. Curvature and bottlenecks control molecular transport in inverse bicontinuous cubic phases. *J. Chem. Phys* **148**, 54902 (2018).
71. Mezzenga, R., Seddon, M., Drummon, C., Boyd, C. J., Schroder-Turk, G. E., Segalowicz, L. Nature-Inspired Design and Application of Lipidic Lyotropic Liquid Crystals. *Adv Materials*, **31** 1900818 (2019).



72. Aleandri, S., Mezzenga, R. The physics of lipidic mesophase delivery systems *Physics Today* **73(7)**, 38 (2020).
73. Leser, M. E., Sagalowicz, L., Michel, M., Watzke, H. J. Self-assembly of polar food lipids. *Adv Colloid Interface Sci* **123(126)**, 125–136 (2006).
74. Mezzenga, R., Meyer, C., Servais, C., Romoscanu, A. I., Sagalowicz, L., Hayward, R. C. Shear rheology of lyotropic liquid crystals: A case study. *Langmuir* **21**, 3322–3333 (2005).
75. Guo, C., Wang, J., Cao, F., Lee, R. J., Zhai, G. Lyotropic liquid crystal systems in drug delivery. *Drug Discov Today* **15**, 1032–1040 (2010).
76. Elzenaty, O., Luciani, P., Aleandri, S. A lipidic mesophase with tunable release properties for the local delivery of macromolecules: the apoferritin nanocage, a case study. *J Mater Chem B* **10**, 3876–3885 (2022).
77. Manni, L. S., Zabara, A., Yazmin, M., Osornio, J., Schoppe, D., Batyuk, A., Pluckthun, A., Siegel, J. S., Mezzenga, R. Lipid synthesis phase behavior of a designed cyclopropyl analogue of monoolein: implications for low temperature membrane protein crystallization. *Ang Chemie* **54(3)**, 1027-1031 (2015).
78. Kim, H., Leal, C. Cuboplexes: Topologically Active siRNA Delivery. *ACS Nano* **9(10)**, 10214- 10226 (2015).
79. Martiel, I., Baumann, N., Vallooran, J. J., Bergfreund, J., Sagalowicz, L., Mezzenga, R. Oil and drug control the release rate from lyotropic liquid crystals. *J Control Release* **204**, 78–84 (2015).
80. Sagalowicz, L., Leser, M. E., Watzke, H. J., Michel, M. Monoglyceride self-assembly structures as delivery vehicles. *Trends Food Sci Technol* **17**, 204–214 (2006).
81. Boyd, B. J., Whittaker, D. v., Khoo, S. M., Davey, G. Hexosomes formed from glycerate surfactants-Formulation as a colloidal carrier for irinotecan. *Int J Pharm* **318**, 154–162 (2006).
82. Cervin, C., Vandoolaeghe, P., Nistor, C., Tiberg, F. , Johnsson, M. A combined in vitro and in vivo study on the interactions between somatostatin and lipid-based liquid crystalline drug carriers and bilayers. *Eur J Pharm Sci* **36**, 377–385 (2009).
83. Libster, D., Aserin, A., Wachtel, E., Shoham, G., Garti, N. An HII liquid crystal-based delivery system for cyclosporin A: Physical characterization. *J Colloid Interface Sci* **308**, 514–524 (2007).
84. Lopes, L. B. Reverse Hexagonal Phase Nanodispersion of Monoolein and Oleic Acid for Topical Delivery of Peptides: in Vitro and in Vivo Skin Penetration of Cyclosporin A. *Pharm Research* **23**, 1332-1342 (2006).
85. Nielsen, L. S., Schubert, L., Hansen, J. Bioadhesive drug delivery systems: I. Characterisation of mucoadhesive properties of systems based on glyceryl mono-oleate and glyceryl monolinoleate. *Eur Journal Pharm Sci* **6**, 231–239 (1998).
86. Han, S., Shen, J. Q., Gan, Y., Geng, H. M., Zhang, X. X., Zhu, C. L., Gan, L. Novel vehicle based on cubosomes for ophthalmic delivery of flurbiprofen with low irritancy and high bioavailability. *Acta Pharmacol Sin* **31**, 990–998 (2010).
87. Fong, W. K., Hanley, T., Boyd, B. J. Stimuli responsive liquid crystals provide ‘on-demand’ drug delivery in vitro and in vivo. *J Control Release* **135**, 218–226 (2009).
88. Ki, M. H., Lim, J. L., Ko, J. Y., Park, S. H., Kim, J. E., Cho, H. J., Park, E. S., Kim, D. D. A. new injectable liquid crystal system for one month delivery of leuprolide. *J Control Release* **185**, 62–70 (2014).
89. Shah, M. H., Biradar, S. V., Paradkar, A. R. Spray dried glyceryl monooleate-magnesium trisilicate dry powder as cubic phase precursor. *Int J Pharm* **323**, 18–26 (2006).

## Chapter 2

### Temperature-triggered *in situ* forming lipid mesophase gel for local treatment of ulcerative colitis

Marianna Carone<sup>1</sup>, Marianne R. Spalinger<sup>2</sup>, Robert A. Gaultney<sup>3</sup>, Raffaele Mezzenga<sup>4</sup>, Kristýna Hlavačková<sup>3</sup>, Aart Mookhoek<sup>3</sup>, Philippe Krebs<sup>3</sup>, Gerhard Rogler<sup>2</sup>, Paola Luciani<sup>1</sup>, Simone Aleandri<sup>1</sup>

#### **Affiliations:**

<sup>1</sup> Department of Chemistry, Biochemistry and Pharmaceutical Sciences, University of Bern, Bern, Switzerland

<sup>2</sup> Department of Gastroenterology and Hepatology, University Hospital Zurich, University of Zurich, Zurich, Switzerland

<sup>3</sup> Institute of Tissue Medicine and Pathology, University of Bern, Bern, Switzerland

<sup>4</sup> Laboratory of Food & Soft Materials, Institute of Food, Nutrition and Health, IFNH; Department for Health Sciences and Technology, D-HEST, ETH Zurich, Switzerland

Paola Luciani, Simone Aleandri contributed with the conceptualization and small angle X ray experiments. Raffaele Mezzenga contributed with the revisions to the manuscript. The *in vivo* experiments for T cell transfer-induced colitis mice model were collaboratively planned and performed by Marianne R. Spalinger and Gerhard Rogler, while Robert A. Gaultney, Kristýna Hlavačková, Aart Mookhoek and Philippe Krebs collaboratively planned and performed the experiments for dextrane sulfate sodium-induced colitis mice model.

*Patent applicant:* University of Bern and University of Zurich

*Name of inventor(s):* Marianna Carone, Marianne R. Spalinger, Robert A. Gaultney, Philippe Krebs, Gerhard Rogler, Paola Luciani, Simone Aleandri.

*Application number:* European Patent Application No 22197842.3

*Status of application:* The above application has been filed with the European Patent Office (EPO)

This chapter is currently under review as ‘Temperature-triggered *in situ* forming lipid mesophase gel for local treatment of ulcerative colitis’.

## 1. Introduction

Ulcerative colitis (UC) is a chronic remitting-relapsing inflammatory disorder of the large intestine, involving the colonic and rectal mucosa<sup>1</sup>. Clinically, 75% of patients suffer from left-sided colitis or proctitis but the inflammation can spread upward in a continuous manner and involves the colon partially or entirely<sup>2</sup>. There is no known cure for UC and the chronic relapse and remission often result in patient disability<sup>1,2</sup>.

All treatments currently recommended by the European Crohn's and Colitis Organization (ECCO) and American Gastroenterological Association (AGA) struggle to deliver the desired remission rates, and many patients must cycle through several different therapies to achieve remission<sup>3,4</sup>. Following a step-up approach, the first line treatment of mild to moderate left-sided UC or pancolitis is 5-aminosalicylic acid (5-ASA, combined topical and oral administration) for the induction of remission. For refractory patients and in severe disease cases, systemic corticosteroids, azathioprine, 6-mercaptopurine, monoclonal antibodies (such as infliximab, an anti TNF- $\alpha$ ; vedolizumab, an anti  $\alpha\beta_7$  integrin; and ustekinumab, IL-12/IL-23 blockade) and ozanimod (a sphingosine 1-phosphate receptor modulator) are the treatments of choice to obtain remission<sup>4-8</sup>. Biological-based therapies may have considerable side effects including systemic toxicity, resulting in recurrence of opportunistic infections, psoriasis, a lupus-like syndrome, and loss of response to therapy over time<sup>9-13</sup>.

Recently, tofacitinib (TOFA), a small-molecule inhibitor of the enzymes Janus kinase 1 and 3 (JAK3 and JAK1, respectively)<sup>14</sup>, was approved by European and US regulators for the oral treatment of UC in patients who had intolerance or a loss of response to biologic drugs. Its oral administration is preferred by many patients as compared to biologics in maintenance of remission and endoscopic improvement<sup>15,16</sup>. In steroid-refractory UC, the use of tacrolimus (TAC) – a macrolide that inhibits T-lymphocyte activation – is recommended<sup>17</sup>. TOFA and TAC, however, showed dose-dependent adverse effects when administered systemically (e.g., nephrotoxicity, thromboembolic complications, headache, metabolic disorders) in a significant fraction of patients<sup>18-21</sup>, which may require discontinuation of the treatment in some cases and limits the dosages that can be administered<sup>21</sup>. Taken together, the side effects of these systemically administered drugs must be weighed in patient management against the potential benefits of UC treatment. If not for the limiting side effects, higher drug concentrations would likely have a higher efficacy. The specific localization of the disease to the colon encourages the use of topical therapies<sup>22</sup>. Indeed, delivery via the rectal route is a safe therapeutic approach that can maximize the drug concentration directly at the site of inflammation while minimizing systemic exposure. 5-ASA or budesonide in rectal preparations as enema or foam are routinely used as first-line treatment for UC<sup>23,24</sup>. The rectal administration of 5-ASA in UC

patients has been shown to be significantly more efficient than oral administration<sup>25–30</sup>. The efficacy of rectal administration is further supported by the finding that steroid-refractory ulcerative proctitis has been managed by topically administered TAC as ointment<sup>27,31</sup>, suppository<sup>32</sup> or enema<sup>20,21,30</sup>. Although clinical studies have shown that rectal 5-ASA preparations are more effective than oral preparations, these treatments are still rarely prescribed<sup>33</sup>. The efficacy of conventional enema-based formulations is intrinsically limited by their insufficient retention in the colon<sup>34</sup> and faecal urgency associated with the large volumes administered<sup>35</sup>. The required retention time – at least 20 minutes – together with frequent dosing negatively affect patient compliance<sup>36</sup>.

To address these drawbacks, and to improve either the performance of the topical formulation or the therapeutic outcome of the delivered drug, we propose, herein, a gel platform that employs rectal temperature as a trigger for the formation of a highly viscous adhesive depot system (TIF-Gel). TIF-Gel is a lipidic mesophase (LMP) based formulation, a versatile delivery system able to protect and release the incorporated drugs slowly *in vivo*<sup>37,38</sup>. Upon hydration, monoacylglycerol lipids such as monolinolein (MLO, generally recognized as safe for human and/or animal use by the FDA) can self-assemble in different arrangements. By increasing the water content, the less viscous lamellar (*L*) phase transforms first to an *Ia3d* and then to a *Pn3m* cubic phase (*Q*) which are similar in appearance and rheology to a high viscous cross-linked hydrogel<sup>39</sup>. To overcome the hurdle of administering a highly viscous gel, not only water<sup>40</sup> but also temperature can be used as a trigger to tune the viscosity of the system. Increasing the system's temperature, indeed, induces a transition from the *L* phase to a *Q* phase (with *Ia3d* symmetry)<sup>39,41</sup>. Considering the peculiarity of the rectal milieu, characterized by a low volume and with a composition highly affected by age, biological sex and pathology<sup>42</sup>, water is not the most suitable trigger for an *in-situ* gelation. Thus, rectal temperature is the ideal condition to activate the transformation of the precursor *L* phase into the cubic phase gel. The TIF-Gel was then loaded with the hydrophilic TOFA, or hydrophobic TAC and the therapeutic suitability of the drug-loaded TIF-Gel was tested and validated *in vivo* in the contexts of chemically and T cell transfer induced colitis in mice—two established models of inflammatory bowel disease (IBD)<sup>43,44</sup>. Results demonstrate that our TIF-Gel provides a valuable approach to effectively administer these drugs locally to the inflamed colonic mucosa resulting in sustained drug release. Furthermore, our findings suggest that the TIF-Gel may enhance the localized activity of these anti-inflammatory drugs while potentially reducing the risk of side effects. Thanks to the higher viscosity that the gel develops in the rectal environment, we observed a low leakage of the gel after administration in mice. Overall, we expect that our TIF-Gel may translate to a topical mucosal therapy with high patient friendliness, concomitantly decreasing problems with retention, bloating, and urgency, and therefore increasing medical adherence.

## 2. Materials and methods

### *Materials*

Monolinolein (MLO) was purchased by NU-Check Prep, Inc. (MN, USA). Ultrapure water of resistivity 18.2 M $\Omega$ .cm was produced by Barnstead Smart2pure (Thermo scientific) and used as the aqueous phase. Methanol, acetonitrile, and tetrahydrofuran were analytical grade supplied by Fisher Scientific (Schwerte, Germany). Ethanol absolute >99.5 wt% was obtained from VWR chemicals BDH (London, UK). Tofacitinib citrate (TOFA) was purchased by LC laboratories (Woburn, MA) and tacrolimus (TAC) was obtained from R&S Pharmchem Co., Ltd (Shanghai, China). The lipase from porcine pancreas and methyl cellulose (viscosity 25 cp) were obtained from Sigma Chemical Co. (St. Louis, USA). Caffeine (Ph. Eur. Quality) was purchased from Hanseler Swiss Pharma. HEPES salt was obtained from Carl Roth (Karlsruhe, Germany).

### *Gel preparation*

MLO was used as the lipid component of the mesophases and mixed with TOFA (5 % w/w; 5 mg/100 mg) or TAC (1% w/w; 1 mg/100 mg). Lipid/drug mixtures were prepared by dissolving the appropriate amounts of lipid and drug stock solutions together in ethanol. The solvent was then completely removed under reduced pressure (freeze-drying for 24 h at 0.22 mbar) and the dried lipid mixture was hydrated by mixing weighed amounts of water in sealed Pyrex tubes and alternatively centrifuging (10 min, 5000 g) several times at room temperature until a homogenous mixture was obtained. The mesophase was then equilibrated for 48 h at room temperature in the dark. For *in vivo* studies, after 48 h equilibration (as described above) the formulation was loaded into a 1-mL syringe (Injekt-F, Braun) and the dead volume of the animal feeding needle (20G, L  $\times$  diam. 1.5 in.  $\times$  1.9 mm) for rectal administration was calculated so that exactly 100 mg was applied (in the Appendix, **A1.1**).

### *Small angle X-ray scattering*

SAXS measurements were used to determine the phase identity and symmetry of the produced LMPs. Measurements were performed on a Bruker AXS Micro, with a microfocused X-ray source, operating at voltage and filament current of 50 kV and 1000  $\mu$ A, respectively. The Cu K $\alpha$  radiation ( $\lambda_{\text{Cu K}\alpha} = 1.5418 \text{ \AA}$ ) was collimated by a 2D Kratky collimator, and the data were collected by a 2D Pilatus 100K detector. The scattering vector  $Q = (4\pi/\lambda) \sin \theta$ , with  $2\theta$  being the scattering angle, was calibrated using silver behenate. Data were collected and azimuthally averaged using the Saxsgui software to yield 1D intensity vs. scattering vector  $Q$ , with a  $Q$  range from 0.001 to 0.5  $\text{\AA}^{-1}$ . For all

measurements, the samples were placed inside a stainless-steel cell between two thin replaceable mica sheets and sealed by an O-ring, with a sample volume of 10  $\mu\text{L}$  and a thickness of  $\sim 1$  mm. Measurements were performed at 25, 30, 34, 36 and 38  $^{\circ}\text{C}$ . Samples were equilibrated for 10 min before measurements whereas scattered intensity was collected over 30 min and over 60 min in case of lamellar phase. On the other hand, for the kinetic study, the sample was pre equilibrated at 25  $^{\circ}\text{C}$  and inserted in the sample holder kept at 38  $^{\circ}\text{C}$  and the scattered intensity collected over 5 min. To determine the structural parameters such as the size of the water channels, SAXS data information on the lattice were combined with the composition of the samples<sup>39</sup>.

### *Rheology experiments*

A stress-controlled rheometer (Modular Compact Rheometer MCR 72 from Anton Paar, Graz, Austria) was used in cone-plate geometry,  $0.993^{\circ}$  angle, and 49.942 mm diameter. The temperature control was set either at 25 or 38  $^{\circ}\text{C}$ . First, a strain sweep was performed at 1 Hz between 0.002 and 100% strain to determine the linear range. Then, oscillatory frequency sweeps were performed at 0.1% strain between 0.1 and 100 rad/s. Frequency sweep measurements were performed at a constant strain in the linear viscoelastic regime (LVR), as determined by the oscillation strain sweep (amplitude sweep) measurement performed for each sample. Within the linear viscoelastic region, in fact, the material response is independent of the magnitude of the deformation and the material structure is maintained intact; this is a necessary condition to accurately determine the mechanical properties of the material.

### *Release experiments: in vitro and ex vivo set-up and HPLC drug quantification.*

Formulations and free drug enema were tested *in vitro* and *ex vivo* with vertical diffusion cells (PermeGear, Pennsylvania, USA) using a 3000 nm polycarbonate membrane (Sterlitech Corporation, USA). HEPES buffer (8 mL) with a pH 7.4 or HEPES buffer enriched with 10% (v/v) of EtOH was used as the release medium for TOFA and TAC, respectively and the device was placed in a shaking incubator at 100 rpm and 37  $^{\circ}\text{C}$ . To investigate the effect of lipase on drug release, porcine pancreatic lipase (1000 U/mL,) was added to the sample in the donor chamber. *Ex vivo* experiments were performed using rat intestinal tissue to evaluate the drug release of our TIF-Gel. Briefly, fresh intestinal tissue was obtained and cut into suitable samples (2mm\*1mm\*1mm) for Franz cell apparatus. Tissue was placed on the polycarbonate membrane for tensile loading. At designated time points (0.5, 1, 1.5, 2, 3, 4, 5, 6, 7, 8 h), the release medium (HEPES buffer with a pH 7.4 in case of TOFA or HEPES buffer enriched with 30% (v/v) EtOH in case of TAC) was completely replaced with 8 mL of fresh medium, and 1 mL aliquot was taken for lyophilization. Each sample was resuspended with internal standard in the mobile phase and the drug content was analysed by HPLC

(in the Appendix, **A1.2**). The same experimental design was used for both formulations. Moreover, samples of TIF-Gel containing drug were stored at room temperature and 4 °C for 30 days. The drug stability was determined by HPLC analysis. The same experimental design was used for both drugs.

### *In vivo investigation*

#### *Chemically induced colitis based on application of DSS*

Female 6-8 week-old C57B/6J mice were ordered from Charles River Germany and maintained under specific and opportunistic pathogen-free (SOPF) microbiota conditions at the animal facility of the University of Bern. Mice were ear-marked, randomly assigned to different cages and treatment groups, and bedding mixed between all cages to avoid potential cage effects on microbiota. All methods used were approved by the Bernese animal welfare authority (permission no. BE 20/18). One day prior to the start of DSS supplementation, mice were intra-rectally injected with 100 µL of empty gel, TOFA in 1% methylcellulose, or gel loaded with drug (5 mg /100 µL).

The next day, drinking water was supplemented with 2% w/v dextran sodium sulfate (DSS; MP Biomedicals, 160110). Every other day, the different compounds were applied intra-rectally until the end of the experiment. During the experiment, the mice were constantly monitored, and the weight and disease scores were recorded when appropriate. Disease score was determined by grading of 1-4 of the following criteria (with grade 4 corresponding to most unhealthy/abnormal): posture, mobility, fur appearance, weight, stool consistency, and stool color, as previously described<sup>45</sup>. At the termination of the experiment, mice were euthanized by asphyxia with carbon dioxide, and organs were collected and used as described in the results. Swiss rolls<sup>46</sup> were made from the colons, fixed overnight with 10% formalin in PBS, then washed with PBS, embedded in paraffin, and sectioned with H&E staining. Histopathology scoring was performed by board-certified pathologist, in a blinded manner, using the following criteria: loss of goblet cells, crypt abscesses, epithelial erosions, hyperemia, thickness of mucosa, and cellular infiltration (maximal score for each criterion: 3)<sup>47</sup>.

#### *Flow cytometry and quantification of single cells*

The gating strategy was adapted from previously published work<sup>48</sup>. Briefly, mouse spleens (after weighing) and mesenteric lymph nodes were homogenized through a 70 µm cell strainer, after which point the red blood cells were removed from the spleen by re-suspending the cell pellet in ACK lysing buffer (150mM NH<sub>4</sub>Cl, 10mM KHCO<sub>3</sub>, 0.1mM; pH: 7.4) at room temperature for 5 min. Splenocytes were quantified using a CASY cell counter (Omni Life Sciences) and the following populations were quantified following single cell and live/dead selection (Thermofischer, L34961). T cells (defined as CD3ε+ cells; antibody used: eBioscience, 25-0031-82); dendritic cells (CD11c+, CD11b+; Biolegend

117324 & 101241); neutrophils (CD11b+; Ly6G+; Biolegend, B156884), macrophages (CD11b+, CD11c-, Ly6G-, Ly6C-), and inflammatory monocytes (CD11b+, Ly6C+; Biolegend, 128024). Stained cells were analysed on a BD BioscienceLSR II SORP flow cytometer.

#### *T-cell transfer colitis*

To induce T cell mediated colitis, CD4+ T cells were isolated from the spleen of C57/BL6 mice using the CD4 T cell isolation kit from Stemcell Technologies (# 19852; Cologne, Germany) and subsequently naïve T helper cells (CD3+, CD4+, CD25<sup>low</sup>, CD6L<sup>high</sup>, CD44<sup>low</sup> cells) were sorted on a FACS Aria III (Becton Dickinson; Eysins, Switzerland). 12–15-week-old male and female *Rag*<sup>-/-</sup> mice in the C57/BL6 background (originally purchased from Taconic from which a local colony was maintained in our vivarium) were injected intraperitoneally with 2.5 x10<sup>5</sup> naïve T helper cells. Mice (6 animals/group) were randomly assigned to different cages and treatment groups and bedding mixed between all cages to avoid potential cage effects on microbiota. All methods used were approved by the animal welfare authority (permission no. ZH043/2021). Starting on day 3 post T cell injection, mice received rectal instillations (100 µL) of empty TIF-Gels, TAC-loaded TIG-Gels or TAC in vehicle solution (1% nitrocellulose in distilled water) once per day until the end of the experiment. Weight development and disease activity scores were measured daily. On the last day of the experiment (day 18), the mice were anaesthetized using a mixture of ketamine 90–120 mg/kg bodyweight (Vétoquinol, Bern, Switzerland) and xylazine 8 mg/kg bodyweight (Bayer, Lyssach, Switzerland) and subjected to mouse endoscopy to assess the extent of endoscopic colitis as described previously<sup>49</sup> using the following parameters: 1) thickening of the colon wall, 2) vascularization/bleeding, 3) extent of fibrin deposits, 4) granular appearance of the colon wall, 5) stool consistency. Each parameter was given a score from 0 (normal) to 3 (most severe appearance), resulting in a maximal total score of 15. After colonoscopy, the mice were sacrificed, and colon tissue harvested for histology and isolation of *lamina propria* immune cells. Immune cells were isolated from the colon, mesenteric lymph nodes and the spleen, and analyzed for immune cell subsets as described previously<sup>50</sup>.

#### *H&E staining and histological analysis of colitis severity*

To assess the microscopic extent of colitis, formalin-fixed, paraffin embedded sections of the most distal 1.5 cm of the colon were subjected to hematoxylin and eosin (H&E) staining using standard protocols<sup>49</sup>. The sections were analyzed by two blinded scientists for the extent of epithelial damage (score 0-4) and infiltration of immune cells (score 0-4) resulting in a maximal possible score of 8. Images were taken using a Zeiss Axio Imager.Z2 microscope (Zeiss), equipped with an AxioCam HRc (Zeiss, Jena, Germany) camera and ZEN imaging software (Zeiss, Germany).



### *Pharmacokinetics (PK)*

The PK studies in healthy animals were performed by the Platform of Biopharmacy of the University of Montreal in accordance with local animal welfare committee of the University of Montreal and in agreement with regulations of the Canadian Council on Animal Care (CCAC). Healthy mice (female C57/BL6 mice; 5 animals/group) received under anesthesia a single administration (100  $\mu$ L) of either drug-loaded TIF-Gel (TIF-Gel-TOFA and TIF-Gel-TAC) or free drugs (TOFA and TAC in suspension). All the formulations contain 5 mg of TOFA and 1 mg of TAC and they were applied once at t=0 rectally and plasma levels were determined after 0.25, 1, 2, 4, 6, 12, 24 and 48 h. Animals were euthanized after the last sampling point with CO<sub>2</sub> (slow fill rate and organ harvesting performed after confirmation of death). Blood was collected and stored in K2-EDTA BD-Microtainer™ (Fisher Scientific AG, Switzerland), centrifuged at 4 °C, at 3000 g for 5 min and the obtained plasma (15  $\mu$ L) stored at -20 °C. Drugs were extracted from plasma and their concentration was determined in the obtained clear supernatant using LC-MS/MS analysis (in the Appendix, **A1.3**) and AUC<sub>0-48h</sub> were calculated according to the trapezoid method.

### 3. Results and discussion

Since the potential benefits of parenteral drug administration must always be weighed against concomitant side effects, due to systemic circulation of the drug, the management of UC does not simply rely on the choice of a timely pharmacological treatment<sup>51</sup>. The localization of the disease should indeed encourage the pursuit of a rectal administration through which the drug directly reaches the site of inflammation with minimal systemic exposure<sup>36</sup>. Among the various acyl glycerol lipids capable of forming lipidic mesophases in water via self-assembly, we selected MLO. MLO is an acyl glycerol lipid extensively used for drug encapsulation due to its ability to form lipidic mesophases in water via self-assembly. It has unique phase diagrams that lack coexistence of mesophases at any temperature and water content<sup>52</sup>, and it has been affirmed as Generally Recognized as Safe (GRAS) by the US FDA for human and animal use.

#### *Physico-chemical characterization of TAC- and TOFA-loaded TIF-Gel*

We designed and developed a gel formulation based on the concept that at 25 °C, and in the presence of a low percentage of water, MLO forms a lamellar (*L*) phase with a lower structural strength with

respect to the cubic phase ( $Q$ ), resulting in a formulation easier to administer and more able to treat remote tissue areas, as depicted in **Figure 1a**.

As a first step, we used small angle X-ray scattering (SAXS) measurements to determine the optimal amount of water needed to obtain a lamellar phase which provides a transition to the cubic phase at 38 °C (**Figure 1b and 1c**). The X-ray beam directed at the gel results in a scattering pattern with a set of maxima that correspond to sharp Bragg reflections characteristic of the long-range positional order. The sequence of Bragg reflections (and their ratio; listed in **Figure 1a**) identifies the symmetry of the mesophase studied<sup>53</sup>.

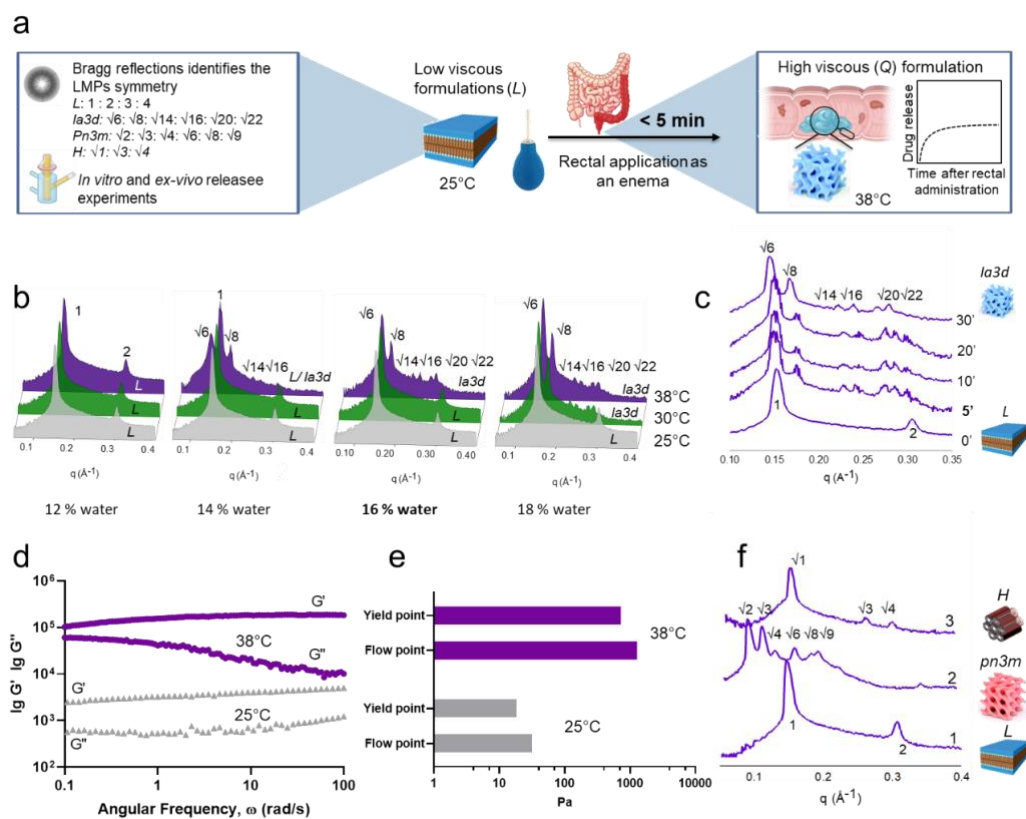


**Figure 1:** *In vitro* characterizations of the TIF-Gel: a) schematic depiction of the *in vitro* characterization and the mechanism of the gel formation. b) SAXS spectra acquired at different temperatures (25, 30 and 38 °C; bottom, middle and top spectra, respectively) on gels containing increasing amount of water (12%, 14%, 16% and 18 % w/w) and (c) SAXS spectra acquired at different times (5, 10, 20 and 30 min) after incubation at 38 °C; (d) frequency sweep at the end (purple symbols) and beginning (grey symbols) of the release experiments. (e) Flow and yield points obtained for lamellar phase (grey bars) and for cubic gel (purple bars). (f) SAXS before (1) and after incubation of LMPs in HEPES buffer (2) and in HEPES buffer enriched with 1000 U/mL of lipase (3). The LMPs cartoons (L; cubic ia3d, cubic pn3m and hexagonal) are adapted for Aleandri *et al.*<sup>38</sup>.

As shown in **Figure 1b**, with 12% water the Bragg reflections characteristic of L phase were present at 25 and 38 °C. Hydrating the MLO to 14% water led to a lamellar structure at 25 °C and a coexistence of L and Q structures (with an *Ia3d* geometry) at 38°, whereas increasing the amount of water up to 18% w/w induced the L → Q transition already at 30 °C. On the other hand, a mesophase composed by 16% w/w of water and 84% w/w of MLO gives Bragg reflections characteristic of the lamellar structure at 25 °C and a transition to a Q structure (with a *Ia3d* geometry) at 38°, i.e. the rectal temperature. The reflections characteristic of this L phase (containing 16 % water) adopt those characteristic of a Q phase after only 5 min of incubation at 38 °C (**Figure 1c**), indicating a rapid conversion of the lamellar precursor into the *Ia3d* cubic structure<sup>54</sup>, making it particularly suited for rectal administration. The transition is reversible if the temperature is brought back to 25 °C (in the Appendix, **A1.4**). While this information is not relevant for rectal applications *per se*, it is an important property for the storage conditions of TIF-Gel. In comparison to the available liquid crystal technology<sup>®</sup> developed by the Swedish company Camurus<sup>55,56</sup>, which consists of an alcoholic lipid solution that transforms to a gel upon contact with water, TIF-gel is not only dependent on water content, but also uses temperature as a trigger for an *in situ* gelation. This aspect is of particular relevance since the volume of rectal fluid is low and highly affected by age, biological sex and pathology.

The diverse topologies of the mesophases were confirmed by the different viscoelastic regimes identified by rheological (frequency sweep) measurements. Specifically, the precursor L phase had a low structural strength, as indicated by the lower value of storage modulus and loss modulus ( $G'$  and  $G''$ , respectively) with respect to the viscoelastic Q phase. This resulted in a less viscous pseudoplastic gel characterized by extensive energy dissipation mechanisms associated with the parallel slip of the lamellae. In simulated administration conditions, increasing the temperature and water availability resulted in swelling of the structure corresponding to a Q phase transition (where both  $G'$  and  $G''$  are higher than those obtained for L phase—**Figure 1d**). Moreover, either the flow or the yield points (both representing the shear limit above which a material starts to behave like a fluid) better determine the differences between our low viscous lamellar precursor and the high viscoelastic cubic gel and they might identify a threshold above which a formulation is too elastic to be rectally applied (**Figure 1e**). Since the sliding of a lamellae can occur along any possible direction, a low shear is required to be applied to this gel so that it starts behaving like a fluid and it can be forced to pass easily through a canula for enema, a syringe or a colon pipe. This translates into a low viscosity material with a low structural strength easier to administer compared to the fully hydrated cubic gel owing to its high flow and a yield point (in the Appendix, **A1.5**). On the other hand, the pseudoplastic precursor has a higher viscosity than commercially available enemas such as Asacol<sup>®</sup>,

Pentasa<sup>®</sup> and foam-containing 5-ASA and budesonide. Once applied, our TIF-Gel adheres to the colon wall and it is retained for at least 6 hours, a time needed to avoid loss of material <sup>39,57,58</sup> (in the Appendix, **A1.6**).

To prove the occurrence of the expected transition, a series of SAXS experiments was carried out after the gel was soaked in 1 mL of HEPES (or, alternatively, in a buffer solution containing lipase) and incubated at 38 °C for 8 h. As shown in Fig. 1f, the *L* phase absorbed heat and water during the release experiments reaching a cubic (*pn3m*) phase with a lattice parameters (*a*= 8.7 nm) and a water channel (*d<sub>w</sub>*= 4 nm) comparable with those obtained for a *Pn3m* phase at its maximum hydration level <sup>59</sup>. These transitions were also confirmed *in vivo* where, after rectal application, the gel excreted and collected with the stool after 30 min had an *Ia3d* phase identity, whereas the residual gel present in the colon after 6 h was determined to be in the *pn3m* cubic phase (in the Appendix, **A1.7**). The presence of lipase (100 U/mL) hydrolysed the ester group of MLO inducing a transition from *Q*→Hexagonal phase (*H*) <sup>60</sup>, with the latter not linked to a burst release phenomenon (**Figure 2**). Based on this initial characterisation, we chose an 84% MLO and 16% water formulation for subsequent *in vitro* and *in vivo* studies, which had suitable rheological properties to pass through a small diameter animal feeding needle (size 20 G) to further expand into a sponge-like system once injected into the rectum.

#### *Drugs are efficiently encapsulated and released from TIF-Gel*

In order to properly use TIF-Gel as a treatment option, the thermal characteristics of the LMP should not be perturbed by the guest drug. To evaluate the influence of the active principles on the phase identity, TOFA (a hydrophilic inhibitor of the JAK 1 and 3) and TAC (a hydrophobic immunosuppressive drug) loaded-mesophases were independently prepared and analyzed with SAXS. Notably, the entrapment of drugs (5 mg of TOFA or 1 mg of TAC in 100 mg of gel – 5 or 1% w/w, respectively) (**Figure 2a and 2b**) did not affect the phase identity and thermal behaviour of the carrier gel and the rectal temperature still induced a transition from *L*→*Q* phase (in the Appendix, **A1.8**). When hydrated with water, the lipid/drug mixtures form the lamellar structure and the totality of the drugs are embedded in the gel with a 100% encapsulation efficacy, differently from the recently developed hydrogel for local drug delivery in IBD in which a low proportion of dexamethasone was encapsulated<sup>61</sup>. These drug concentrations are higher than those contained in the commercially available enemas for UC treatment, which contain only 4% w/w of 5-ASA (in case of Asacol<sup>®</sup>) or 2% w/w of budesonide (for Budenofalk<sup>®</sup> and Entocort<sup>®</sup>). Moreover, both drugs do not form crystals once embedded in the 3D gel structure, as proven by the absence of reflections associated with a drug crystallization in the wide-angle X-ray scattering (WAXS) spectra. The drugs were also

homogeneously distributed in the gel matrix (in the Appendix, **A1.9**) and both - the tested drugs and the TIF-Gel - exhibit long-term stability (in the Appendix, **A1.10 and A1.11**).

In the *in vitro* release experiments, drug-loaded TIF-Gel formulations were placed in the donor chamber of a vertical Franz cell (a commonly used apparatus to assess the drug release from a semisolid dosage formulation in preclinical studies; depicted in **Figure 2**). Contrary to the small intestine, for which different *in vitro* models are established<sup>62-64</sup>, for colon tissues only animal models are available and are mostly used in pre-clinical studies<sup>65,66</sup>. To bypass this limitation, we employed an *ex vivo* approach in which tissues isolated from healthy rat colon were used as natural membrane<sup>67</sup>, replacing the polycarbonate membrane detailed above. The 3D gel network retains the TOFA (hydrophilic drug) and slowly releases it in both the *in vitro* and an *ex vivo* setups (**Figure 2b and 2c**, respectively). The same sets of experiments were also carried out for the TAC-loaded gel. Results for this hydrophobic drug mirrored those of the hydrophilic TOFA in both *in vivo* and *ex vivo* experiments, reflecting the flexibility of this vehicle (**Figure 2e and 2f**). Notably, the presence of lipase in our experimental conditions did not induce disassembly of the gel with consequent burst release of the drug, as reported for another lipid-based gel, developed to topically treat UC<sup>68</sup>. In this study, addition of the enzyme (*Thermomyces lanuginosus* lipase) induced a responsive release (+20% of drug released) from the hydrogel only after 24 h. In comparison, TAC and TOFA were released from our TIF-Gel within only 8 h, a time span more compatible with the retention time of rectally administered dosage forms. In 2015, Martiel et. al. developed the structural control efficiency index (SCEI)<sup>69</sup>, which provides an estimate of the kinetics of drug release for various phases. However, in our case, the phase identity of the gel changes dynamically during the release experiment. Thus, we cannot use the above-mentioned paradigm to describe the release profile. Indeed, our hydrophobic drugs do not follow a Fickian diffusion profile and, consequently, the release profile cannot be modeled using the Higuchi equation. We did not observe any gel erosion (no weight loss was recorded either *in vitro* or in *ex vivo* experiments) and we can, therefore, reject the hypothesis that the release process is driven by gel dissolution.

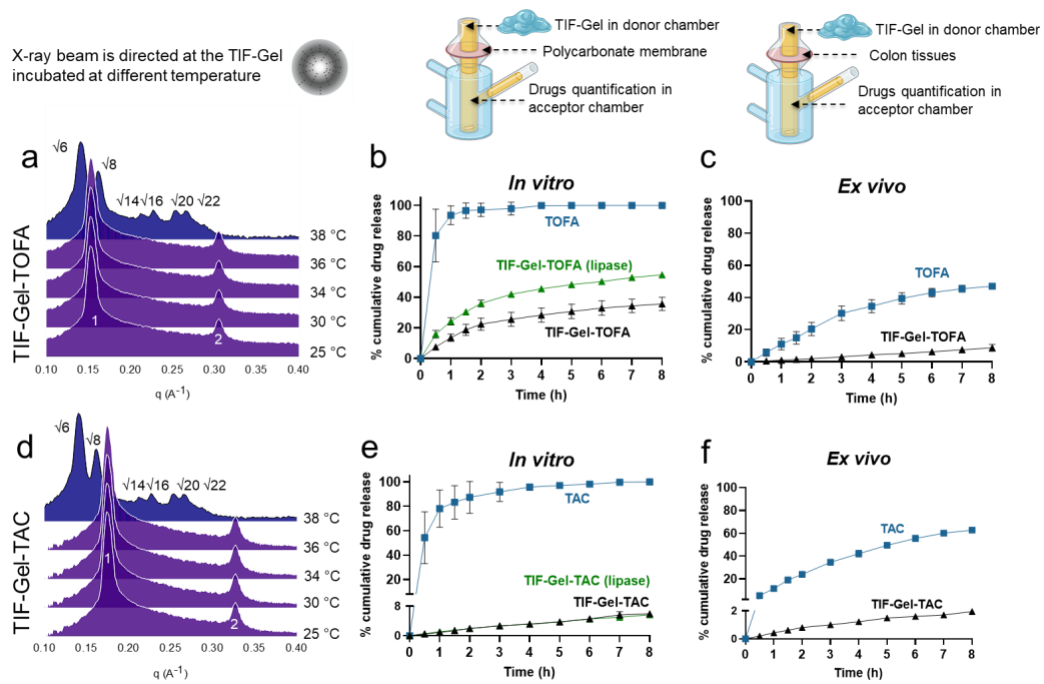


**Figure 2:** *In vitro* and *ex vivo* characterizations of the drug loaded TIF-Gel: (a) TOFA-loaded gel (TIF-Gel-TOFA) SAXS spectra acquired at different temperatures; (b) *in vitro* release of free drug (TOFA, blue line) and TIF-Gel-TOFA in HEPES buffer (black line) and in the presence of lipase (green line); (c) *ex vivo* release of free drug (TOFA, blue line) and TIF-Gel-TOFA (black line); (d) TAC loaded LMPS (TIF-Gel-TAC) SAXS spectra acquired at different temperatures; (e) *in vitro* release of free drug (TAC, blue line), TIF-Gel-TAC (black line) and in the presence of lipase (green line); (f) *ex vivo* release of free drug (TAC, blue line) and TIF-Gel-TAC in HEPES buffer (black line). Results in panels b, c, e and f are reported as mean  $\pm$  STDV (n=3).

### *Effect of TIF-Gel-TOFA on dextran sulfate sodium (DSS)-induced acute colitis*

To test the potential efficacy of the gel in treating an acute UC flare-up, we applied TIF-Gel loaded with TOFA to a mouse model of acute colitis induced by dextran sulfate sodium (DSS). DSS is toxic to epithelial cells and its application compromises the integrity of the intestinal barrier, thereby leading to an erosion of the epithelium and activation of submucosal immune cells by intestinal microbes<sup>70</sup>. Through experimentation, we determined that application of the gel every other day yielded robust mitigation of local and systemic inflammation.

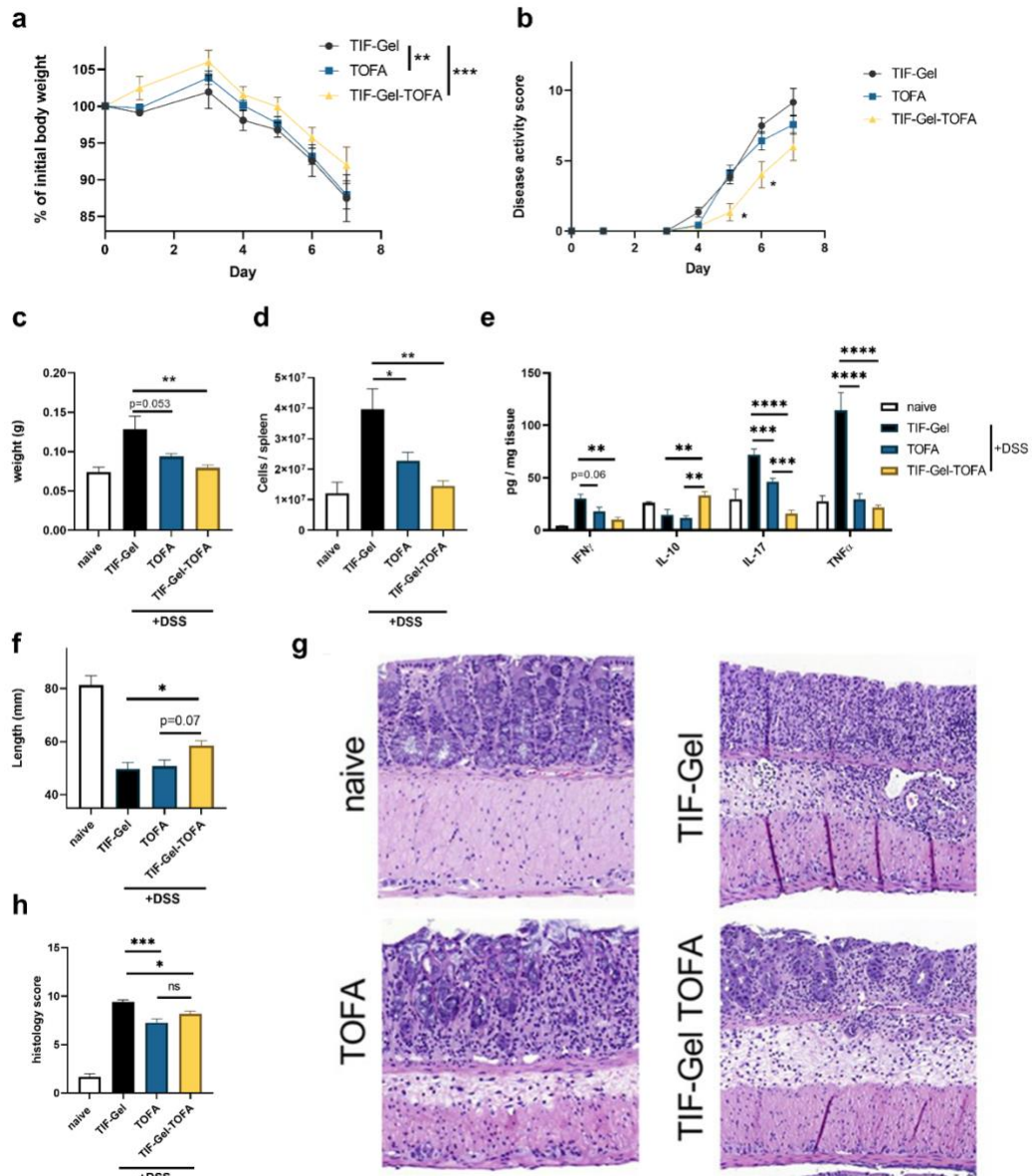


**Figure 3:** TIF-Gel-TOFA effectively mitigates intestinal inflammation and disease induced by DSS treatment in mice. Mice were prophylactically treated rectally with either empty gel (TIF-Gel), tofacitinib in vehicle (TOFA), or TOFA loaded-gel (TIF-Gel-TOFA) and thereafter challenged with 2% DSS in the drinking water. Treatments were then applied every other day until the end of the experiment. Weights (a) and disease score (b) were recorded throughout the experiment. At the end of the experiment, spleens, mesenteric lymph nodes (mLNs) and colons were removed from the mice. The spleens were weighed (c) and single splenocytes were enumerated (d). The tissue concentrations of various cytokines were measured (e). The mouse colon length was measured (f), and the colon was opened transversally, cleaned, and prepared for histology (g). Colon histopathology scores were determined by a blinded pathologist and aggregated (H). \*:  $p < 0.05$ , \*\*:  $p < 0.01$ , \*\*\*:  $p < 0.001$ , \*\*\*\*:  $p < 0.0001$ , and actual value is provided for values less than 0.1 but not meeting significance threshold as determined by 2-way ANOVA (a), multiple Student's- tests with Holm-Sidak correction for multiple comparisons (b), and one way ANOVA with multiple comparisons and Tukey correction (c, d, e, f, h). All tests were performed using Prism (GraphPad) and applying default settings for the above-mentioned analyses; naïve values were excluded from analyses; all error bars are  $\pm$ SEM.

Mice treated with this regimen of TIF-Gel-TOFA displayed decreased weight loss and disease severity when compared to mice treated with an empty TIF-Gel (**Figure 3a and 3b**). In contrast, drug in vehicle solution (TOFA), while improving weight loss, did not improve the disease score in these mice (**Figure 3b**). Of note, daily application of the compounds did not yield as robust results, and the differences between free TOFA and TIF-Gel-TOFA were less apparent under this regimen (in the Appendix, **A1.12**). Signs of systemic inflammation, determined by spleen size and cellularity, were also alleviated in mice treated every other day with the TIF-Gel-TOFA (**Figure 3c and 3d**). Furthermore, local pro-inflammatory cytokine levels were reduced in TOFA and TIF-Gel-TOFA-treated mice, and anti-inflammatory IL-10 levels were increased only in the TIF-Gel-TOFA group (**Figure 3e**). Local inflammation was also mitigated by the TIF-Gel-TOFA as determined by a reduction in colon shortening and pathology (**Figure 3f, 3g, and 3h**). For colon shortening, but not for histopathology, TIF-Gel-TOFA was more effective than the drug in vehicle, and no differences were detectable in the proportion of immune cell populations of the spleens or mesenteric lymph nodes of the different treatment groups (Fig. S7). Overall, these data indicate that a topically applied temperature-dependent *in situ*-forming gel carrying TOFA represents a valuable tool to mitigate acute intestinal inflammation.

#### *Effect of TIF-Gel-TAC on T-cell transfer colitis*

TIF-Gel acts as a platform able to host and release molecules with different polarities (**Figure 2**). Thus, we also assessed the ability of the TIF-Gel loaded with the hydrophobic drug TAC to reduce colitis severity using a model of T cell-mediated colitis, namely the T cell transfer colitis model <sup>71</sup>. In this model, naïve CD4 + T cells are transferred into B and T cell-deficient *Rag*<sup>-/-</sup> recipient mice, which results in the development of T helper cells that react against luminal antigens and subsequently induce a strong colon inflammation <sup>49,72,73</sup>. Three days after naïve T cell transfer into *Rag*<sup>-/-</sup> hosts, mice were treated with 100 µL i) TAC-loaded TIF-Gel (TIF-Gel-TAC), ii) empty TIF-Gel (TIF-Gel) or iii) TAC in vehicle solution (TAC) via daily rectal instillation (**Figure 4a**). Weight development and monitoring of disease activity demonstrated that mice that received empty TIF-Gel or TAC in vehicle solution started to develop the first signs of colitis around day 10 post T cell transfer as evidenced by progressive weight loss and signs of diarrhoea (**Figure 4b and 4c**). Of note, mice that were treated with TIF-Gel-TAC did not lose weight and diarrhoea scores were lower than in the other two groups (**Figure 4b and 4c**). Moreover, all mice receiving TAC (either in TIF-Gels or administered in vehicle) showed longer colons and reduced spleen weight (**Figure 4d**), indicating reduced disease in these two groups when compared to mice treated with empty TIF-Gels.



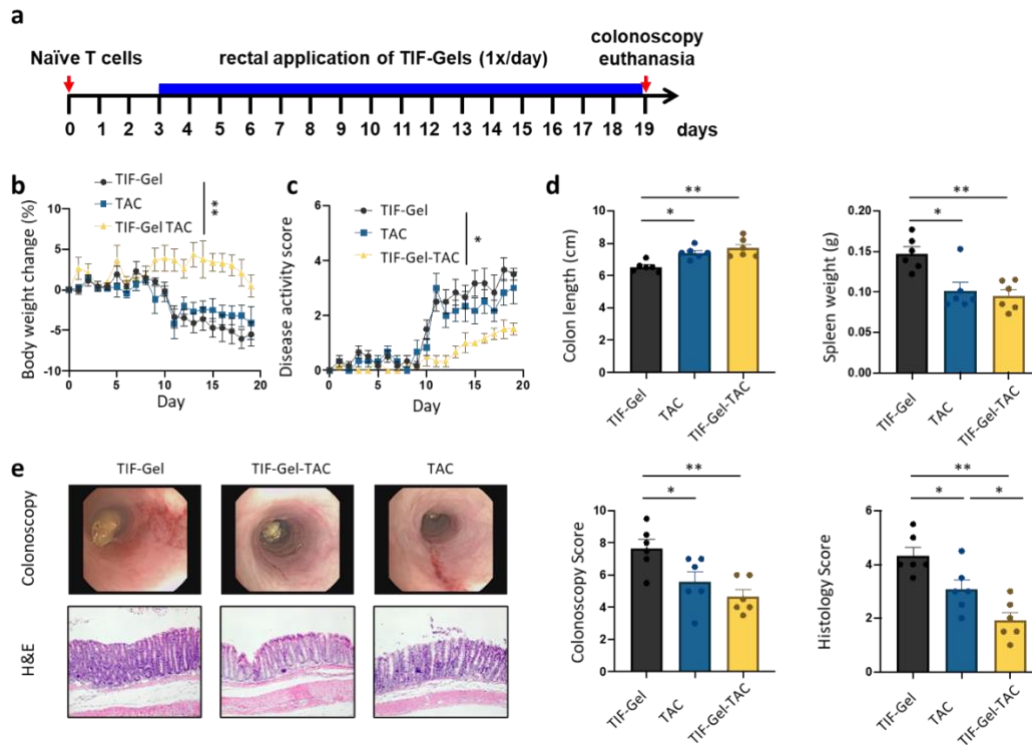


**Figure 4:** Assessment of the effect of TAC-loaded TIF-Gel on T cell-mediated colitis. 12–15-week-old *Rag<sup>-/-</sup>* mice develop colitis via transfer of  $2.5 \times 10^5$  naïve CD4<sup>+</sup> T cells. Starting on day 3 after T cell transfer, mice received daily rectal instillations with TIF-Gel without drug (TIF-Gel), TAC-loaded TIF-Gels (TIF-Gel-TAC) or TAC in vehicle (TAC). (a) Schematic overview on the experimental set-up; (b) weight development over the course of the experiment; (c) cumulative disease activity score; (d) colon length and spleen weight; (e) representative pictures and respective scoring from mouse colonoscopy on day 19 post T cell transfer and from H&E-stained sections of the terminal colon collected on day 19 post T cell transfer. \* $p < 0.05$ , \*\* $p < 0.01$  as determined by 2-way ANOVA (b+c) and one way ANOVA with multiple comparisons and Tukey correction (d+e). All tests were performed using Prism (GraphPad) and applying default settings for the above-mentioned analyses; all error bars are  $\pm$ SEM.

On day 19 after T cell transfer, all mice were subjected to colonoscopy to evaluate macroscopic signs of colitis. Interestingly, TAC-administration via TIF-Gels as well as TAC administration in vehicle reduced endoscopic signs of colitis. Although there was a clear trend towards further reduction of endoscopic scores in mice that received TIF-Gel-TAC, this was not significant (**Figure 4e**). In contrast, and in line with disease activity scores, mice that received TIF-Gel-TAC did not only show clearly reduced colitis severity when compared to mice that were treated with empty TIF-Gels, but also when compared to mice that received TAC in vehicle solution (see histology score; **Figure 4e**). Taken together, these data clearly indicate that TAC administration via TIF-Gels is superior in reducing colitis severity than TAC-administration in vehicle. T cell transfer colitis is mainly mediated by aberrantly activated T helper cells, and especially IFN- $\gamma$ <sup>+</sup> (Th1) and IL-17<sup>+</sup> (Th17) CD4<sup>+</sup> T cells

contribute to the disease. To test the effect of TAC administration either in vehicle or in the TIF-Gels, we analysed proportions of T helper cells in the colonic lamina propria (**Figure 5a**), mesenteric lymph nodes (**Figure 5b**) and the spleen (**Figure 5c**). Of note, both TAC administration forms reduced the relative abundance of T cells in the *lamina propria*, mesenteric lymph nodes and the spleen (**Figure 5a and c**). Among those, Th1 and Th17 cells were reduced with TAC in vehicle as well as with TIF-Gel-TAC when compared to the mice that received empty TIF-Gels only (**Figure 5**). While there was no difference among Th1 cells between mice receiving of TAC in vehicle and those receiving TIF-Gel-TAC, the reduction in Th17 cells was significantly more pronounced in mice receiving TIF-Gel-TAC than in those receiving TAC in vehicle (**Figure 5**). In general, there was not much effect on the abundance of FoxP3+ (regulatory) T cells (**Figure 5**). These findings were also reflected in cytokine measurements in colonic tissues (**Figure 5d**), where we found reduced levels of IFN- $\gamma$  and IL-17 in mice treated with the free drug. TIF-Gel-TAC further reduced levels of these two cytokines and in addition also significantly reduced levels of TNF- $\alpha$  (**Figure 5d**), indicating that TIF-Gel-TAC has a stronger effect on the production of inflammatory cytokines when compared to the free drug. In summary, these results indicate that administration of TIF-Gel-TAC is superior in reducing disease-promoting T helper cells in the setting of T cell induced colitis.

This further confirms the results in the DSS model and supports the observation that the TIF-Gel represents a valid option to locally deliver drugs to the inflamed mucosa.

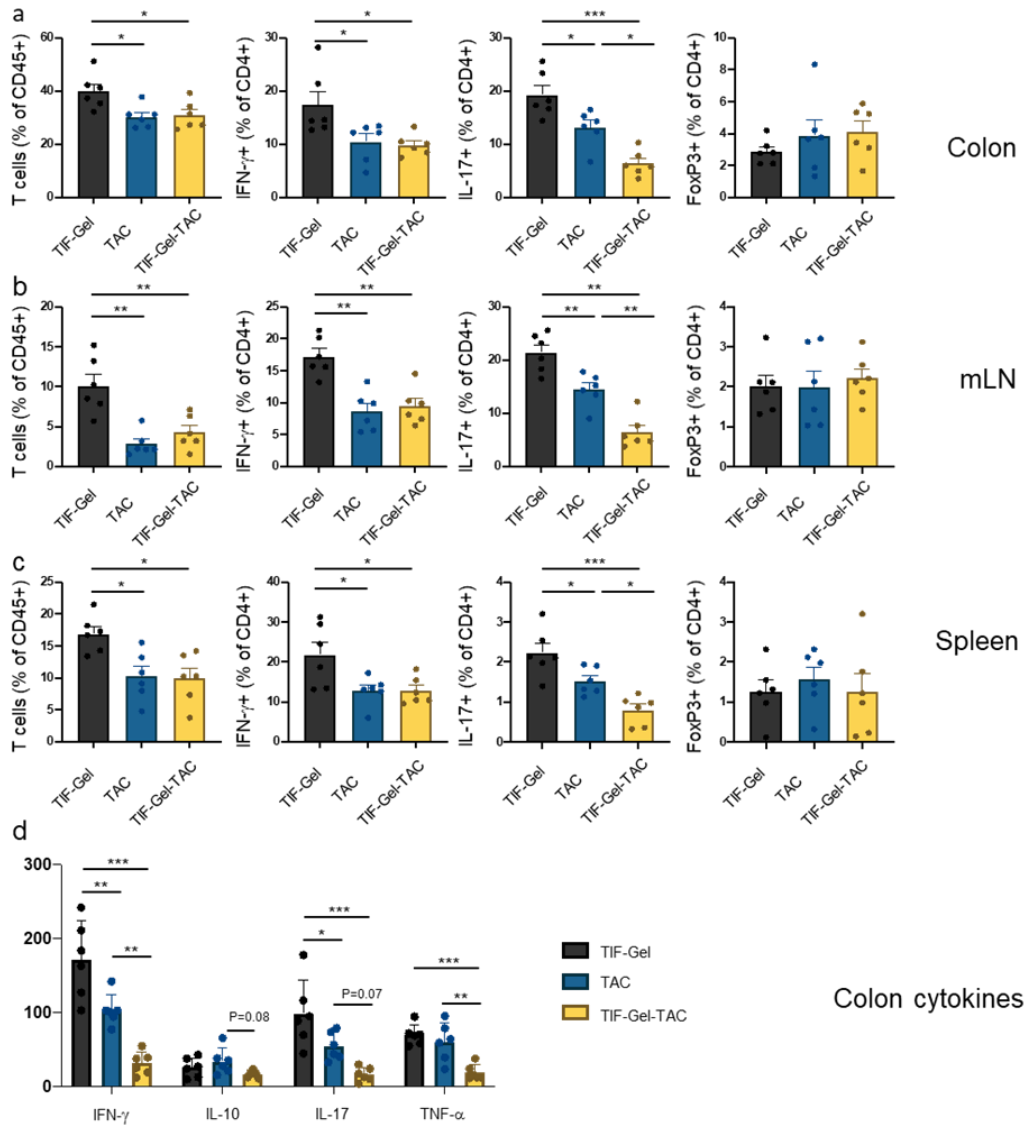


**Figure 5:** Immune cell populations and cytokine levels in the colon from TAC-loaded TIF-Gel (TIF-Gel-TAC) treated mice. 12–15-week-old *Rag*<sup>-/-</sup> mice develop colitis via transfer of  $2.5 \times 10^5$  naïve T cells. Starting on day 3 post T cell transfer, mice received daily rectal instillations with TIF-Gel without drug (TIF-Gel), TAC-loaded TIF-Gels (TIF-Gel-TAC) or TAC in vehicle (TAC). Depicted are the relative abundance of the indicated cell populations in (a) the colonic *lamina propria*, (b) mesenteric lymph nodes; and (c) the spleen on day 19 after T cell transfer, and (d) levels of indicated cytokines in colon lysates. \* $p < 0.05$ , \*\* $p < 0.01$ , \*\*\* $p < 0.001$  as determined by one way ANOVA with multiple comparisons and Tukey correction. All tests were performed using Prism (GraphPad) and applying default settings for the above-mentioned analyses; all error bars are  $\pm$ SEM.

### *Rectal drug delivery via TIF-Gel reduces systemic drug exposure*

To demonstrate that rectal TIF-Gel application was indeed suitable to minimizing systemic exposure, we analyzed drug release *in vivo* by longitudinally monitoring in mice drug plasma levels after TIF-Gel application into the colon. For this purpose, naïve received a single enema of either drug-loaded

TIF-Gel (TIF-Gel-TOFA or TIF-Gel-TAC) or of free drugs (TOFA or TAC) and plasma drug concentrations were measured at different time points (**Figure 6a**). Mice receiving free TOFA had an early peak in plasma concentration at 0.25 h (**Figure 6b**); TOFA plasma levels rapidly decreased thereafter, following first-order kinetics. In mice receiving TIF-Gel-TOFA, the peak concentration at 0.25 h was significantly lower. The area under the curve (AUC), a measurement of cumulative systemic drug absorption, was also significantly reduced in the mice treated with TIF-Gel-TOFA when compared to the group treated with free TOFA (**Figure 6d**). Administration of TAC, either as free drug, or as drug loaded gel resulted in a low (and negligible) systemic drug circulation (**Figure 6c**) and no difference was detected in their AUCs (**Figure 6e**).

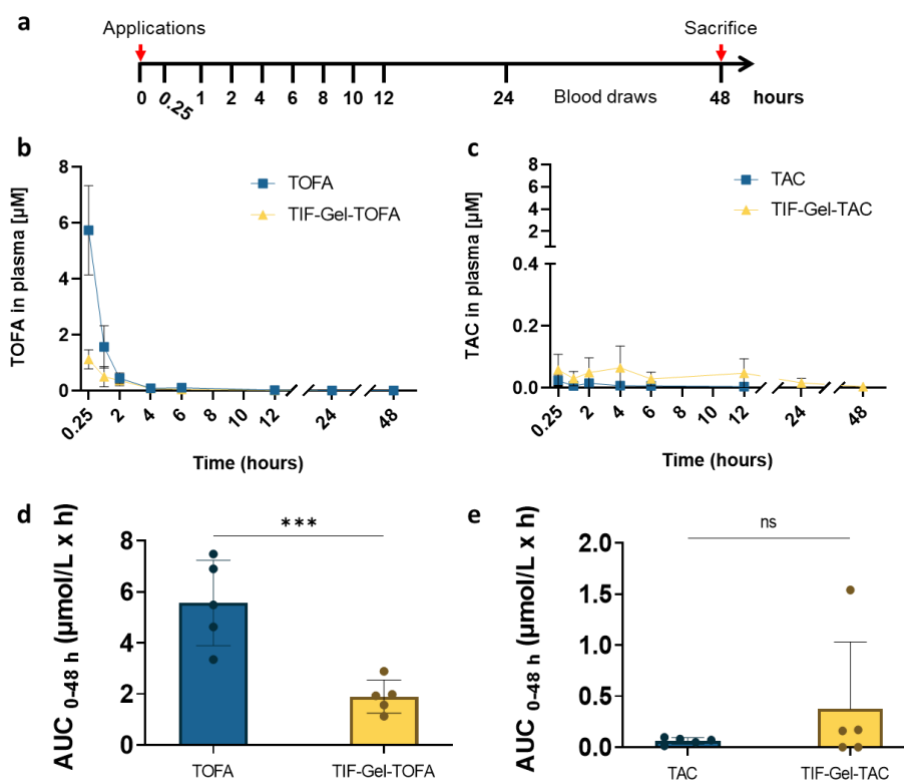


**Figure 6:** Drug delivery via TIF-Gel leads to a low systemic drug exposure. (a) Experimental design for the pharmacokinetic study. Naïve mice (n=5/group) received a single enema of either drug-loaded TIF-Gel (TIF-Gel-TOFA or TIF-Gel-TAC) or free drugs (TOFA or TAC). The plasma drug concentrations were measured at the indicated time points after administration. Plasma concentration versus time profiles of the pharmacokinetic experiment of TOFA- (b) and TAC-treated animals (c) and Area Under the Curve (AUC)<sub>0-48h</sub> values of TOFA- and TAC-treated mice (d and e, respectively). \*\*\*p<0.001, as determined by Student's t test.

Although the drug concentrations in the TIF-Gel can reach high levels, this delivery platform also helps to simultaneously minimize systemic circulation. The plasma concentration of the TOFA in

TIF-Gel-treated mice was lower than in animals rectally treated with free drug within a 48h period after application. On the other end, the pharmacokinetics of TAC either as free drug or as drug loaded gel results in a negligible systemic drug absorption and no difference was detected in their AUCs. In a previous reported clinical study, rectal administration of TAC via a suppository resulted in a systemic exposure with a relative bioavailability of ~70% after 24 h in comparison to the oral formulation<sup>74</sup>. Here, upon administration, patients were asked to remain in a semi-recumbent position for 3 h (without defecation), practice which facilitates drug absorption. Differently from this study, after administration our mice were left free to move and this introduced a certain external variability in the excretion time of the stools and/or of the drug. The low residence time into the intestine could explain the low plasmatic levels of free TAC observed, whereas the low drug absorption of TAC released from TIF-Gel loaded could be explained by a slow and continuous drug release from the gel. In conclusion, this reduced systemic drug concentration indicates that the use of TIF-Gel could reduce the number and severity of systemic side effects resulting from the use of potent drugs such as TOFA and TAC in a clinical setting.

#### 4. Conclusions

Our formulation has the potential to reduce drug side effects associated with systemic therapy, as well as the drawbacks associated with commercially available rectal formulations. This could be particularly important for patients who experience fecal urgency as a result of high-volume daily enema applications. Our research demonstrates that TIF-Gel can effectively administer anti-inflammatory drugs TOFA and TAC locally to the colonic mucosa, resulting in sustained drug release. This approach enhances the localized activity of these drugs, potentially reducing the risk of side effects. We anticipate that TIF-Gel will offer a more patient-friendly drug delivery platform with reduced leakage, retention, bloating, and urgency. This, in turn, could lead to greater patient compliance with drug regimens and an expanded range of topical therapies.

## 5. References

1. Meier, J. Epidemiology. Inflammatory Bowel Disease Nursing Manual. *Springer International Publishing*, 11-14 (2019).
2. Ungaro, R., Mehandru, S., Allen, P. B., Peyrin-Biroulet, L., Colombel, J. F. Ulcerative colitis. *The Lancet* **389**(10080), 1756–1770 (2017).
3. Singh, S., Allegrretti, J. R., Siddique, S. M. & Terdiman, J. P. AGA Technical Review on the Management of Moderate to Severe Ulcerative Colitis. *Gastroenterology* **158**(5), 1465-1496 (2020).
4. Ko, C. W., Singh S., Feuerstein J. D., Falck-Ytter C., Falck-Ytter Y., Cross R. K. AGA Clinical Practice Guidelines on the Management of Mild-to-Moderate Ulcerative Colitis. *Gastroenterology* **156**(3), 748-764 (2019).
5. Manz, M., Michetti, P., Seibold, F., Rogler, G., Beglinger, C. Treatment algorithm for moderate to severe ulcerative colitis. *Swiss Med Wkly* **141**, 13235 (2011).
6. Wehkamp, J., Stange, E. F. Recent advances and emerging therapies in the non-surgical management of ulcerative colitis. *F1000Res* **7**, 1207 (2018).
7. Khanna, R., Afif, W. Ustekinumab for Ulcerative Colitis. *Gastroenterology* **160**, 2184–2186 (2021).
8. Sandborn, W. J., Feagan, B. G., Wolf, D. C., D'Haens, G., Vermeire, S., Hanauer, S. B., Ghosh, S., Smith, H., Cravets, M., Frohna, P. A., Aranda, R., Gujrathi, S., Olson, A. Ozanimod Induction and Maintenance Treatment for Ulcerative Colitis. *N Engl J Med* **374**(18), 1754-1762 (2016).
9. D'Haens, G. Risks and benefits of biologic therapy for inflammatory bowel diseases. *Gut* **56**, 725–732 (2007).
10. Ben-Horin, S., Mao, R., Chen, M. Optimizing biologic treatment in IBD: objective measures, but when, how and how often? *BMC Gastroenterol* **15**, 178 (2015).
11. Kirchgessner, J., Kirchgessner, J., Lemaitre, M., Carrat, F., Zureik, M., Carbonnel, F., Dray-Spira, R. Risk of Serious and Opportunistic Infections Associated with Treatment of Inflammatory Bowel Diseases. *Gastroenterology* **155**(2), 337-346 (2018).
12. Mocci, G., Marzo, M., Papa, A., Armuzzi, A., Guidi, L. Dermatological adverse reactions during anti-TNF treatments: Focus on inflammatory bowel disease. *JCC* **7**, 769–779 (2013).
13. Hoentjen, F., van Bodegraven, A. A. Safety of anti-tumor necrosis factor therapy in inflammatory bowel disease. *World J Gastroenterol* **15**, 2067–2073 (2009).
14. Danese, S., Grisham, M., Hodge, J., Telliez, J.-B. JAK inhibition using tofacitinib for inflammatory bowel disease treatment: a hub for multiple inflammatory cytokines. *Am J Physiol* **310**, 155–162 (2016).
15. Bonovas, S., Lytras, T., Nikolopoulos, G., Peyrin-Biroulet, L., Danese, S. Systematic review with network meta-analysis: comparative assessment of tofacitinib and biological therapies for moderate-to-severe ulcerative colitis. *Aliment Pharmacol Ther* **47**(4), 454-465 (2018).
16. Singh, S., Fumery, M., Sandborn, W. J., Murad, M. H. Systematic review with network meta-analysis: first- and second-line pharmacotherapy for moderate-severe ulcerative colitis. *Aliment Pharmacol Ther* **47**(2), 162-175 (2018).
17. Ogata, H., Matsui, T., Nakamura, M., Iida, M., Takazoe, M., Suzuki, Y., Hibi, T. A randomised dose finding study of oral tacrolimus (FK506) therapy in refractory ulcerative colitis. *Gut* **55**, 1255–1262 (2006).
18. Rogler, G. Gastrointestinal and liver adverse effects of drugs used for treating IBD. *Best Pract Res Clin Gastroenterol* **24**(2), 157-165 (2010).
19. Westhovens, R. Clinical efficacy of new JAK inhibitors under development. Just more of the same? *Rheumatology* **58**, 27–33 (2019).
20. Haga, K., Shibuya, T., Nomura, K., Okahara, K., Nomura, O., Ishikawa, D., Sakamoto, N., Osada, T., Nagahara, A. Effectiveness and Nephrotoxicity of Long-Term Tacrolimus Administration in Patients with Ulcerative Colitis. *J Clin Med* **9**(6), 1771 (2020).
21. Godat, S., Fournier, N., Safroneeva, E., Juillerat, P., Nydegger, A., Straumann, A., Vavricka, S., Biedermann, L., Greuter, T., Fraga, M., Abdelrahman, K., Hahnloser, D., Sauter, B., Rogler, G., Michetti, P., Schoepfer, A. M. Frequency and type of drug-related side effects necessitating treatment discontinuation in the Swiss Inflammatory Bowel Disease Cohort. *Eur J Gastroenterol Hepatol* **30**(6), 612–620 (2018).
22. Frei, P., Biedermann, L., Manser, C. N., Wilk, M., Manz, M., Vavricka, S. R., Rogler, G. Topical therapies in inflammatory bowel disease. *Digestion* **86**, 36–44 (2012).
23. Cohen, R. D., Weissshof, R. A comprehensive review of topical therapies for distal ulcerative colitis. *Gastroenterol Hepatol (N Y)* **16**, 21–27 (2020).
24. Marshall, J. K., Irvine, E. J. Rectal aminosalicylate therapy for distal ulcerative colitis: a meta-analysis. *Aliment Pharmacol Ther* **9**(3), 293–300 (1995).
25. Katz, S., Lichtenstein, G. R., Safdi, M. A. 5-ASA dose-response: Maximizing efficacy and adherence. *Gastroenterol Hepatol* **6**, 1–12 (2010).
26. Safdi, M., DeMicco, M., Sninsky, C., Banks, P., Wruble, L., Deren, J., Koval, G., Nichols, T., Targan, S., Fleishman, C., Wiita, B. A Double-Blind Comparison of Oral versus Rectal Mesalamine versus Combination Therapy in the Treatment of Distal Ulcerative Colitis. *Am J Gastroenterol* **92**(10), 1867-1871 (1997).
27. Lawrance, I. C., Copeland, T. S. Rectal tacrolimus in the treatment of resistant ulcerative proctitis. *Aliment Pharmacol Ther* **28**, 1214–1220 (2008).
28. van Dieren, J. M., van Bodegraven, A. A., Kuipers, E. J., Bakker, E. N., Poen, A. C., van Dekken, H., Nieuwenhuis, E. E., van der Woude, C. J. Local application of tacrolimus in distal colitis: Feasible and safe. *Inflamm Bowel Dis* **15**(2), 193–198 (2009).
29. Lawrance, I. C., Baird, A., Lightower, D., Radford-Smith, G., Andrews, J. M., Connor, S. Efficacy of Rectal Tacrolimus for Induction Therapy in Patients With Resistant Ulcerative Proctitis. *Clin Gastroenterol Hepatol* **15**(8), 1248–1255 (2017).
30. Fehily, S. R., Martin, F. C., Kamm, M. A. Simple water-based tacrolimus enemas for refractory proctitis. *JGH Open* **4**, 561–564 (2020).
31. Lawrance, I. C., Baird, A., Lightower, D., Radford-Smith, G., Andrews, J. M., Connor, S. Efficacy of rectal tacrolimus for induction therapy in patients with resistant ulcerative proctitis. *Clin Gastroenterol Hepatol* **15**(8), 1248-1255 (2017).
32. Seoane-Viaño, I., Ong, J. J., Luzardo-Álvarez, A., González-Barcia, M., Basit, A. W., Otero-Espinar, F. J., Goyanes, A. 3D printed tacrolimus suppositories for the treatment of ulcerative colitis. *Asian J Pharm Sci* **16**, 110–119 (2021).
33. Frei, P., Rogler, G. Topical therapies for inflammatory bowel disease. *Digestion* **86**, 36-44 (2017).
34. Gionchetti, P., Rizzello, F., Venturi, A., Brignola, C., Ferretti, M., Peruzzo, S., Campieri, M. Comparison of mesalazine suppositories in proctitis and distal proctosigmoiditis. *Aliment Pharmacol Ther* **11**, 1053–1057 (1997).

35. Campieri, M., Gionchetti, P., Belluzzi, A., Brignola, C., Tabanelli, G.M., Miglioli, M., Barbara, L. 5-Aminosalicylic acid as enemas or suppositories in distal ulcerative colitis? *J Clin Gastroenterol* **10**, 406–409 (1988).
36. Seibold, F., Fournier, N., Beglinger, C., Mottet, C., Pittet, V., Rogler, G. Topical therapy is underused in patients with ulcerative colitis. *J Crohns Colitis* **8**, 56–63 (2014).
37. Nidhi, Rashid, M., Kaur, V., Hallan, S.S., Sharma, S., Mishra, N. Microparticles as controlled drug delivery carrier for the treatment of ulcerative colitis: A brief review. *SPJ* **24**, 458–472 (2016).
38. Aleandri, S., Mezzenga, R. The physics of lipidic mesophase delivery systems. *Phys Today* **73**, 38–44 (2020).
39. Mezzenga, R., Meyer, C., Servais, C., Romoscanu, A.I., Sagalowicz, L., Hayward, R.C. Shear rheology of lyotropic liquid crystals: a case study. *Langmuir* **21**, 3322–3333 (2005).
40. Fong, W. K., Hanley, T., Boyd, B. J. Stimuli responsive liquid crystals provide ‘on-demand’ drug delivery in vitro and in vivo. *J Control Release* **135**, 218–226 (2009).
41. Tardieu, A., Luzzati, V. Polymorphism of lipids a novel cubic phase - a cage-like network of rods with enclosed spherical micelles. *Biochim Biophys Acta* **219**, 11–17 (1970).
42. Camilleri, M., Linden, D. R. Measurement of Gastrointestinal and Colonic Motor Functions in Humans and Animals. *CMGH* **2**, 412–428 (2016).
43. Wirtz, S., Neurath, M. F. Mouse models of inflammatory bowel disease. *Advanced Drug Delivery Reviews* **59**, 1073–1083 (2007).
44. Eri, R., McGuckin, M. A., Wadley, R. T cell transfer model of colitis: A great tool to assess the contribution of T cells in chronic intestinal inflammation. *Methods in Molecular Biology* **844**, 261–275 (2012).
45. Mager, L. F., Koelzer, V.H., Stuber, R., Thoo, L., Keller, I., Koeck, I., Langenegger, M., Simillion, C., Pfister, S.P., Faderl, M., Genitsch, V., Tymbarevich, I., Juillerat, P., Li, X., Xia, Y., Karamitopoulou, E., Lyck, R., Zlobec, I., Hafelmeier, S., Bruggmann, R., McCoy, K.D., Macpherson, A.J., Müller, C., Beutler, B., Krebs, P. The ESRP1-GPR137 axis contributes to intestinal pathogenesis. *Elife* **6**, 28366 (2017).
46. Moolenbeek, C., Ruitenbergh, E. J. The ‘Swiss roll’: A simple technique for histological studies of the rodent intestine. *Lab Anim* **15**, 57–59 (1981).
47. Erben, U., Loddenkemper, C., Doerfel, K., Spieckermann, S., Haller, D., Heimesaat, M.M., Zeitz, M., Siegmund, B., Kühn, A.A. A guide to histomorphological evaluation of intestinal inflammation in mouse models. *Int J Clin Exp Pathol* **7**, 4557–4576 (2014).
48. Liyanage, S. E. Flow cytometric analysis of inflammatory and resident myeloid populations in mouse ocular inflammatory models. *Experimental Eye Research* **151**, 160–170 (2016).
49. Spalinger, M. R., Schmidt, T.S., Schwarzfischer, M., Hering, L., Atrott, K., Lang, S., Gottier, C., Geirnaert, A., Lacroix, C., Dai, X., Rawlings, D.J., Chan, A.C., von Mering, C., Rogler, G., Scharl, M. Protein tyrosine phosphatase non-receptor type 22 modulates colitis in a microbiota-dependent manner. *Journal of Clinical Investigation* **129**, 2527–2541 (2019).
50. Spalinger, M. R., Schwarzfischer, M., Hering, L., Shawki, A., Sayoc, A., Santos, A., Gottier, C., Lang, S., Bäbler, K., Geirnaert, A., Lacroix, C., Leventhal, G.E., Dai, X., Rawlings, D., Chan, A.A., Rogler, G., McCole, D.F., Scharl, M. Loss of PTPN22 abrogates the beneficial effect of cohousing-mediated fecal microbiota transfer in murine colitis. *Mucosal Immunol* **12**, 1336–1347 (2019).
51. Raine, T. ECCO Guidelines on Therapeutics in Ulcerative Colitis: Medical Treatment. *J Crohns Colitis* **16**, 2–17 (2022).
52. Sagalowicz, L., Leser, M. E., Watzke, H. J., Michel, M. Monoglyceride self-assembly structures as delivery vehicles. *Trends in Food Science and Technology* **17(5)**, 204–214 (2006).
53. Demurtas, D., Guichard, P., Martiel, I., Mezzenga, R. Direct visualization of dispersed lipid bicontinuous cubic phases by cryo-electron tomography. *Nat Commun* **6**, (2015).
54. Mezzenga, R., Meyer, C., Servais, C., Romoscanu, A.I., Sagalowicz, L., Hayward, R.C. Shear rheology of lyotropic liquid crystals: a case study. *Langmuir* **21**, 3322–3333 (2005).
55. Tiberg, F., Harwigsson, I., Johnsson, M. High bioavailability opioid formulations. *US Patent App* **13(558)**, 463 (2013).
56. Examiner, P. & Bali, V. United States Patent (10) Patent No 2, 1–6 (2006).
57. Otten, M. H., Haas, G. de, Ende, R. van den. Colonic range of 5-ASA enemas in healthy individuals, with a comparison of their physical and chemical characteristics. An open, single-dose, randomized, cross-over study. *Aliment Pharmacol Ther* **11**, 693–697 (1997).
58. Ingram, J. R. Comparative study of enema retention and preference in ulcerative colitis. *Postgrad Med J* **81**, 594–598 (2005).
59. Rahanyan-Kagi, N., Aleandri, S., Speziale, C., Mezzenga, R., Landau, E. M. Stimuli-responsive lipidic cubic phase: triggered release and sequestration of guest molecules. *Chemistry (Easton)* **21**, 1873–1877 (2015).
60. Liu, Q., Xiao, Y., Hawley, A., Boyd, B. J. Lipid-based lyotropic liquid crystalline phase transitions as a novel assay platform using birefringence as the visual signal output. *J Mater Chem B* **8**, 6277–6285 (2020).
61. Zhang, S., Ermann, J., Succi, M.D., Zhou, A., Hamilton, M.J., Cao, B., Korzenik, J.R., Glickman, J.N., Vemula, P.K., Glimcher, L.H., Traverso, G., Langer, R., Karp, J.M. An inflammation-targeting hydrogel for local drug delivery in inflammatory bowel disease. *Sci Transl Med* **7**, 300 (2015).
62. Rocha, R. A., Vélez, D., Devesa, V. In vitro evaluation of intestinal fluoride absorption using different cell models. *Toxicol Lett* **210(7)**, 311–317 (2012).
63. Nollevaux, G., Devillé, C., El Moulaj, B., Zorzi, W., Deloyer, P., Schneider, Y.J., Peulen, O., Dandriofosse, G. Development of a serum-free co-culture of human intestinal epithelium cell-lines (Caco-2/HT29-5M21). *BMC Cell Biol* **7**, 20 (2006).
64. Walter, E., Janich, S., Roessler, B. J., Hilfinger, J. M., Amidon, G. L. HT29-MTX/Caco-2 Cocultures as an in Vitro Model for the Intestinal Epithelium: In Vitro-in Vivo Correlation with Permeability Data from Rats and Humans. *J Pharm Sci* **85**, 1070–1076 (1996).
65. Low, D., Nguyen, D. D., Mizoguchi, E. Animal models of ulcerative colitis and their application in drug research. *Drug Des Devel Ther* **7**, 1341–357 (2013).
66. Low, D., Nguyen, D. D., Mizoguchi, E. Animal models of ulcerative colitis and their application in drug research. *Drug Design, Development and Therapy* **7**, 1341–1356 (2013).
67. Ivanova, N. A., Trapani, A., Franco, C.D., Mandracchia, D., Trapani, G., Franchini, C., Corbo, F., Tripodo, G., Kolev, I.N., Stoyanov, G.S., Bratsova, K.Z. In vitro and ex vivo studies on diltiazem hydrochloride-loaded microsponges in rectal gels for chronic anal fissures treatment. *Int J Pharm* **557**, 53–65 (2019).
68. Zhang, S., Ermann, J., Succi, M.D., Zhou, A., Hamilton, M.J., Cao, B., Korzenik, J.R., Glickman, J.N., Vemula, P.K., Glimcher, L.H., Traverso, G., Langer, R., Karp, J.M. An inflammation-targeting hydrogel for local drug delivery in inflammatory bowel disease. *Sci Transl Med* **7**, 1–11 (2015).
69. Martiel, I., Baumann, N., Vallooran, J.J., Bergfreund, J., Sagalowicz, L., Mezzenga, R. Oil and drug control the

- release rate from lyotropic liquid crystals. *J Control Release* **204**, 78–84 (2015).
70. Wirtz, S., Popp, V., Indermann, M., Gerlach, K., Weigmann, B., Fichtner-Feigl, S., Neurath, M.F. Chemically induced mouse models of acute and chronic intestinal inflammation. *Nat Protoc* **12**, 1295–1309 (2017).
71. Ostanin, D. V., Bao, J., Koboziev, I., Gray, L., Robinson-Jackson, S.A., Kosloski-Davidson, M., Price, V.H., Grisham, M.B.T cell transfer model of chronic colitis: Concepts, considerations, and tricks of the trade. *Am J Physiol Gastrointest Liver Physiol* **296**, 135–146 (2009).
72. Spalinger, M. R., Kasper, S., Chassard, C., Raselli, T., Frey-Wagner, I., Gottier, C., Lang, S., Atrott, K., Vavricka, S.R., Mair, F., Becher, B., Lacroix, C., Fried, M., Rogler, G., Scharl, M. PTPN2 controls differentiation of CD4+ T cells and limits intestinal inflammation and intestinal dysbiosis. *Mucosal Immunol* **8**, 918–929 (2015).
73. Spalinger, M. R., Schwarzfischer, M., Niechcial, A., Atrott, K., Laimbacher, A., Gottier, C., Lang, S., Scharl, M. Loss of PTPN22 Promotes Intestinal Inflammation by Compromising Granulocyte-mediated Antibacterial Defence. *J Crohns Colitis* **15**, 2118–2130 (2021).
74. Stiff, F., Vanmolkot, F., Scheffers, I., van Bortel, L., Neef, C., Christiaans, M. Rectal and sublingual administration of tacrolimus: A single-dose pharmacokinetic study in healthy volunteers. *Br J Clin Pharmacol* **78**, 996–1004 (2014).



## Chapter 3

# Composite layer-by-layer liposomal gel for mucosal delivery of pirfenidone

Marianna Carone<sup>1</sup>, Sarah Teworte<sup>1</sup>, Simone Aleandri<sup>1</sup>, Gregor Bordon<sup>1</sup>, Paola Luciani<sup>1</sup>

### **Affiliations:**

<sup>1</sup> Department of Chemistry, Biochemistry and Pharmaceutical Sciences, University of Bern, Bern, Switzerland

Simone Aleandri and Paola Luciani contributed with the conceptualization and design of the layer-by-layer liposomal gel. Sarah Teworte performed the release studies for vaginal delivery. Gregor Bordon contributed with the development of the hydrogel.

This chapter is prepared for submission as ‘Composite layer-by-layer liposomal gel for mucosal delivery of pirfenidone’.

## 1. Introduction

There is an unmet medical need for the treatment of fibrosis. Fibrotic disorders can affect any organ and has been estimated to contribute to approximately 45% of all deaths in the Global North.<sup>1-3</sup> Currently, only two drugs –pirfenidone (PFD) and nintedanib – are approved in several countries for the treatment of idiopathic pulmonary fibrosis<sup>1,4</sup> and their investigational use across various organs showed promising results.<sup>5-13</sup> Indeed, fibrotic diseases share common mechanisms and core pathways that are of central pathophysiological relevance.<sup>14</sup> Therefore, drug repurposing may result in an effective approach to treat a wide range of fibrotic diseases.<sup>15</sup>

PFD (also known as Esbriet) is approved since 2011 by the European Medicines Agency<sup>16</sup> and 2014 by U.S Food & Drug administration<sup>17</sup> for the treatment of mild-to-moderate idiopathic pulmonary fibrosis. To date, only two immediate-release hard tablets (containing 801 mg and 267 mg of PFD) are commercially available. Beside its proven effectiveness, PFD is associated with a consistent adverse-event profile,<sup>18,19</sup> and a considerable number of patients required dose readjustments.<sup>20,21</sup> The main side effects include gastrointestinal and neurological complications together with photosensitivity reactions. For these reasons, local and sustained delivery of PFD has been increasingly evaluated as a therapeutic option for various fibrotic diseases. Indeed, this approach aims to reduce systemic exposure and collateral or end-organ adverse effects while maintaining therapeutic levels at the fibrotic site. At present, numerous preclinical and clinical efforts have resulted in promising advances in the treatment of local fibrosis-related diseases with PFD,<sup>11,22-24</sup> such as the treatment of fibrotic scar following spinal cord injury,<sup>25</sup> diabetic foot,<sup>26</sup> and localized scleroderma.<sup>27</sup> PFD therapy has also shown to be particularly effective at preventing and reducing post-operative fibrosis,<sup>28,29</sup> dramatically influencing surgery outcomes, as for glaucoma.<sup>30-32</sup> Maximizing local delivery to achieve high drug concentration at the fibrotic site holds promise as a valuable strategy for patients.

Despite efforts for inflammatory bowel disease (IBD) patients, treatment of inflammation and fibrosis in IBD still represents a challenge to most gastroenterologist.<sup>33</sup> Indeed, IBD-associated fibrosis is a common complication of the chronic or recurrent inflammation<sup>34</sup> and it is characterized by an excessive accumulation of extracellular matrix. At present, there are no specific treatment option, and approximately 80% of patients with intestinal strictures require surgery.<sup>35,36</sup> Notably, results from a previous preclinical study<sup>36</sup> confirmed the antifibrotic effect of PFD in both *in vitro* and *in vivo* model of intestinal fibrosis. However, considering the side effect profile of the oral administration - due to

the high dosage - we envision that the therapeutic value of PFD can be improved by exploiting the rectal route for a targeted delivery.

Besides involving the gastrointestinal tract, fibrotic diseases may affect the female reproductive system as leiomyomas (uterine fibroids),<sup>37</sup> endometrial fibrosis,<sup>38</sup> and endometriosis, which is characterized by the presence of fibrotic adhesions in the pelvic cavity.<sup>39,40</sup> In preclinical studies, PFD was shown to inhibit the proliferation of leiomyoma cells *in vitro*<sup>41</sup> and reduce fibrosis in a rat model of abdominal adhesions<sup>42</sup> providing hints that PFD may have potential as a nonhormonal therapy for fibrotic gynecological conditions. We expect that delivering PFD *via* the vaginal route will result in locally elevated concentrations of PFD around the uterus due to the first uterine pass effect.<sup>43,44</sup> To date, no formulation for the vaginal delivery of PFD exists.

To this aim, we designed a delivery system comprising layer-by-layer liposomes (LbL-LIPs) homogeneously incorporated into a zinc alginate hydrogel. Alginate hydrogel was chosen to ensure a prolonged contact time at the site of treatment - not achievable with an aqueous solution of liposomes alone - and for its negative charge that result potentially in improved inflammation-targeting property.<sup>45</sup> PFD was encapsulated in negatively charged liposomes using a layer-by-layer (LbL) design, enabling a tunable drug delivery system for this antifibrotic drug.

Our approach led to: (1) the development of highly concentrated PFD-loaded liposomes through one-step film hydration method, easy to manufacture and scale-up; (2) the formation of multiple-layered liposomes by LbL electrostatic deposition of biopolymers without purification steps; (3) the rapid fabrication of an alginate hydrogel cross-linked by zinc chloride with a potential inflammation-targeting property; (4) a LbL liposomal gel (LbL-LIP-Gel) releasing PFD in a sustained manner and; (5) a tunable PFD release ranging from hours to several days by tuning the layer thickness. Our composite LbL-LIP-Gel laden with PFD may offer unique opportunities for local and sustained delivery of a small and hydrophilic antifibrotic agent directly to the fibrotic site.

## 2. Materials and methods

### *Materials*

The phospholipids 1,2-dipalmitoyl-*sn*-glycero-3-phosphocholine (DPPC) and 1,2-distearoyl-*sn*-glycero-3-phospho-(10-*rac*-glycerol) sodium salt (DSPG) were kindly gifted by Lipoid (Ludwigshafen, Germany). Pirfenidone (5-methyl-1-phenylpyridin-2(1H)-one) was obtained from MedChem Express (Monmouth Junction, NJ, USA). Zinc chloride (98% purity, reagent grade),

alginate sodium salt from brown algae, chitosan medium molecular weight (75-85% deacetylated) and methyl viologen dichloride hydrate (98% purity) were purchased from Sigma-Aldrich-Merck (St Louis, MO, USA). Caffeine (Ph. Eur. quality) was purchased from Hanseler Swiss Pharma. Sodium Acetate (99% purity, ACS grade) and HEPES salt was obtained from Carl Roth (Karlsruhe, Germany). 1,1'-dioctadecyl-3,3,3',3'-tetramethylindodicarbocyanine, 4-chlorobenzenesulfonate salt (DiD, catalog number: D7757) was bought from Thermo Fisher Scientific (Waltham, MA, USA). All organic solvents (chloroform, methanol, acetonitrile, and tetrahydrofuran (THF)) were obtained from Fisher Scientific (Schwerte, Germany). All chemicals were used as received. Ultrapure water of resistivity 18.2 M $\Omega$ .cm was produced by a Barnstead Smart2 pure device from Thermo Scientific (Pittsburgh, USA).

#### *Preparation of PFD-liposomes*

PFD-liposomes were prepared by means of the film hydration method, as previously reported.<sup>46</sup> The stock solutions of DPPC and DSPG in chloroform were mixed at concentration 75 mol% and 25 mol% of the respective phospholipids and 0.05 mol% DiD to reach a final total lipid concentration of 2 mM. The organic solvent was evaporated under a nitrogen stream until dry. Solvent traces were removed by vacuum overnight. After hydration with PFD (40 mM) dissolved in acetate buffer (30 mM, pH 5.5) at different molar ratio (drug-to-lipid) and six freeze-thaw cycles, the liposome formulation was extruded 10 times through a 200 nm polycarbonate membrane (Sterlitech Corporation, USA) at 70 C using a LIPEX extruder (Evonik, Canada).

#### *Preparation of LbL-LIPs*

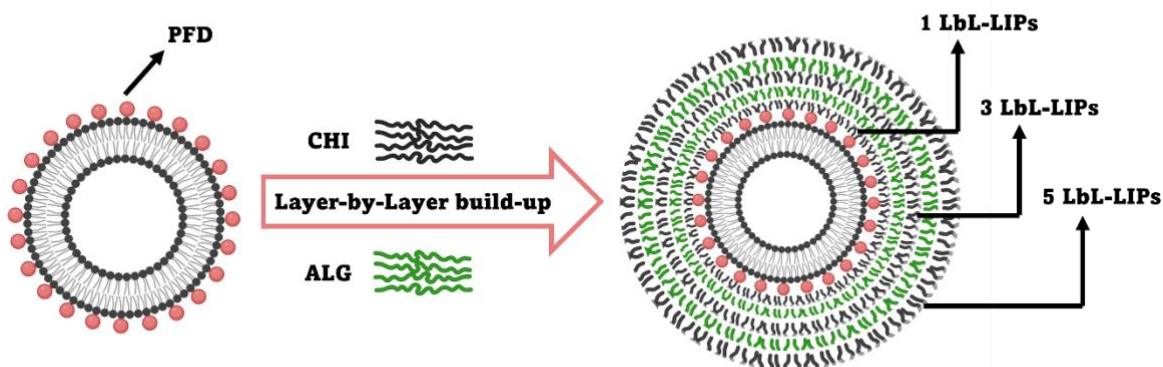


**Figure 1:** Schematic illustration of the preparation of LbL-LIPs. The concentration of liposomes and PFD is 2 mM and 10 mM respectively. The final volume of LbL-LIPs is 1 mL. Final concentration of CHI in 1 LbL-LIPs is 0.04 wt%; final

concentration of CHI and ALG in 3 LbL-LIPs is 0.075 wt% and 0.04 wt% respectively; in 5 LbL-LIPs is 1.1 wt% and 0.075 wt% respectively.

Immediately after the extrusion, the first biopolymer layer was directly deposited onto the negatively charged liposomes. For this purpose, 20  $\mu$ L of 2% (w/v) chitosan (CHI) solution at pH 4.2 was added to 1 mL of 2mM PFD-liposomes and incubated for 3 min under gentle stirring. The subsequent alginate (ALG) layer was deposited by adding 20  $\mu$ L of the 2% (w/v) biopolymer solution at pH 5.5 to the CHI-liposomes, followed by 3 min incubation under gentle stirring. The successive deposition of layer(s) was performed with the same procedure alternating CHI and ALG (**Figure 1**). The robustness of the LbL preparation was evaluated via intra-laboratory tests. The concentration of biopolymers used to prepare the LbL-LIPs was selected based on a preliminary study (in the Appendix, **A2.1**).

### *Drug Loading*

After the production of LbL-LIPs, the unencapsulated drug was removed by dialysis with a Slide-A-Lizer MINI Dialysis device (Thermo Scientific; MW cutoff 20 MWCO) against 45 mL of acetate buffer 30 mM, pH 5.5 at room temperature. The dialysis time (2 h) was chosen by analyzing the amount of drug retained by the membrane via HPLC (in the Appendix, **A2.2**). The PFD concentration was determined by reverse-phase liquid chromatography using a Macherey-Nagel Nucleosil 100-5 C18 (4.0 x 250 mm; 5.0  $\mu$ m particle size) column. The mobile phase consisted of acetonitrile/water (65:35 v/v) + 0.1% trifluoroacetic acid at a flow rate of 0.7 mL/min, temperature 25 °C and UV detection at  $\lambda = 317$  nm. An internal standard (caffeine, 20  $\mu$ g/mL) was added to each sample to correct for inter-injection variation.<sup>47</sup>

Drug loading (DL) was calculated using the following equation:

$$DL\% = \frac{\text{amount of drug retained}}{\text{amount of lipid}} * 100$$

The amount of lipid was determined via UHPLC-CAD (in the Appendix, **A2.3**) using a method previously developed in our group.<sup>48</sup>

### *Particle size and zeta potential*

The mean hydrodynamic diameter and the polydispersity index (PDI) of the PFD-liposomes were determined using Litesizer 500 (Anton Paar, Graz, Austria) at 25 °C with a backscatter angle of 175° and 658 nm laser. The number of measurements were 6 while refractive index 1.3304 and viscosity

0.89 mPa/s were set for the solvent. The samples were placed in disposable polystyrene cuvettes of 1 cm optical path length. The zeta ( $\zeta$ ) potential was determined by laser Doppler micro-electrophoresis using the same instrument. The minimum number of measurements were 100 and Henry factor 1.50 while refractive index 1.33 and viscosity 0.89 mPa/s were set for the solvent. The samples were placed in Omega cuvette (Anton Paar, Graz, Austria). The data evaluation was carried out using Anton Paar Kalliope Software from the Smoluchowski equation. The samples were diluted to a concentration of 0.5 mM with distilled water.

### *Hydrogel preparation*

To prepare the hydrogel, sodium alginate was dissolved in HEPES buffer (30 mM HEPES at pH 7.4) to 2% (w/v) concentration. Gelation occurred when the ALG solution was mixed with zinc chloride (4:1 alginate to zinc chloride volume ratio) with two Luer lock syringes connected with Combifix adapter (B. Braun, Melsungen, Germany). For the LbL-LIP-Gel, LbL-LIPs loaded with PFD were first purified to remove the free drug and later mixed with the ALG solution. The resulting solution was mixed with zinc chloride following the same procedure as before. The final concentration of ALG and zinc chloride was 2% w/v and 20 mM respectively. The hydrogel was immediately used for the release studies.

### *Rheology*

The rheological measurements were performed using an oscillatory rheometer (Modular Compact Rheometer MCR 72 from Anton Paar, Graz, Austria) in a cone-plate geometry, 0.993° angle, and 49.942 mm diameter. The temperature of the plate was set at 25 °C. First, amplitude sweeps were carried out to determine the linear viscoelastic region of each formulation at 1 Hz between 0.01 and 100% strain. Secondly, frequency sweeps were performed using a constant strain in the linear viscoelastic region between 0.1 and 100 rad/s.

### *Fluorescence quenching experiments*

Fluorescence quenching of a free PFD solution in acetate buffer 30 mM and PFD entrapped in liposomes were performed after dialysis treatment using methyl viologen dichloride ( $MVD^+$ ) as a collisional quencher. All fluorescence experiments were carried out using a microplate reader (Spark 10M, Tecan, Switzerland) at 25 °C on solutions with optical densities smaller than 0.05 to minimize the inner filter effects. Experiments were performed by adding concentrations from 20 mM to 100 mM of  $MVD^+$  solution to the samples. Afterwards, the fluorescence intensity of PFD was monitored

at 396 nm by exciting at 318 nm. Quenching of fluorescence is described by the Stern-Volmer equation using the following equation:

$$F_0/F = K_D \times [MVD^+]$$

where  $F_0$  and  $F$  are the fluorescence intensity in absence or in presence of the quencher, respectively;<sup>49</sup>  $K_D$  ( $1/M \times s$ ) is the quenching constant and  $[MVD^+]$  is the quencher molar concentration. The plot of  $F_0/F$  versus  $[MVD^+]$  is expected to be linearly dependent upon the concentration of quencher and it yields an intercept of one on the y-axis and a slope equal to the Stern-Volmer quenching constant  $K_D$  ( $1/M \times s$ ) when the quenching process is dynamic. Fare clic o toccare qui per immettere il testo.

#### *Transmission electron cryomicroscopy (Cryo-TEM)*

For the morphological investigation of 1 LbL-LIPs and 3 LbL-LIPs using cryo-TEM, 3  $\mu$ L of each sample were deposited on lacey carbon films (Cu 200 mesh grid, Quantifoil Micro Tools, Germany) and then plunge-frozen with Vitrobot (FEI, USA). The blotting chamber conditions were set to 4°C, 100% humidity and 4 s blot time. Excess of liquid was blotted automatically between two strips of filter paper. Grids were stored in liquid nitrogen until TEM observation. Low-dose electron diffraction was performed on a Tecnai Spirit G2 electron microscope (FEI, USA) with a Gatan 626 cryoholder. The images were recorded by an Olympus-SIS Veleta CCD camera.

#### *Fluorescence microscopy*

To investigate 5-LbL-LIPs morphology, liposomes were stained with the non-exchangeable lipophilic dye DiD. Fluorescence microscopy images were analyzed using a Nikon Eclipse-Ti inverted fluorescence microscope (Nikon, Mississauga, Canada) with Tx red filter. A volume of 20  $\mu$ L of LbL-LIPs was placed on a slide and covered with a glass coverslip.

#### *Release experiments*

All formulations' drug release profiles were tested *in vitro* with vertical diffusion cells (PermeGear, Pennsylvania, USA) and a 3000 nm polycarbonate membrane (Sterlitech Corporation, USA). Preliminary experiment showed that 100% of the PFD solution (in the Appendix, **A2.4**) passes through the polycarbonate membrane, thus excluding any interference with the release studies. The donor chamber contained 8 mL release medium: either HEPES buffer (30 mM) at pH 7.4 or acetate buffer (30 mM) at pH 4.2 to mimic pH conditions in the colon and vagina, respectively. All the release studies were carried out in sink conditions. The loaded Franz cells were placed in a shaking incubator at 100 rpm and 37 °C. For LbL-LIPs and LbL-LIP-Gel, 200  $\mu$ L and 20 mg were placed directly in

the donor chamber respectively. At predetermined time points of 1, 2, 3, 4, 5, 20, and 24 h, the release medium was completely replaced, and 1 mL aliquot was lyophilized. Each sample was resuspended with the internal standard caffeine and the PFD content was analyzed by HPLC.

### *Statistical analysis*

All experiments were carried out in triplicate and the values are represented as mean  $\pm$  standard deviation. Fresh samples were used unless otherwise stated.

## 3. Results and discussion

PFD is an orally available anti-fibrotic drug. Although effective, its rapid clearance necessitating dosing frequency, and its toxicity may limit the clinical application.<sup>19,50</sup> Therefore, the therapeutic value of PFD can be improved by encapsulating it in drug delivery system which allow its targeted and sustained release to the fibrotic site. Recently, several strategies based on various biomaterials (e.g., nanoparticles and microparticles) have emerged as possible carriers for PFD.<sup>23,29,51–56</sup> For example, poly(lactide-*co*-glycolide) nanoparticles able to release the drug locally in the lungs after intratracheal administration.<sup>22</sup> Chitosan microspheres were also found to attenuate pulmonary fibrosis upon inhalation.<sup>23</sup> However, the majority of these studies focused on lung targeting delivery, and to the best of our knowledge, no studies have been conducted toward a platform to treat fibrosis in multiple organs locally (e.g., rectal and/or vaginal delivery).

To deliver a sufficient amount of drug providing therapeutic effect, a high drug loading is desirable. However, due to the physico-chemical properties – mainly hydrophilicity and low molecular weight - of PFD, this specific drug interacts weakly with many conventional drug carriers - such as chitosan microspheres and hydrogels - leading to low drug loadings and fast release. Additionally, a clear size-dependent difference regarding distribution of particles in the inflamed intestinal mucosa of IBD patients was demonstrated.<sup>57</sup> Upon rectal administration, unlike nanoparticles, which are known to cross the epithelial barrier, potentially leading to systemic absorption, microparticles accumulate and bioadhere to the inflamed mucosa wall. Aiming at developing a rational microparticulate system based on earlier research of our group,<sup>58</sup> we selected negatively charged liposomes for the high PFD loadings they were reported to grant<sup>59,60</sup> and for the possibility to tailor their surface properties to improve local delivery. Nevertheless, several attempts to replicate previous studies<sup>59,60</sup> resulted in low amount of drug encapsulated (data not shown). Here, we developed a robust and highly



concentrated liposome-based system able to deliver the small and water-soluble PFD. Such local delivery system is surface capped with biopolymers able to tune the drug release profile.

#### *Size, $\zeta$ -potential and drug loading*

The results of drug loading, size distribution and  $\zeta$ -potential for liposomes prepared by the film hydration method and extruded through 200 nm polycarbonate membrane are shown in **Table 1**. In agreement with a previous study,<sup>59</sup> a passive loading method resulted to be a better approach to encapsulate PFD in the liposomes than active loading strategy. The negatively charged liposomes of DPPC/DSPG at a molar ratio of 75/25 (mol%) was chosen to increase the drug encapsulation – owing to the saturated acyl chains of the phospholipids – and different drug-to-lipid ratios were assessed. The most important findings were the results of PFD content and DL. As seen in the **Table 1** increasing the drug-to-lipid ratio improved drug loading efficiency. The formulation with the highest drug loading (507.2%, which corresponds to  $1.89 \pm 0.3$  mg/mL PFD concentration and total lipid concentration of 2 mM) was used in all further experiments.

**Table 1:** Average particle size (nm), polydispersity index (PDI),  $\zeta$  potential (mV), drug loading (DL, %) with different drug-to-lipid ratio combinations. The concentration of liposomes (2 mM) is constant while the PFD concentration varies according to the drug-to-lipid ratio. Data shown are the mean  $\pm$  SD ( $n \geq 3$ ).

<b>Drug-to-lipid ratio (mol:mol)</b>	<b>Particle size (nm)</b>	<b>PDI</b>	<b><math>\zeta</math>-potential (mV)</b>	<b>DL (%)</b>
<b>1:20</b>	$120.6 \pm 1.90$	$0.15 \pm 0.02$	$-30.13 \pm 5.79$	2.6
<b>1:10</b>	$126.05 \pm 6.49$	$0.12 \pm 0.02$	$-32.16 \pm 6.99$	1.5
<b>1:1</b>	$116.26 \pm 1.10$	$0.11 \pm 0.01$	$-41.63 \pm 0.80$	23.7
<b>10:1</b>	$127.43 \pm 0.80$	$0.06 \pm 0.02$	$-42.96 \pm 0.16$	205.8
<b>20:1</b>	$122.21 \pm 2.71$	$0.05 \pm 0.02$	$-34.5 \pm 0.86$	507.2

#### *Fluorescence quenching experiments*

The PFD location in the liposome after drug loading was studied with fluorescence quenching experiments. To gather information about the liposomal surface, we chose the collisional quencher MVD<sup>+</sup>. The quencher does not penetrate the bilayer and the electrostatic interaction with the negatively charged liposomes would immobilize it on the surface.<sup>61</sup> Thus, by measuring the quenching of the PFD fluorescence emission in presence of MVD<sup>+</sup>, it is possible to assess the accessibility of the drug to the quencher. As shown in the **Figure 2**, the quenching of fluorescence is described by the Stern-Volmer equation in the case of free PFD and PFD-liposomes. Thus,

fluorescence quenching data, presented as plot of  $F_0/F$  versus  $[MVD^+]$ , show in both cases a linear behavior. This indicates that PFD can be homogeneously approached by the quencher, implying that the drug is located close to the liposome surface. These findings suggest that PFD included in DPPC/DSPG liposomes is adsorbed on the surface of the liposomes as also indicated by the extremely fast release of the drug loaded in plain liposomes (in the Appendix, A2.5). PFD may be in a location, driven by H-bond and  $\pi$ -interactions, close to the phospholipid headgroups and hence more accessible to the cation quencher (Figure 2).

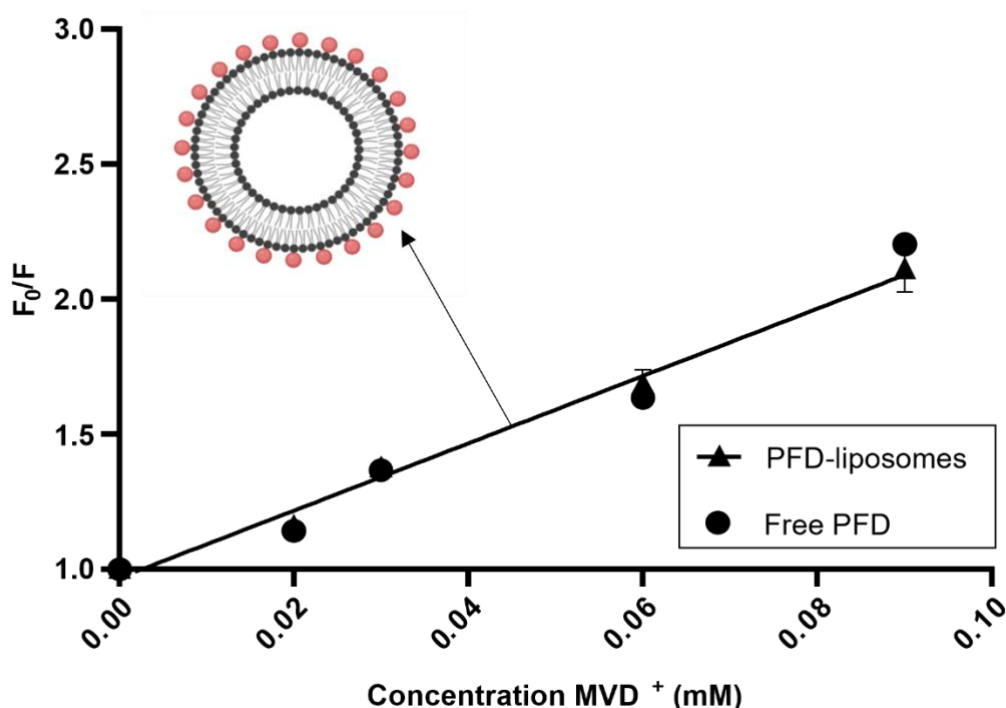


**Figure 2:** Fluorescence quenching release of free PFD drug in comparison with PFD liposomes and LbL-LIPs. Data are shown as mean  $\pm$ SD.

Due to the nature of drug encapsulation and the fast drug release, we hypothesized that a polymer-based layer-by-layer approach could have modulated PFD release via surface capping. The initially negative charge of the liposomes makes them suitable for the subsequent build-up of biopolymers. The latter was monitored with  $\zeta$ -potential (*vide infra*). To facilitate clinical translation, we based our preliminary considerations on biocompatible and commercially available biopolymers. We thus selected ALG<sup>62</sup> and CHI<sup>63</sup> for the further coating.

#### Layer-by-Layer

After having screened a series of conditions (in the Appendix, A2.1), a concentration of 0.04 wt% of the biopolymers was selected for the layer formation, since this was slightly above the required

saturation concentration as indicated by the  $\zeta$ - potential. Upon addition of CHI (**Figure 3a**), the  $\zeta$ - potential of liposomes reaches +19 mV which rapidly decreases to -24 mV in addition of ALG. Furthermore, we observed visible aggregate formation in 2+ layered liposomes. Simultaneously, the Cryo-TEM observations revealed that the aggregation was present in all formulations and their size became increasingly larger when polymers were repeatedly added (**Figure 3b-d**). Due to the extent of the aggregation, 5 LbL-LIPs could not be analyzed using Cryo-TEM. To this aim, 5-LbL-LIPs were stained with the lipophilic fluorescent dye DiD and visualized through fluorescent microscopy (**Figure 3e**). Since the electrostatic interaction is the dominant factor in the deposition, we hypothesized that the biopolymers would approach each other as a consequence of the strong electrostatic force. Hence, the attraction between oppositely countercharged biopolymers would drive the interaction despite the fact that their chain may not be optimally rearranged. The failure of optimal reorientation of the chain may result in non-homogeneous coating which would trigger the aggregation process. Interestingly, we observed that the extent of aggregation does not affect the reproducibility of the drug release.

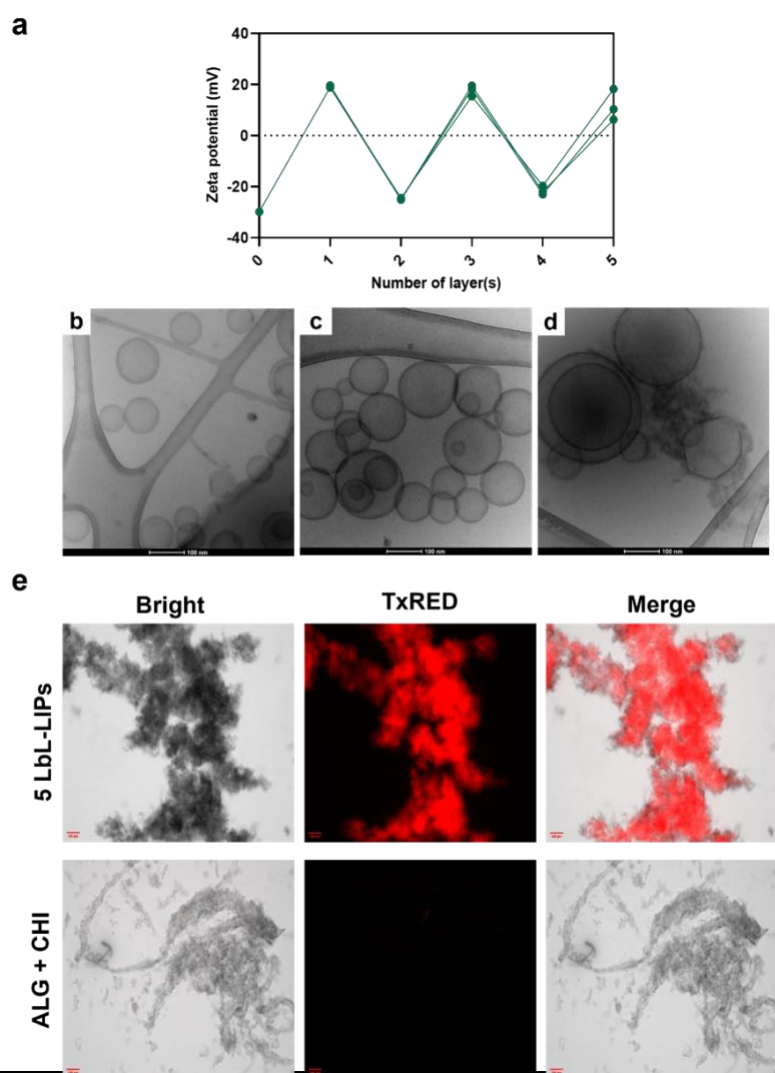


**Figure 3:** In panel **a)** changes in  $\zeta$ -potential of coated liposomes using CHI and ALG alternatively. Data shown are shown as individual measurements. Representative cryo-TEM images of **b)** PFD-liposomes; **c)** 1-LbL-LIPs; **d)** 3-LbL-LIPs; **e)** 5-LbL-LIPs.

To improve the topical applicability of such system and to enhance its long-term physical stability, we integrated the aggregated liposomes into zinc alginate hydrogel. During the study design, we selected alginate and zinc for their inflammation-targeting and anti-inflammatory properties, respectively. Here, we propose a synergistic combination of the tunable aggregated liposomes and instantaneously cross-linked zinc alginate hydrogel as mucosal drug delivery system for PFD.

#### *Rheological measurements*

The production of LbL-LIP-Gel was successfully obtained via ionotropic gelation and the rheological properties were further investigated. Frequency sweeps are proven methods for gathering information on the behavior and inner structure of polymers as well as on the long-term physical stability of hydrogels. High frequencies are used to simulate fast motion on short timescales, whereas low frequencies simulate the behavior on long timescales or at rest. Prior to the test, it was confirmed by amplitude sweep (in the Appendix, **A2.6**) that the amplitude value selected was within the linear viscoelastic region (LVE) region. By varying the frequency, all hydrogels showed the characteristic rubber plateau where storage modulus ( $G'$ ) is higher than the loss modulus ( $G''$ ) particularly with reference to the high frequency range - thus prevalence of elastic properties (**Figure 4**). The addition of LbL-LIPs does not result in significant modification of their rheological characteristics. Long-term storage behavior is evaluated in the lower frequency range. The  $G' > G''$  indicates a stable network meeting the precondition for physical long-term stability- thus avoiding precipitation.

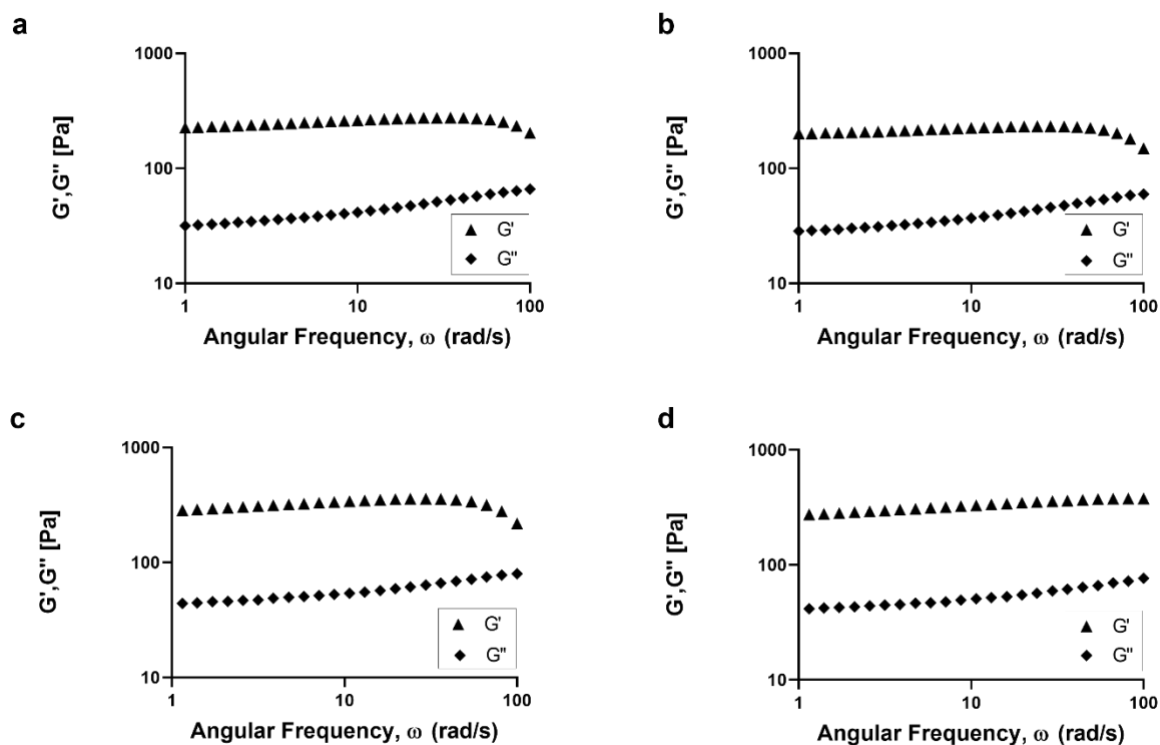


**Figure 4:** Frequency sweep of **a)** ALG hydrogel 2% crosslinked with ZnCl and ALG hydrogel in presence of **b)** 1 LbL-LIPs, **c)** 3 LbL-LIPs and **d)** 5 LbL-LIPs. Data shown as angular frequency (rad/s) on the x-axis and storage modulus  $G'$  and loss modulus  $G''$  plotted on the y-axis; both on a logarithmic scale.

#### *In vitro release studies*

Drug release profiles of LbL-LIPs and LbL-LIP-Gel were monitored at pH 7.4 and 4.2 to mimic the intestine and vaginal milieu. As shown in **Figure 5**, the release of PFD decreases with increasing the number of layers. In general, the release profiles result faster in the first hours and followed by a steady release rate. The results showed that the layering process is a crucial and required step for the final formulation. A possible explanation for this may be the interactions that can occur during the layering process: (i) chitosan can participate in hydrophobic interaction - owing to its remaining acetyl groups - with PFD (ii) and H-bonding. This suggests either immobilization of the drug between the liposomes structure and the 3D biopolymer network and/or an extremely slow diffusion coefficient through the deposited biopolymers. Several control experiments were performed (in the Appendix, A2.7) to confirm that the subsequent addition of biopolymers was a necessary step for the controlled release of PFD. Additionally, data show that the system is pH-independent making it suitable also for the delivery in more acidic environment.

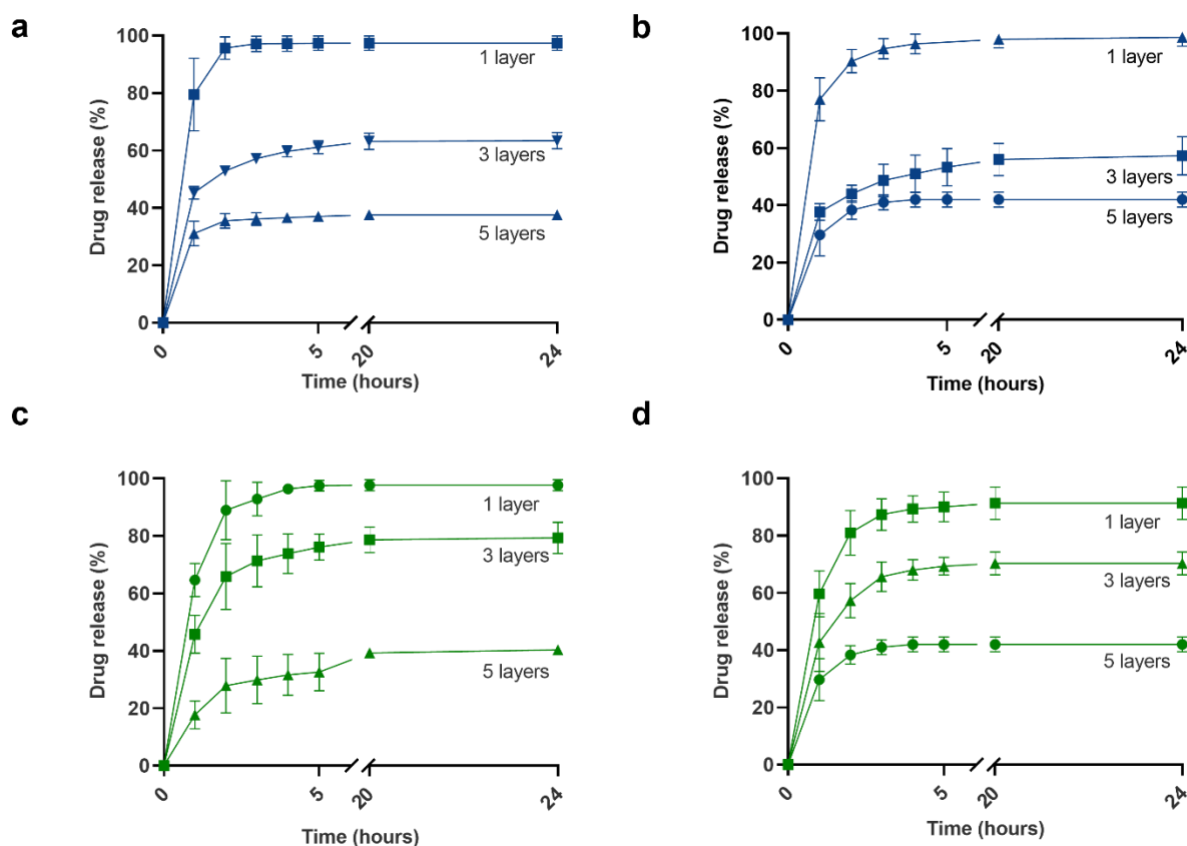


**Figure 5:** *In vitro* release of all formulations. Release of liposomal PFD at pH 7.4 of LbL-LIPs (panel **a**) and at pH 4.2 (panel **b**). Release of PFD from the liposomal gel LbL-LIP-Gel at pH 7.4 (panel **c**) and at pH 4.2 (panel **d**). Mean  $\pm$  SD, n=3.

The intrinsic mucoadhesive properties of alginate hydrogel should potentially improve the delivery of PFD when compared to PFD enema, in vaginal and rectal tissue. We reason that these features should prolong the retention time and promote the drug availability at the fibrotic site. Regrettably, the lack of suitable *in vivo* fibrosis models of IBD and endometriosis precludes a preclinical efficacy study of our formulation.

#### 4. Conclusions

We developed a new strategy able to provide a topical sustained release of the small hydrophilic PFD using liposomes and commercially available biopolymers. Compared to other approaches, the current strategy has the advantage to result in ultrahigh drug loading and tunable release profiles compatible with mucosal drug delivery. Furthermore, the incorporation of our tunable liposomal aggregates into zinc alginate hydrogel has the potential to improve the mucoadhesive properties in rectal and vaginal tissue. We envision that the release of zinc ions, known for their anti-inflammatory properties, and

PFD would synergistically improve the anti-fibrotic therapy. Future *in vivo* studies in experimental fibrotic models will help validating the toxicity and the pharmacokinetics of our local therapeutic approach.

## 5. References

- Henderson, N. C., Rieder, F., Wynn, T. A. Fibrosis: from mechanisms to medicines. *Nature* **587**, 555–566 (2020).
- Nanthakumar, C. B., Hatley, R., Lemma, S., Gaudie, J., Marshall, R. P., Macdonald, S., J., F. Dissecting fibrosis: therapeutic insights from the small-molecule toolbox. *Nat. Rev. Drug Discov.* **14**, 693–720 (2015).
- Long, Q., Liu, Z., Shao, Q., Shi, H., Huang, S., Jiang, C., Qian, B., Zhong, Y., He, X., Xiang, X., Yang, Y., Li, B., Yan, X., Zhao, Q., Wei, X., Santos, H.A., Ye, X. Autologous Skin Fibroblast-Based PLGA Nanoparticles for Treating Multiorgan Fibrosis. *Adv Sci Lett* **9(21)**, 2200856 (2022).
- Rogliani, P., Calzetta, L., Cavalli, F., Matera, M. G. & Cazzola, M. Pirfenidone, nintedanib and N-acetylcysteine for the treatment of idiopathic pulmonary fibrosis: A systematic review and meta-analysis. *Pulm Pharmacol Ther* **40**, 95–103 (2016).
- Khanum, B. N. M. K., Guha, R., Sur, V.P., Nandi, S., Basak, S.K., Konar, A., Hazra S. Pirfenidone inhibits post-traumatic proliferative vitreoretinopathy. *Eye* **31**, 1317–1328 (2017).
- Lewis, G. A., Dodd, S., Clayton, D., Bedson, E., Eccleson, H., Schelbert, E.B., Naish, J.H., Jimenez, B.D., Williams, S.B., Cunnington, C., Ahmed, F.Z., Cooper, A., Viswesvariah, R., Russell, S., McDonagh, T., Williamson, P.R., Miller, C.A. Pirfenidone in heart failure with preserved ejection fraction: a randomized phase 2 trial. *Nat. Med.* **27**, 1477–1482 (2021).
- Li, C., Rezov, V., Joensuu, E., Vartiainen, V., Rönty, M., Yin, M., Myllärniemi, M., Koli, K. Pirfenidone decreases mesothelioma cell proliferation and migration via inhibition of ERK and AKT and regulates mesothelioma tumor microenvironment in vivo. *Sci. Rep.* **8**, 1–14 (2018).
- Hall, C. L., Wells, A. R. & Leung, K. P. Pirfenidone reduces profibrotic responses in human dermal myofibroblasts, in vitro. *Lab. Invest.* **98(5)**, 640–655 (2018).
- Miric, G., Dallemagne, C., Endre, Z., Margolin, S., Taylor, S.M., Brown, L. Reversal of cardiac and renal fibrosis by pirfenidone and spironolactone in streptozotocin-diabetic rats. *Br J Pharmacol* **133(5)**, 687–694 (2001).
- Lee, K. W., Everett 4th, T.H., Rahmutula, D., Guerra, J.M., Wilson, E., Ding, C., Olgin, J.E. Pirfenidone prevents the development of a vulnerable substrate for atrial fibrillation in a canine model of heart failure. *Circulation* **114(16)**, 1703–1712 (2006).
- Armendariz-Borunda, J., Lyra-Gonzalez, I., Medina-Preciado, D., Gonzalez-García, I., Martínez-Fong, D., Miranda, R.A., Magaña-Castro, R., Peña-Santoyo, P., García-Rocha, S., Bautista, C.A., Godoy, J., Flores-Montana, J., Floresvillar-Mosqueda, J., Armendariz-Vazquez, O., Lucano-Landeros, M.S., Vazquez-Del Mercado, M., Sanchez-Parada, M.G., *Ann Plast Surg*, A controlled clinical trial with pirfenidone in the treatment of pathological skin scarring caused by burns in pediatric patients. *Ann Plast Surg* **68**, 22–28 (2012).
- di Sario, A., Bendia, E., Macarri, G., Candelaresi, C., Taffetani, S., Marzioni, M., Omenetti, A., De Minicis, S., Trozzi, L., Benedetti, A. The anti-fibrotic effect of pirfenidone in rat liver fibrosis is mediated by downregulation of procollagen alpha1(I), TIMP-1 and MMP-2. *Dig Liver Dis* **36(11)**, 744–751 (2004).
- AI-Bayati, M. A., Xie, Y., Mohr, F. C., Margolin, S. B., Giri, S. N. Effect of pirfenidone against vanadate-induced kidney fibrosis in rats. *Biochem Pharmacol* **64(3)**, 517–525 (2002).
- Distler, J. H. W., Györfi, A.H., Ramanujam, M., Whitfield, M.I., Königshoff, M., Lafyatis, R. Shared and distinct mechanisms of fibrosis. *Nat Rev Rheumatol* **15**, 705–730 (2019).
- Karatzas, E., Bourdakou, M. M., Kolios, G., Spyrou, G. M. Drug repurposing in idiopathic pulmonary fibrosis filtered by a bioinformatics-derived composite score. *Scientific Reports* **7**, 12569 (2017).
- Esbriet | European Medicines Agency. <https://www.ema.europa.eu/en/medicines/human/EPAR/esbriet>.
- Drug Approval Package: Brand Name (Generic Name) [https://www.accessdata.fda.gov/drugsatfda\\_docs/nda/2014/022535Orig1s000toc.cfm](https://www.accessdata.fda.gov/drugsatfda_docs/nda/2014/022535Orig1s000toc.cfm).
- E. Bendstrup, V. Cottin, P. Dewint, J. J. J. Egan, J. Ferguson, R. Groves, P. M. Hellström, M. Kreuter, T. M. Maher, M. Molina-Molina, K. Nordlind, A. Sarafidis and C. Vancheri, Adv Ther, Phase 3 Trial of Pirfenidone in Patients with Idiopathic Pulmonary Fibrosis. *N Engl J Med* **22**, 2083–92 (2014).
- Costabel, U., Bendstrup, E., Cottin, V., Dewint, P., Egan, J.J.J., Ferguson, J., Groves, R., Hellström, P.M., Kreuter, M., Maher, T.M., Molina-Molina, M., Nordlind, K., Sarafidis, A., Vancheri, C. Pirfenidone in idiopathic pulmonary fibrosis: Expert panel discussion on the management of drug-related adverse events. *Adv Ther* **31(4)**, 375–391 (2014).
- Galli, J. A., Pandya, A., Vega-Olivo, M., Dass, C., Zhao, H., Criner, G.J. Pirfenidone and nintedanib for pulmonary fibrosis in clinical practice: Tolerability and adverse drug reactions. *Respirology* **22(6)**, 1171–1178 (2017).
- Hughes, G., Toellner, H., Morris, H., Leonard, C., Chaudhuri, N. Real World Experiences: Pirfenidone and Nintedanib are Effective and Well Tolerated Treatments for Idiopathic Pulmonary Fibrosis. *J Clin Med* **5(9)**, 78 (2016).
- Trivedi, R., Redente, E. F., Thakur, A., Riches, D. W. H., Kompella, U. B. Local delivery of biodegradable pirfenidone nanoparticles ameliorates bleomycin-induced pulmonary fibrosis in mice. *Nanotechnology* **23(50)**, 505101 (2012).
- Li, D., Gong, L. Preparation of novel pirfenidone microspheres for lung-targeted delivery: in vitro and in vivo study. *Drug Des Devel Ther* **10**, 2815 (2016).
- Sun, G., Lin, X., Zhong, H., Yang, Y., Qiu, X., Ye, C., Wu, K., Yu, M. Pharmacokinetics of pirfenidone after topical administration in rabbit eye. *Mol Vis* **6**, 2191 (2011).
- Zhang, B., Ding, Z., Dong, J., Lin, F., Xue, Z., Xu, J. Macrophage-mediated degradable gelatin-coated mesoporous silica nanoparticles carrying pirfenidone for the treatment of rat spinal cord injury. *Nanomedicine* **37**, 102420 (2021)
- Zires, J.M., Valdes, P.A., Wiechers, A.C.U., Comboni, S.C.J., Gutiérrez, J.L., Jiménez, J.J.E., Pérez, F.J.G. Topical Administration of Pirfenidone Increases Healing of Chronic Diabetic Foot Ulcers: A Randomized Crossover Study. *J Diabetes Res* **2016**, 7340641 (2016).
- Rodríguez-Castellanos, M., Tlacuilo-Parra, A., Sánchez-Enríquez, S., Vélez-Gómez, E., Guevara-Gutiérrez, E. Pirfenidone gel in patients with localized scleroderma: A phase II study. *Arthritis Res Ther* **16(6)**, 510 (2014).
- El-Halwagy, A. S., Al-Gergawy, A. A., Dawood, A. S., Shehata, A. Reduction of Postoperative Adhesions after Laparoscopic Surgery for Endometriosis by Using a Novel Anti-Fibrotic Drug Pirfenidone: A Randomized Double Blind Study. *Gynecology e Obstetrics* **7**, 1–6 (2017).
- Fayzullin, A., Churbanov, S., Ignatieva, N., Zakharkina, O., Tokarev, M., Mudryak, D., Khristidis, Y., Balyasin, M., Kurkov, A., Golubeva, E.N., Aksenova, N.A., Dyuzheva, T., Timashev, P., Guller, A., Shekhter, A. Local Delivery of Pirfenidone by PLA Implants Modifies Foreign Body Reaction and Prevents Fibrosis. *Biomedicines* **9**, 853 (2021).



30. Bao, Y., Huang, L., Huang, X., Gao, C., Chen, Y., Zhu, L.W.S., Song, Y. Pirfenidone ameliorates the formation of choroidal neovascularization in mice. *Mol Med Rep* **21**, 2162–2170 (2020).
31. Zhong, H., Sun, G., Lin, X., Wu, K., Yu, M. Evaluation of Pirfenidone as a New Postoperative Antiscarring Agent in Experimental Glaucoma Surgery. *Invest ophthalmol vis sci* **52**, 3136–42 (2011).
32. Jung, K. I., Park, C. K. Pirfenidone inhibits fibrosis in foreign body reaction after glaucoma drainage device implantation. *Drug Des Devel Ther* **10**, 1477–1488 (2016).
33. Rieder, F., Brenmoehl, J., Leeb, S., Schö, J., Rogler, G. Wound healing and fibrosis in intestinal disease. *Gut* **56**, 130–139 (2007).
34. Rieder, F., Fiocchi, C., Rogler, G. Mechanisms, Management, and Treatment of Fibrosis in Patients with Inflammatory Bowel Diseases. *Gastroenterol* **152**, 340–350 (2017).
35. Rieder, F., Fiocchi, C. Intestinal fibrosis in IBD-A dynamic, multifactorial process. *Nat Rev Gastroenterol Hepatol* **6**, 228–235 (2009).
36. Meier, R., Lutz, C., Cosin-Roger, J., Fagagnini, S., Bollmann, G., Hünerwadel, A., Mamie, C., Lang, S., Tchouboukov, A., Weber, F.E., Weber, A., Rogler, G., Hausmann, M. Decreased fibrogenesis after treatment with pirfenidone in a newly developed mouse model of intestinal fibrosis. *Inflamm Bowel Dis* **22**, 569–82 (2016).
37. Stewart, E. A., Laughlin-Tommaso, S.K., Catherino, W.H., Lalitkumar, S., Gupta, D., Vollenhoven, B., Uterine fibroids. *Nat Rev Dis Primers* **2**, 16043 (2016).
38. Hu, Q., Jiang, P., Feng, Y., Xu, Y., Zhou, N., Chen, W., Zhu, L., Hu, L., Zhou, Z. Noninvasive assessment of endometrial fibrosis in patients with intravoxel incoherent motion MR imaging. *Sci Rep* **11**, 1–8 (2021).
39. Saunders, P. T. K., Horne, A. W. Endometriosis: Etiology, pathobiology, and therapeutic prospects. *Cell* **184**, 2807–2824 (2021).
40. Matsuzaki, S., Pouly, J. L., Canis, M. Dose-dependent pro- or anti-fibrotic responses of endometriotic stromal cells to interleukin-1 $\beta$  and tumor necrosis factor  $\alpha$ . *Sci Rep* **10**, 1–12 (2020).
41. Lee, B. S., Margolin, S. B., Nowak, R. A. Pirfenidone: A Novel Pharmacological Agent That Inhibits Leiomyoma Cell Proliferation and Collagen Production. *J Clin Endocrinol Metab* **83**, 219–223 (1998).
42. Hasdemir, P. S., Ozkut, M., Guvenal, T., Uner, M.A., Calik, E., Koltan, S.O., Koyuncu, F.M., Ozbilgin, K. Effect of Pirfenidone on Vascular Proliferation, Inflammation and Fibrosis in an Abdominal Adhesion Rat Model. *J invest Surg* **30**, 26–32 (2016).
43. Bulletti, C., de Ziegler, D., Flamigni, C., Giacomucci, E., Polli, V., Bolelli, G., Franceschetti, F. Targeted drug delivery in gynaecology: the first uterine pass effect. *Human Reproduction* **12**, 1073–1079 (1997).
44. Bulletti, C., De Monstier, B., Jääskeläinen, A.S. Vaginal drug delivery: the first uterine pass effect. *Ann NY Acad Sci* **828**, 285–290 (1997).
45. Zhang, S., Ermann, J. Succi, M.D., Zhou, A., Hamilton, M.J., Cao, B., Korzenik, J.R., Glickman, J.N., Vemula, P.K., Glimcher, L.H., Traverso, G., Langer, R., Karp, J.M. An inflammation-targeting hydrogel for local drug delivery in inflammatory bowel disease. *Sci Transl Med* **7**, 1–11 (2015).
46. Valentino, G., Zivko, C., Weber, F., Brülisauer, L., Luciani, P. Synergy of Phospholipid—Drug Formulations Significantly Deactivates Profibrogenic Human Hepatic Stellate Cells. *Pharmaceutics* **11**, 676 (2019).
47. Sharma, A., Conway, W. D., Straubinger, R. M. Reversed-phase high-performance liquid chromatographic determination of taxol in mouse plasma. *J Chromatogr B Biomed Sci Appl* **655**, 315–319 (1994).
48. Weber, F., Rahnfeld, L., Luciani, P. Analytical profiling and stability evaluation of liposomal drug delivery systems: A rapid UHPLC-CAD-based approach for phospholipids in research and quality control. *Talanta* **220**, 121320 (2020).
49. Lakowicz, J. R. Principles of fluorescence spectroscopy. *Principles of Fluorescence Spectroscopy*, 1–954 (2006).
50. Lancaster, L. H., de Andrade, J.A., Zibrak, J.D., Padilla, M.L., Albera, C., Nathan, S.D., Wijssenbeek, M.S., Stauffer, J.L., Kirchgassler, K.U., Costabel, U. Pirfenidone safety and adverse event management in idiopathic pulmonary fibrosis. *Eur Respir Rev* **26**, 170057 (2017).
51. Pardeshi, S., Patil, P., Rajput, R., Mujumdar, A., Naik, J. Preparation and characterization of sustained release pirfenidone loaded microparticles for pulmonary drug delivery: Spray drying approach. *Drying technology* **39**, 337–347 (2020).
52. Abnoos, M., Mohseni, M., Mousavi, S.A.J., Ashtari, K., Ilka, R., Mehravi, B. Chitosan-alginate nano-carrier for transdermal delivery of pirfenidone in idiopathic pulmonary fibrosis. *Int J Biol Macromol* **118**, 1319–1325 (2018).
53. Silva, R. O., da Costa, B.L., da Silva, F.A., da Silva, C.N., de Paiva, M.B., Dourado, L.F.N., Malachias, A., de Souza Araújo, A.A., Nunes, P.S., Silva-Cunha, A., Treatment for chemical burning using liquid crystalline nanoparticles as an ophthalmic delivery system for pirfenidone. *Int J Pharm* **568**, 118466 (2019).
54. Wu, C., Or, P.W., Chong, J.I.T., Pathirage Don, I.K.K., Lee, C.H.C., Wu, K., Yu, M., Lam, D.C.C., Yang, Y. Extended delivery of pirfenidone with novel, soft contact lenses in vitro and in vivo. *J Ocul Pharmacol Ther* **37**, 75–83 (2021).
55. Dudhat, K., Patel, H. Preparation and evaluation of pirfenidone loaded chitosan nanoparticles pulmonary delivery for idiopathic pulmonary fibrosis. *Future J Pharm Sci* **8**, 1–14 (2022).
56. Diaz-Palomera, C. D., Vidal-Paredes, A.I., Navarro-Partida, J., Cid-Hernandez, M., Rosales-Rivera, L.C., De la Rosa-Bibiano, R., Monroy-Ramirez, H.C., Santos, A., Armendariz-Borunda, J. Topical Pirfenidone-Loaded Liposomes Ophthalmic Formulation Reduces Haze Development after Corneal Alkali Burn in Mice. *Pharmaceutics* **14**, 316 (2022).
57. Schmidt, C., Lautenschlaeger, C., Collnot, E.M., Schumann, M., Bojarski, C., Schulzke, J.D., Lehr, C.L., Stallmach, A. Nano- and microscaled particles for drug targeting to inflamed intestinal mucosa - A first in vivo study in human patients. *J Control Release* **165**, 139–145 (2013).
58. Rahnfeld, L., Thamm, J., Steiniger, F., van Hoogevest, P., Luciani, P. Study on the in situ aggregation of liposomes with negatively charged phospholipids for use as injectable depot formulation. *Colloids Surf B* **168**, 10–17 (2018).
59. Parvathaneni, V., Kulkarni, N.S., Shukla, S.K., Farrales, P.T., Kunda, N.K., Muth, A., Gupta V. Systematic Development and Optimization of Inhalable Pirfenidone Liposomes for Non-Small Cell Lung Cancer Treatment. *Pharmaceutics* **12**, 206 (2020).
60. Meng, H., Xu, Y. Pirfenidone-loaded liposomes for lung targeting: preparation and in vitro/in vivo evaluation. *Drug Des Devel Ther* **9**, 3369 (2015).
61. Bombelli, C., Bordini, F., Ferro, S., Giansanti, L., Jori, G., Mancini, G., Mazzuca, C., Monti, D., Ricchelli, F., Sennato, S., Venanzi, M. New cationic liposomes as vehicles of m-tetrahydroxyphenylchlorin in photodynamic therapy of infectious diseases. *Mol Pharm* **5**, 672–679 (2008).
62. Cattelan, G., Gerbolés, A.G., Foresti, R., Pramstaller, P.P., Rossini, A., Miragoli, M., Malvezzi, C.C. Alginate Formulations: Current Developments in the Race for Hydrogel-Based Cardiac Regeneration. *Front Bioeng Biotechnol* **8**, 414 (2020).
63. Hirano, S., Seino, H., Akiyama, Y., Nonaka, I. Chitosan: A Biocompatible Material for Oral and Intravenous Administrations. *Prog Polym Sci* (**270**) 283–290 (1990).

## Chapter 3

### Design and use of lipid mesophase for 3D-printed oral dosage form

Marianna Carone<sup>1</sup>, Niklaas Manten<sup>1</sup>, Garima Yadav<sup>1</sup>, Paola Luciani<sup>1</sup>, Simone Aleandri<sup>1</sup>

#### **Affiliations:**

<sup>1</sup> Department of Chemistry, Biochemistry and Pharmaceutical Sciences, University of Bern, Bern, Switzerland

Simone Aleandri and Paola Luciani contributed with the conceptualization of the project. Niklaas Manten performed the lipid mesophase screening. Garima Yadav performed the physical parameters of the 3D-printed oral dosage form.

This chapter is prepared for submission as ‘Design and use of lipid mesophase for 3D-printed oral dosage form’.

## 1. Introduction

Lipid-based formulations offer an attractive approach for enhancing the oral bioavailability of lipophilic and water-insoluble drugs<sup>1</sup>. This is typically achieved through several mechanisms, including the formation of colloidal particles within the gastrointestinal tract (GIT) that enhance drug solubility and dissolution<sup>2</sup>, the activation of the intestinal lymphatic system to decrease first-pass metabolism<sup>3</sup>, and interactions with enterocyte-based transport and metabolic processes to modify drug uptake and efflux<sup>4</sup>. These mechanisms have been demonstrated to result in increased oral bioavailability for several drugs<sup>5</sup> and have led to the commercial and clinical success of various lipid-based drug delivery systems<sup>6</sup>.

The addition of lipids in solid oral tablets has proven challenging due to the limited versatility of lipids with respect to polymers and other traditional excipients<sup>7</sup> used to produce stable and uniform tablets<sup>7</sup>. To improve the tableting process, lipids are usually converted into solid intermediates by utilizing mesoporous materials, which are then blended with suitable tableting excipients and compressed into tablets. These porous materials, though, are susceptible to external forces that can affect their morphologies and porosities<sup>8</sup>. The compression of mesoporous materials can lead to release of its lipid content, a phenomenon known as ‘squeezing effect’<sup>9,10</sup>. As a consequence, the addition of high concentration of lipids may result in over-lubrication, which would lead to poor tablet quality attributes. Furthermore, lipids exhibit sharp thermal transitions that cause them to behave as low-viscosity fluids at high temperatures generated during the compression process, compromising the tablet’s cohesion. Eutectic-like events may occur between the lipid and the active ingredients, further influencing tablet production<sup>11</sup>.

Unlike traditional tableting process, the 3D printing does not rely on compression forces but instead utilises an aqueous fluid to bind layers of formulation together to form the solid dosage form. The application of 3D printing in pharmaceuticals and personalized medicine has garnered significant interest in the field<sup>12-15</sup>. For example, 3D-printing technology enables customizable dosing<sup>16</sup>, manufacturing of polypills<sup>17-21</sup>, and offers tunable drug release<sup>22-26</sup>. This is exemplified by the approval of the first commercially available 3D-printed medication, Spritam<sup>®</sup>, by the United States Food and Drug Administration (FDA) in 2015<sup>27,28</sup>, which also demonstrated the feasibility of using 3D-printing in large-scale manufacturing<sup>12,29</sup>. Additionally, the approval granted to two new medications as Investigational New Drugs (IND) obtained by TRIASTEK in 2021 and 2022<sup>29</sup> further confirms the growing prominence of 3D

printing in the pharmaceutical industry. The most used methods for pharmaceutical and medical-grade 3D printing are inkjet printing and Semi-Solid Extrusion (SSE). Inkjet printing comprises three essential phases: droplet formation, jetting of the material, and solidification mechanism. Droplet formation can be initiated either through thermal or piezoelectric pathways<sup>30</sup>. While piezoelectric inkjet printers rely on the material's response to an applied voltage, resulting in mechanical deformation that prompts droplet formation, thermal inkjet printers utilize localized heating to induce a rapid expansion of the ink. Piezoelectric mechanism is favored over the thermal approach, primarily when the inks or contained drugs are susceptible to heat degradation. Furthermore, it is crucial that the material viscosity is below 20 mPa s<sup>31</sup>. On the other hand, SSE uses a pressurized air mechanism to extrude semi-solid material through a nozzle in a layer-by-layer process to build up 3D objects<sup>32</sup>. The main advantage is its ability to rapidly print viscous matrix at room temperature<sup>33</sup>, which is of great importance for thermolabile drugs and heat-sensitive components of formulations such as lipids.

Given the high viscosity and heat sensitivity of lipids, and to facilitate broader drug applicability, our study employs 3D-printing SSE technology to produce oral dosage forms containing a high percentage of pure lipids for the effective delivery of water-insoluble drugs through self-emulsification. Among the various bio-inspired materials, we selected lipid mesophases, a class of materials belonging to the lyotropic-liquid-crystal family, possessing a tuneable three-dimensional nanostructure along with mechanical (e.g., flexural strength and rigidity) and rheological properties of great interest for efficient material engineering for 3D printing. By altering the water content, temperature, or incorporating additives, we can tailor the lipid mesophase to exhibit lamellar ( $L_\alpha$ ), cubic (Q), and reverse hexagonal ( $H_{II}$ ) geometries<sup>34</sup>. Each phase geometry has an impact on drugs release rates, viscosity, and self-emulsification mechanisms. By exploring the nanostructure-property correlations, lipid matrices with the desired material and self-emulsification properties were developed. While order-to-order phase transitions in lipid mesophase have been extensively investigated to achieve controlled drug release<sup>35-37</sup>, this is the first time, to our knowledge, that order-to-order phase transitions of lipid mesophases have been explored for pharmaceutical additive manufacturing.

To achieve our objective, we selected a lipid mixture, S80, enriched with polyenylphosphatidylcholines(PPC) at a concentration greater than 75%. We selected this mixture for its dual activity as an excipient, to improve drug bioavailability, and for its

bioactivity in deactivating profibrogenic hepatic stellate cells, which are the main collagen-producing cells in hepatic fibrogenesis<sup>38</sup>.

Nonetheless, pure lipids are unsuitable for 3D printing due to their natural waxy, soft, and brittle nature. Therefore, we chose to blend S80 with tocopherol based on its demonstrated capacity to promote transition to  $H_{II}$ <sup>39-41</sup>, typically characterized by a high viscosity system<sup>42,43</sup> as well as its well-known antioxidant properties that prevent lipid peroxidation<sup>44</sup>. Previous research suggests that formulating obeticholic acid (OA) with PPC-based dosage forms could potentially enhance its clinical success. Therefore, we specifically selected OA to assess the solubility capacity<sup>45</sup>. This highly lipophilic compound ( $\log P = 5.7$ ) is a Biopharmaceutical Classification System Class II drug (poorly soluble and highly permeable). OA has demonstrated potential in reducing liver fibrosis markers such as  $\alpha$ -smooth muscle actin ( $\alpha$ SMA) and collagen (coll1a1) in rodent models of fibrosis and cirrhosis<sup>46,47</sup>, and it is currently undergoing phase 3 clinical trials for the treatment of NASH-related hepatic fibrosis<sup>48-52</sup>.

Our approach has led to (1) the design and additive manufacturing of lipid mesophase containing high content of pure lipid; (2) the incorporation of the water-insoluble OA into the printable lipidic mesophase at a dose comparable to the marketed one; (3) the production of uniform 3D-printed tablets (printlets) using semi-solid extrusion at room temperature; (4) the disintegration of the printlets in intestinal fluids through self-emulsification and (5) the increase in the solubility of the embedded drug in the selected intestinal fluids. Our printlets with OA (OA-printlets) may offer unique opportunities for the treatment of chronic liver disease, as well as serve as a potential platform for the printing of other water-insoluble drugs for oral delivery.

## 2. Materials and methods

### *Materials*

Soybean phospholipid with 75% polyenylphosphatidylcholines (S80) was a kind gift from Lipoid GmbH (Ludwigshafen, Germany).  $\alpha$ -Tocopherol (Ph. Eur. Quality) was purchased from Sigma-Aldrich (St. Louis, MO, USA). Obeticholic acid was purchased from abcr GmbH (Karlsruhe, Germany). Fasted and fed state simulated fluid were purchased from Biorelevant (London, UK). Phosphate buffer saline was purchased from Carl Roth (Karlsruhe, Germany). All organic solvents (methanol, acetonitrile, and tetrahydrofuran (THF)) were obtained from

Fisher Scientific (Schwerte, Germany). All chemicals were used as received. Ultrapure water of resistivity 18.2 M $\Omega$ .cm was produced by a Barnstead Smart2 pure device from Thermo Scientific (Pittsburgh, USA). Relevant chemical structures are given in **Figure 1**.

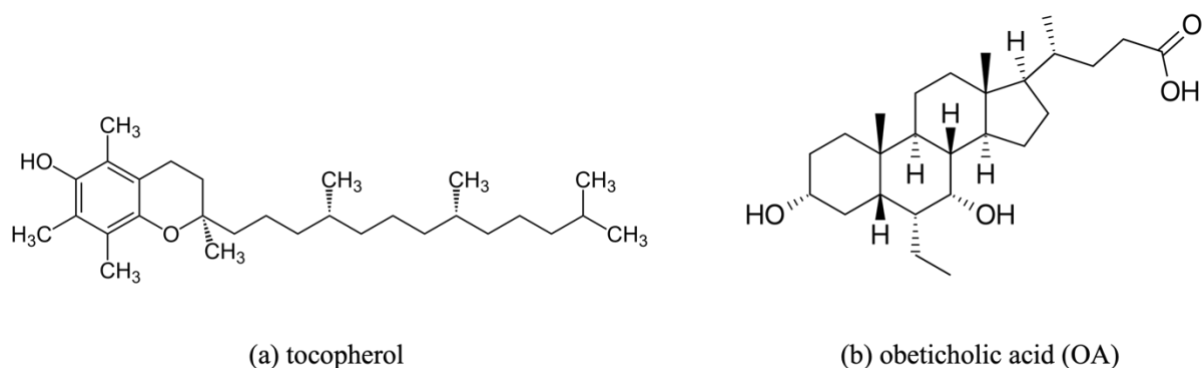


**Figure 1:** Chemical structure of (a) tocopherol and (b) obeticholic acid used in this study.

#### *Preparation of lipid mesophase ink and OA-lipid mesophase ink*

For the preparation of the lipid mesophase ink, S80 (68% w/w) and tocopherol (12% w/w) were co-dissolved in methanol (MeOH) into a glass vial. MeOH was removed and the dried lipid mixture was mixed with weighed amounts of water (20% w/w). The mixture was centrifuged for 10 min at 5000 g and manually mixed with a spatula several times. The procedure was repeated until a uniform mixture was achieved. The lipid mesophase was left to equilibrate for 24 h in the dark at room temperature. For lipid mesophase containing the drug (OA-lipid mesophase ink), OA was added at a concentration of 2.5% w/w and dissolved with the lipid mixture. The subsequent steps followed the same procedure as outlined above. A schematic representation of the preparation process of lipid mesophases is shown in **Figure 2**.

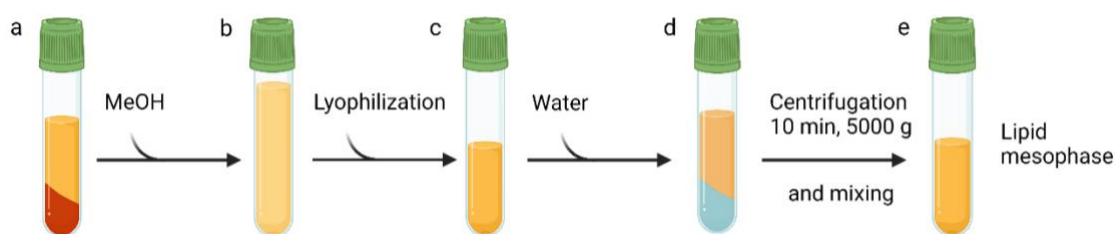


**Figure 2:** Schematic representation of the preparation of lipid mesophases. (a) S80 and tocopherol are placed into a glass vial. (b) MeOH is added to dissolve the components. (c) The vial undergoes freeze-drying to remove all the solvent. (d) A weighed amount of water is added to the mixture. (e) Centrifugation and mixing are repeated until the mixture becomes uniform.

### *Small angle X-ray*

SAXS experiments were conducted to determine the phase identity and symmetry of both printable lipid mesophase and OA-printable lipid mesophase. The measurements were carried out using a Bruker AXS Micro with a micro-focused X-ray source. The voltage and filament current were set to 50 kV and 1000  $\mu\text{A}$ , respectively. The 2D Kratky collimator was used to collimate the Cu K $\alpha$  radiation ( $\lambda_{\text{Cu K}\alpha} = 1.5418 \text{ \AA}$ ), and the data were collected by a 2D Pilatus 100K detector. The scattering vector Q, which is determined by the scattering angle  $2\theta$  and the wavelength  $\lambda$ , was calibrated using silver behenate. The data were collected and azimuthally averaged using the Saxsgui software to generate a 1D intensity vs. scattering vector Q plot, with a Q range of 0.001 to 0.5  $\text{\AA}^{-1}$ . The samples were placed inside a stainless-steel cell between two thin replaceable mica sheets and sealed with an O-ring. The measurements were performed at 25 °C, and the samples were equilibrated for 10 min before measurements were taken. The scattered intensity was collected over a period of 30 min.

### *Design and 3D printing of lipid mesophase ink*

The design of the printlets was created using the Netfabb<sup>®</sup> software (Autodesk, USA). A Bio-X (Celink, Sweden) bioprinter with a pneumatic thermoplastic printhead was used for 3D printing the tablets. To ensure optimal results, approximately 3 g of each formulation was placed into the pneumatic syringe and then centrifuged at 4430 g for 15 min to remove any air bubbles. Starting from a previous study<sup>53</sup>, a formulation screening was performed to evaluate the extruded shape for both printability and shape retention (in the Appendix, **Table A3.1 and A3.2**). The result of this screening process led to the identification of the best formulation. The following printing parameters were used: a pressure of 65 kPa; a print speed of 5 mm/s; and a nozzle diameter of 27G. The temperature was set to 25 °C, and the infill density was chosen as 13%, 25%, and 35% with a honeycomb pattern. After 3D printing, the manufactured tablets were allowed to dry at room temperature for 24 h, after which they were weighed, and their dimensions were measured using a manual caliper.

### *Drug load and drug distribution*

To assess the homogeneity of drug distribution within the tablet matrix, a random selection of three OA-printlets at all infill densities was taken, and each tablet was divided into three sections. Each section was then dissolved in MeOH, and drug concentration was analyzed using high-performance liquid chromatography (HPLC; Ultimate 3000, Thermo Fisher Scientific, Switzerland) equipped with a charged aerosol detector (CAD; Corona Veo RS, Thermo Fisher).

A Hypersil Gold™ (C18, 150 x 2.1 mm; Thermo Fisher Scientific) with a particle size of 1.9 µm and a pore size of 175 Å and was used at a temperature of 30 °C. The injection volume was 5 µL and the flow rate was set at 0.5 mL min<sup>-1</sup>. The method used was isocratic and consisted of three eluents, eluent A: methanol + 0.05% v/v TFA, eluent B: acetonitrile + 0.05% v/v TFA and eluent C: ultrapure water + 0.05% v/v TFA. The analysis used 35% of eluent A, 55% of eluent B, and 10% of eluent C for 10 min. Therefore, all sections were analyzed and normalized based on a 10 mg weight. In contrast, to assess the equivalence of the total drug content between OA-printlets with an infill density of 35% and the theoretical value – which corresponds to the marketed tablets (5 mg) – tablets were individually dissolved in 10 mL MeOH, and the drug concentration was quantified using HPLC-CAD as described above. Data was collected and analyzed using the software Chromeleon (Version 7, Thermo Fisher).

#### *Rheological characterization*

The rheological characteristics of the printable lipid mesophase, as well as the printlets and OA-printlets of various infill densities (13%, 25%, and 35%), were investigated using a Modular Compact Rheometer MCR 72 (Anton Paar, Graz, Austria) equipped with a cone-plate geometry, diameter=49.942 mm and cone angle=0.993°. The temperature was kept at 25 °C and the linear viscoelastic region (LVR) was determined by conducting an amplitude sweep at 1 Hz between 0.01 and 100% strain. After, a frequency sweep was performed at a constant strain within the linear viscoelastic region between 0.1 and 100 rad/s at 25 °C.

#### *Assessment of self-emulsification and particle size determination*

The self-emulsification properties of printlets were evaluated using an experimental setup that consisted of a 50 mL tube and a custom-made metallic basket<sup>54</sup> (in the Appendix, A3.2). The evaluation was conducted in three different media: phosphate buffer saline (PBS), fasted state simulated intestinal fluid (FaSSIF), and fed state simulated intestinal fluid (FeSSIF) to determine the disintegration of the tablets in intestinal fluids. To this end, printlets at various infill densities (13%, 25% and 35%) were placed in 20 mL of the selected dissolution media and gently agitated using a shaker at 200 rpm, at a temperature of 37 °C for 2 h. The process of self-emulsification was visually assessed to examine the appearance of the resulting emulsions. After the self-emulsification assessment, aliquots of the bulk media were collected and analysed using dynamic light scattering (DLS). The mean hydrodynamic diameter was determined using Litesizer 500 (Anton Paar, Graz, Austria) at a temperature of 25 °C and a backscatter angle of 175° and a 658 nm laser. The number of measurements was 6 while a



refractive index of 1.3304 and a viscosity of 0.89 mPa/s were set for the solvent. The sample was analyzed without additional dilution.

#### *Transmission electron cryomicroscopy (Cryo-TEM)*

A printlet with an infill density of 35% was subjected to the aforementioned three different media, namely PBS, FaSSIF, and FeSSIF, for a duration of 2 h. The resulting media was subsequently diluted to a concentration of 0.5 mg/mL of S80 and analyzed using Cryo-TEM. A volume of 4  $\mu$ L of each sample was deposited on lacey carbon films (Cu 200 mesh grid, Agar Scientific, UK) and then plunge-frozen with Vitrobot (FEI, USA). The blotting chamber conditions were set to 4 °C, 100% humidity, and 4 s blot time. Excess liquid was blotted automatically between two strips of filter paper. Grids were stored in liquid nitrogen until TEM observation. Low-dose electron diffraction was performed on an FEI Tecnai Spirit F20 electron microscope (FEI, USA). and imaged on a FEI Titan Krios at 300kV equipped with a US4000 CCD detector.

#### *Equilibrium solubility measurements*

The following method was adapted from a previous study<sup>55</sup>. OA solubility was carried out in the following media: PBS, FaSSIF, and FeSSIF. The impact of the formulation on the drug solubility was assessed by using the experimental setup both with and without the formulation. Free OA (10 mg) or the correspondent amount of formulation containing 10 mg of OA was added to 5 mL of the dissolution medium in glass vials. The vials were incubated at 37 °C for 24 h at 200 rpm, after which 1 mL was transferred in an Eppendorf tube and centrifuged for 10 min at 6800 g. The supernatant was lyophilized and diluted to an appropriate concentration for HPLC analysis to determine the drug concentration.

#### *Statistical analysis*

For all performed experiments, the obtained data are presented as mean  $\pm$  standard deviation and were replicated at least three times.

### 3. Results and discussion

#### *Lipid mesophase ink development*

To achieve successful semi-solid 3D printing using lipid mesophases at room temperature, a careful balance between ink composition, printing parameters, and shape retention is crucial.

For a material to be printable, it must exhibit sufficient resistance to deformation to flow through a nozzle and display adequate adhesion to both the build platform and previous layers. At the same time, the material must demonstrate a level of rigidity sufficient to retain its desired shape and support its weight without breaking or collapsing. In the case of pure lipids, which possess a waxy and naturally soft and brittle nature, they result unsuitable as printing material<sup>56</sup>.

To enhance the printability of the S80 lipid mixture, a second component was added, water. However, the screening of the binary system S80-water failed to meet the necessary criteria for printability and shape retention (data not shown). A ternary system was thus employed to optimize the ink's mechanical properties. Among the various additives used in lipid mesophase engineering, tocopherol was selected for being a potent lipid-soluble antioxidant<sup>57</sup> able to act as a stiffener of lipid chains<sup>53</sup> and induce phase transition to hexagonal phase<sup>41</sup>, associated with rheological properties relevant for the design of printable ink<sup>42,43</sup>. Starting with a non-printable lipid mesophase containing tocopherol (35% w/w) and developed by Martiel *et al.*<sup>53</sup>, a screening process was performed varying one parameter at a time, either the water or tocopherol content, to evaluate their printability and shape retention as key criteria for selection (in the Appendix, **Table A3.1 and A3.2**). Results showed that gradual increases in water content with constant tocopherol and lipid content led to inadequate printability. In contrast, increasing tocopherol content with constant lipid and water content resulted in a significant improvement in printability. The optimal composition of the ink was found to be 64% w/w S80, 12% w/w tocopherol, and 20% w/w water (lipid mesophase ink), which exhibited the best printability and shape retention qualities, both of which are crucial for high-quality printing. This composition (**Table 1**) was further loaded with OA at a concentration of 2.5% w/w (OA-lipid mesophase ink), a drug concentration chosen based on commercially available tablets to ensure comparability<sup>58</sup>.

**Table 1:** Composition of the printable lipid mesophase ink used for both printlet and OA-printlet.

<b>Surfactant</b>	<b>Oil</b>	<b><math>\alpha</math> oil</b>	<b>Water content (wt.%)</b>
<b>S80</b>	Tocopherol	12	20

## SAXS

To evaluate the influence of tocopherol on the phase identity of the binary system S80-water, the lipid mesophase inks were analysed with SAXS. A SAXS profile was obtained for both the lipid mesophase ink and OA-lipid mesophase ink, as depicted in **Figure 3**. The sequence of Bragg reflections identifies the long-range order, thus the symmetry of the lipid mesophase studied. The analysis revealed that the lamellar phase ( $L_\alpha$ ) coexists with the inverse hexagonal ( $H_{II}$ ) phase at room temperature, as evidenced by the observations of Bragg reflections at relative positions of 1:2:3:4 and  $\sqrt{1}:\sqrt{3}:\sqrt{4}$ , respectively. Additionally, the incorporation of 2.5% w/w of OA into the formulation did not result in any notable phase transition, as determined by the SAXS analysis. Previous studies have shown that amphiphiles with a single alkyl chain and critical packing parameter ( $CPP$ )  $\geq 1$ , such as tocopherol, can induce a phase transition towards the more negatively curved  $H_{II}$  phase due to their relatively small headgroup compared to the alkyl chain volume and  $CPP \geq 1$ , with a shorter amphiphile length than the phase forming lipid<sup>59</sup>. For example, in binary systems such as phytantriol-water<sup>39</sup> and glycerol monooleate-water<sup>40</sup>, the addition of tocopherol acetate has been observed to lead to a reorganization of the geometry to  $H_{II}$  phase. In the case of Dimodan U/J-tocopherol acetate-water, a complete phase diagram is available in literature<sup>41</sup>, where a low vitamin content (less than 5%) can result in a wide variety of mesophases. Increasing the water content while keeping the lipid and tocopherol percentage constant can lead to a direct transition from  $L_\alpha$  to  $H_{II}$  phase. Martiel et al.<sup>53</sup> have also reported on the formation of  $H_{II}$  phase in a ternary system composed of soybean phosphatidylcholine-tocopherol-water at a composition of 45-35-20%. Since the lipid mesophase ink under investigation is based on a mixture of PPC-rich (>75%) lipid, it is reasonable to hypothesize that the addition of tocopherol could similarly induce direct formation of  $H_{II}$  phase, as observed in previous studies. Therefore, the observed coexistence of  $L_\alpha$  and  $H_{II}$  phase in our lipid mesophase ink can be explained by a not fully complete phase transition, possibly due to the multiple lipidic components of the ink mesophase.

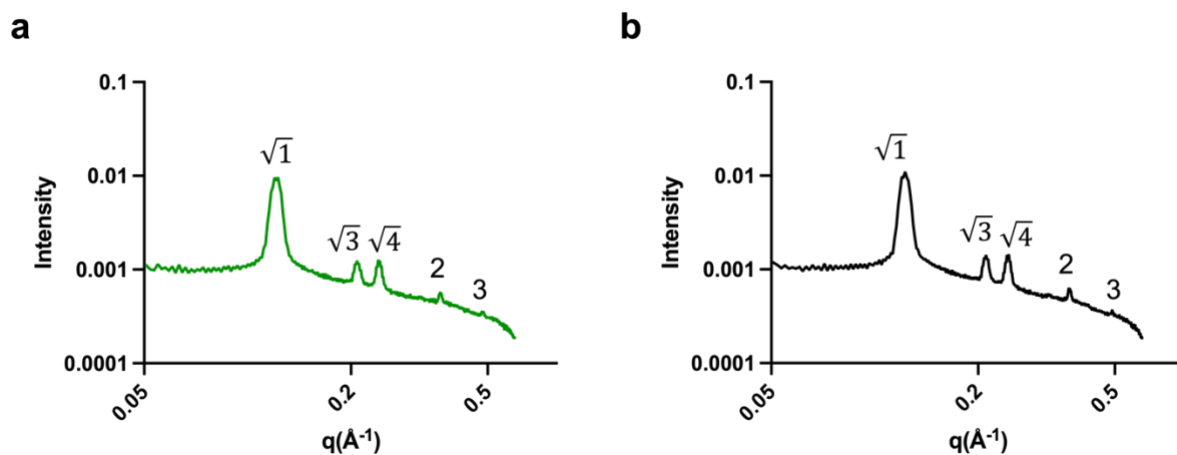


**Figure 3:** SAXS patterns of the (a) lipid mesophase ink and (b) OA-lipid mesophase ink.

### *3D printing and quality of the printlets and OA-printlets*

The formulation was extruded through a 27G nozzle, producing oval tablets utilizing a honeycomb geometry, as depicted in **Figure 4**. The end product was yellow-coloured tablets, due to the presence of the S80 lipid mixture, and no solidification or dripping was observed during the printing process. Moreover, the honeycomb geometry was modified by controlling the infill densities (13%, 25%, and 35%), and hence surface area, to enable for example dose personalization without the need to alter the formulation. While the printing process did not achieve a high level of precision, as evidenced by the presence of small lines on the surface of the tablets when a 35% infill density was used, this can be attributed to the low-resolution nozzle diameter as smaller nozzle diameter are convenient for producing higher resolution objects<sup>60</sup>. Thus, the observed lines are likely due to the limitations of the printing equipment and the trade-offs between printing resolution and speed. Upon drying at room temperature, the printlets displayed suitable mechanical properties (e.g., flexural strength and rigidity) for handling without the risk of breaking or deformation. However, we believe that using a vacuum dryer would improve their upscale production.

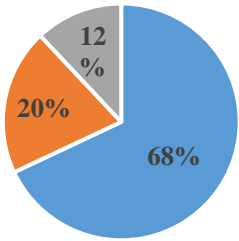


**Figure 4:** Samples of printlets of different infill densities.

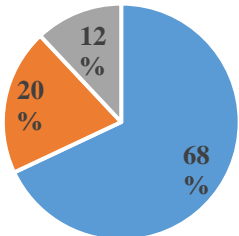
After the production of the printlets, we incorporated the drug OA (OA-printlets). As shown in **Table 2** and **Table 3**, printing parameters of pressure (65 kPa), speed (mm/sec) and nozzle (27G) are identical to the printing parameters used for the manufacturing of printlets, thus the presence of the drug did not negatively impact the printing process. In conclusion, these results demonstrated the feasibility of producing printlets from lipid mesophases and loading drugs using a semi-solid extrusion 3D printer at room temperature, making it suitable for thermolabile drug compounds.

After printing, the physical parameters of the printlets and OA-printlets tablets were evaluated and recorded in **Table 2** and **Table 3**. Printlets were printed with a constant value of pressure (65 kPa) and speed (5 mm/sec) and a fixed nozzle diameter (27G). Furthermore, we observed a 2-fold increase in weight for printlets from an infill density 13% to 35%. Furthermore, comparing the weight of printlets and OA-printlets, we observed comparable weights. The results of this study demonstrated the successful implementation of a semi-solid 3D-printing process to manufacture tablets of different infill densities. The data provide evidence of the reproducibility of the extrusion-based 3D printing process.

**Table 2:** Composition of printlets (blue, S80; orange, water; grey, tocopherol), and physical parameters of the manufactured printlets at various infill densities. The results are analysed by calculating the mean value of the physical dimensions  $\pm$  standard deviation (n = 6).

Composition (% w/w) of printlets	Pressure (kPa)	Speed (mm/s)	Nozzle (G)	Infill density	Length (mm)	Width (mm)	Height (mm)	Weight (g)
	65 kPa	5 mm/sec	27G	13%	11.24 $\pm$ 0.10	5.46 $\pm$ 0.05	2.22 $\pm$ 0.43	0.12 $\pm$ 0.002
	65 kPa	5 mm/sec	27G	25%	11.46 $\pm$ 0.32	5.68 $\pm$ 0.12	2.42 $\pm$ 0.21	0.17 $\pm$ 0.01
	65 kPa	5 mm/sec	27G	35%	11.61 $\pm$ 0.27	6.13 $\pm$ 0.25	2.08 $\pm$ 0.39	0.20 $\pm$ 0.01

**Table 3:** Composition of OA-printlets (blue, S80; orange, water; grey, tocopherol), and physical parameters of the manufactured OA-printlets at various infill densities. The results are analysed by calculating the mean value of the physical dimensions  $\pm$  standard deviation ( $n = 3$ ).

Composition (% w/w) of OA-printlets	Pressure (kPa)	Speed (mm/s)	Nozzle (G)	Infill density	Length (mm)	Width (mm)	Height (mm)	Weight (g)
	65 kPa	5 mm/sec	27G	13%	11.15 $\pm$ 0.19	5.78 $\pm$ 0.05	2.20 $\pm$ 0.23	0.11 $\pm$ 0.002
	65 kPa	5 mm/sec	27G	25%	11.33 $\pm$ 0.22	5.68 $\pm$ 0.10	2.40 $\pm$ 0.21	0.16 $\pm$ 0.01
	65 kPa	5 mm/sec	27G	35%	11.51 $\pm$ 0.17	6.11 $\pm$ 0.20	2.07 $\pm$ 0.26	0.20 $\pm$ 0.01

Drug distribution within the OA-printlets of various infill densities was carried out to assess their homogeneity. The results depicted in **Figure 5a** demonstrate a consistent and uniform drug distribution throughout the tablets, which highlights the potential of 3D-printing lipid mesophases as a method for producing high-dose tablets with accuracy. The consistent drug loading during printing process precluded any settling or aggregation of the drug in the printer cartridge. Additionally, the OA-printlets were formulated at a concentration of 2.5% w/w. This dose is comparable to commercially available tablets at an infill density of 35%. Therefore, a systematic evaluation of the total drug content of OA-printlets at the infill density 35% was performed and the results, as depicted in **Figure 5b**, indicated a strong correlation between the measured drug content and the theoretical drug loading in the final OA-printlets.

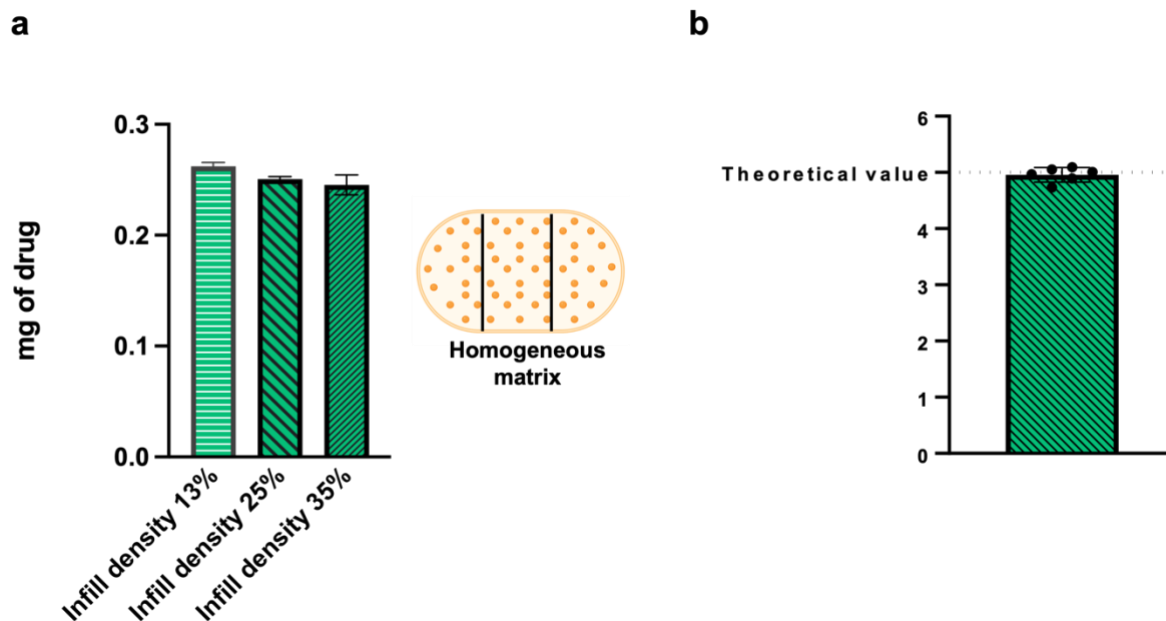


**Figure 5:** (a) Mass of drug (expressed in mg and constant weight=10 mg) from three different tablets with a representation of an example of a homogeneous matrix; (b) drug content of OA-printlets with infill density 35% in comparison with the theoretical value of drug.

### Rheology

To investigate the impact of printing and drying on the viscoelastic properties of the mesophase, as well as the structural strength and deformations during the disintegration of the printlets at different infill densities, we conducted amplitude sweep measurements on lipid mesophase ink prior to and following the manufacturing of printlets at various infill densities. In this test, the strain is gradually increased while the frequency is held constant at 1 Hz and at  $T = 25^\circ$ , **Figure 6**). Firstly, the results of the analysis showed that all the samples displayed a solid-like structure, with storage modulus ( $G'$ , the elastic component of the complex modulus  $G^*$ ) greater than the loss modulus ( $G''$ , the dissipative component of  $G^*$ ) in all measurements, indicating that they are viscoelastic solid materials. The  $G''$  describes the energy loss due to internal friction during shearing, and the results showed that the material remained intact, and no micro cracks developed before the limit of the LVE was reached.

The flow point (**Figure 6a and 6b**), together with the  $G'$  value in the LVR range, serves as an appropriate parameter for assessing the structural strength of materials. The flow point is closely related to the required force to be applied on the sample to induce flow and corresponds to the transition from predominantly elastic to mainly viscous behavior. Evaluation is achieved through the intersection point of  $G'$  and  $G''$  versus shear stress. At this point, the inner structure becomes irreversibly destroyed, leading to flow. Our observations indicate that the lipid

mesophase ink has a lower yield point and  $G'$  prior to printing, indicating lower structural strength, which is crucial for achieving optimal flexural strength and rigidity to allow the material flow through the nozzle while maintaining shape after printing. Following the drying process, the flow point increases, along with the  $G'$  value in the LVR, indicating a higher structural strength, which may result in poor mechanical properties that are not suitable for 3D printing.

In all the materials (**Figure 6c, 6d, 6e, 6f**), the shape of  $G'$  and  $G''$  exhibit a sharp downturn at the limit of the LVR, above that a strain increase causes the disruption of the network, resulting in a decrease of both  $G'$  and  $G''$ . This phenomenon was previously interpreted with a 'slip-plane' model<sup>61–63</sup>, which suggests that large deformations occur along certain planes in the structure while maintaining relatively small deformations elsewhere. Therefore, the elasticity that emerges before the LVE is linear, and the material behaves as a viscoelastic solid. Above the limit, slip exists, leading to brittle fracturing behaviour and suggesting that the formulation breaks into large pieces, rather than breaking homogeneously. Indeed, the material formed a consistent three-dimensional network throughout the non-destructive deformation range and broke into larger pieces once the limit was reached.

To gather additional insight into the flow behaviour and topology of the mesophase, we investigated the dependence of the storage and loss modulus of the material on the frequency of the applied shear perturbation, by performing a frequency sweep in the LVR (in the Appendix, **A3.3**). The results showed that  $G'$  dominated over  $G''$  without crossover in the frequency range (0.1-100 rad/s), which indicated strong stability of the material over time. These results provide informative insights into the rheological behaviour of the viscoelastic material and can be used for further studies and applications.



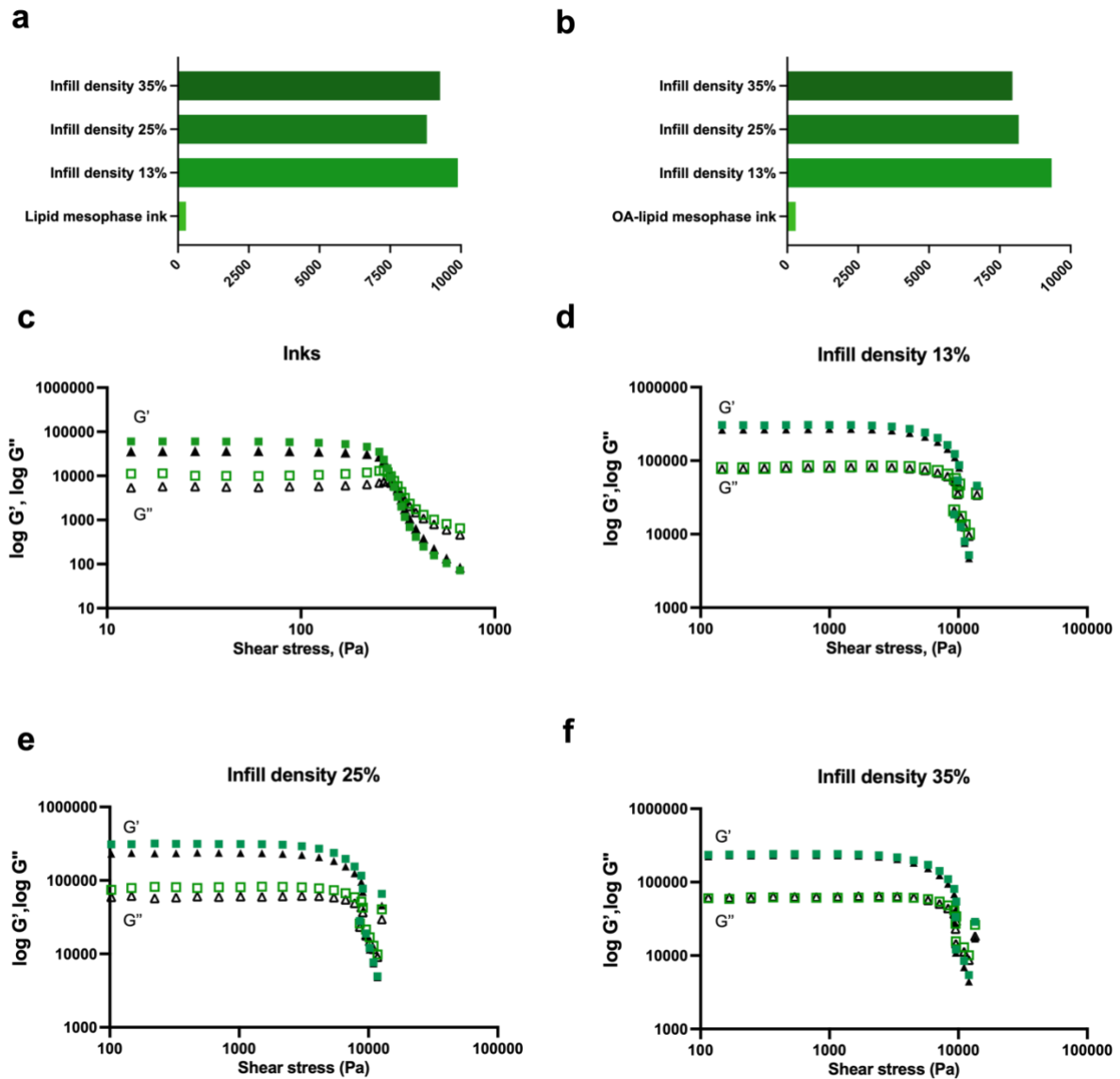


**Figure 6:** Flow points of (a) lipid mesophase ink and printlets at different infill densities and (b) OA-lipid mesophase ink and OA-printlets at different infill densities. Amplitude sweep measurements of (c) lipid mesophase (green) and OA-lipid mesophase ink (black); (d) printlet (green) and OA-printlet (black) at infill density 13%; (e) printlet (green) and OA-printlet (black) at infill density 25% and (b) printlet (green) and OA-printlet at infill density 35%. Storage modulus ( $G'$ - filled symbols) and loss modulus ( $G''$ - empty symbols) are shown at 25°C.

### *Assessment of self-emulsification*

Lipid-based formulations are generally employed to enhance the solubility of embedded drugs through the formation of colloidal structures. In the development of lipid mesophase ink, we sought to explore the self-emulsifying properties within the gastrointestinal tract. To this end the study aimed to assess the emulsification behavior of printlets upon exposure to simulated intestinal fluid, FaSSIF and FeSSIF, as well as plain buffer in the form of PBS. As shown in

the Appendix, **A3.4**, the tablets were fully emulsified within 2 h in all three media, with larger fragments observed only in the presence of plain buffer. In contrast, when the printlets were exposed to FaSSIF and FeSSIF, the resulting media was relatively homogeneous with few or no clumps. To gain further insight into the bulk structure of the diluted printlets, a dynamic light scattering (DLS) analysis was performed, revealing a highly polydisperse dispersion with multiple peaks in intensity (**Table 4, 5 and 6**). Therefore, to explore the morphological changes of the lipid mesophase ink that occurred during the emulsification process, Cryo-TEM images were captured (**Figure 7**). In PBS, the media was dominated by the presence of large colloids, along with lipid droplets. The presence of bile components in FaSSIF resulted in a polydisperse media containing micelles, vesicles, multilamellar vesicles, and lipid droplets of varying size and morphology. While Cryo-TEM imaging could not distinguish between mixed-micelles and small lipid droplets, the coexistence of large aggregates and ‘sponge-like’ unilamellar vesicles, where it is possible to observe ordered inner structures compatible with the hexagonal phase<sup>64</sup> while the outermost surface region displays lamellar features, was observed in FaSSIF. In agreement with a previous study<sup>65</sup>, FeSSIF showed a higher abundance of micelles and lipid droplets, potentially due to the presence of surfactants such as taurocholic acid and lecithin, along with pancreatin. This suggests the formation of mixed bile salts/phospholipid micelles with rare vesicles. In general, these results strongly suggest that the use of biorelevant media lowers the degree of structural order of the bulk printlets.

To further investigate the highly polydisperse nature of the printlets in contact with aqueous media, we performed additional experiments that combined SAXS with visual inspections. As previously described, our SAXS results revealed that the 3D-printed formulation consists of a combination of  $L_\alpha$  and  $H_{II}$  phases. The  $H_{II}$  (S80, 45% w/w; tocopherol, 12% w/w; water 20% w/w) phase was found to be completely water-insoluble in PBS, while the  $L_\alpha$  (S80, 80% w/w; water, 20% w/w) phase dissolved rapidly, reaching complete dissolution (in the Appendix, **A3.4**). Therefore, we hypothesized that the  $L_\alpha$  component of the ink acts as a disintegrant, facilitating the rapid disintegration of the tablet upon exposure to PBS, while the  $H_{II}$  component contributes to the formation of larger fragments. Further, to fully emulsify the printlets, we hypothesized that the larger fragments undergo a transition from inverse  $H_{II}$  to  $L_\alpha$  emulsified phase in the dispersed state, as already described in previous studies<sup>41,66</sup>. In the dispersed state, the larger  $H_{II}$  fragments are destabilized due to the interface with the media and the mechanism of particle stabilization leading to a higher free energy. This observation, together with possible degradation of the liquid crystalline matrix as a result of the lipid digestion in biorelevant

media, may explain why the  $H_{II}$  phase is more prone to destabilization when larger fragments are produced.

**Table 3.** Intensity peaks of printlets of different infill densities in FaSSIF.

<b>FaSSIF</b>	<b>Peak Intensity 1</b>	<b>Peak Intensity 2</b>	<b>Peak Intensity 3</b>
<b>Infill density 13%</b>	66 nm	233 nm	5738 nm
<b>Infill density 25%</b>	106 nm	457 nm	3552 nm
<b>Infill density 35%</b>	1,62 nm	259 nm	2882 nm

**Table 4.** Intensity peaks of printlets of different infill densities in FeSSIF.

<b>FeSSIF</b>	<b>Peak Intensity 1</b>	<b>Peak Intensity 2</b>	<b>Peak Intensity 3</b>
<b>Infill density 13%</b>	16 nm	181 nm	3794 nm
<b>Infill density 25%</b>	15 nm	70 nm	459 nm
<b>Infill density 35%</b>	11 nm	39 nm	/

**Table 5.** Intensity peaks of printlets of different infill densities in PBS.

<b>PBS</b>	<b>Peak Intensity 1</b>	<b>Peak Intensity 2</b>	<b>Peak Intensity 3</b>
<b>Infill density 13%</b>	122 nm	514 nm	14553 nm
<b>Infill density 25%</b>	165 nm	934 nm	7693 nm
<b>Infill density 35%</b>	125 nm	458 nm	8887

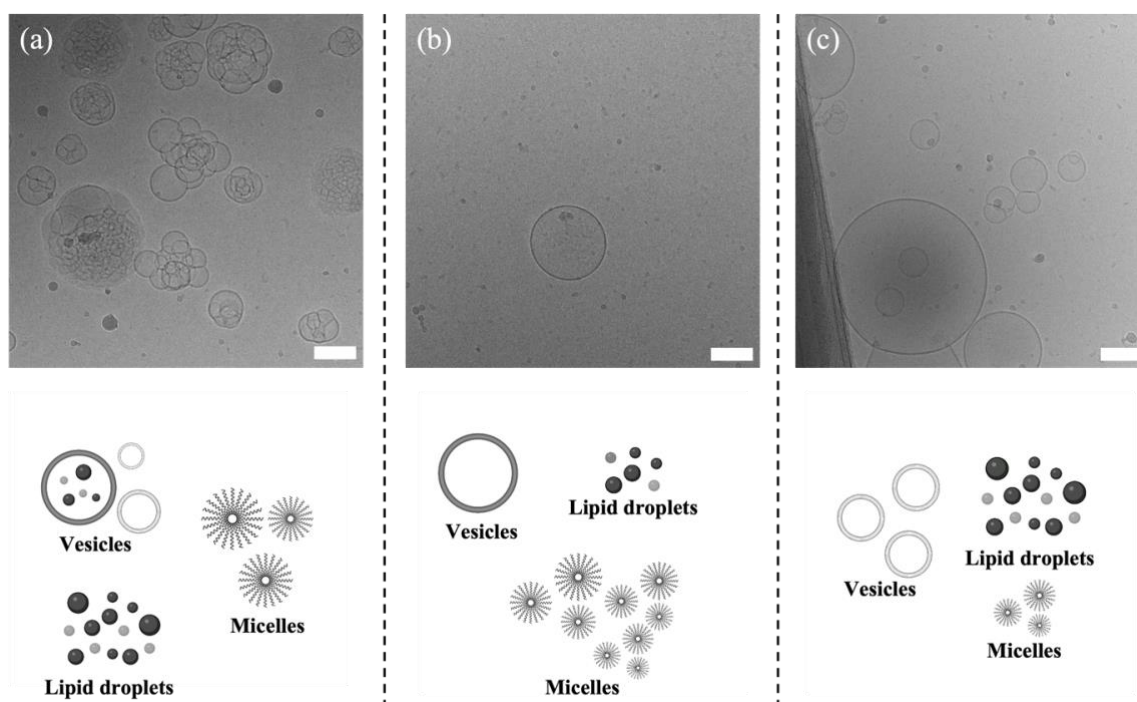


**Figure 7:** Cryo TEM images of printlets in (a) FaSSIF, (b) FeSSIF and (c) PBS after 2h of treatment. To facilitate identification of different colloidal structures, schematic representation of the images is in the figures below. The scale bar corresponds to 100 nm.

### *Equilibrium solubility assessment*

With the aim of determine the equilibrium solubility and the impact of the formulation on the solubility of the water-insoluble drug, we performed experiments to evaluate the solubility of free drug OA and OA-printlets in three different dissolution media: PBS, FaSSIF and FeSSIF. As showed in **Figure 8**, the complete solubilization of the drug was only achieved in the presence of the formulation in biorelevant media enriched with lecithin, taurocholate acid, and bile acids. This result can be explained by the incorporation of the bile acids into the formulation lipids to form a range of colloidal and liquid crystalline structures that help to reduce precipitation and maintain the drug in a solubilized state, as previously reported<sup>67,68</sup> In comparison with the formulation, a rise in the solubility is also observed in free OA when exposed to FaSSIF and FeSSIF, consistent with previous research<sup>69</sup>. On the other hand, the results revealed that the lowest solubility of free OA was observed in plain buffer, whereas the presence of the formulation did not significantly improve its solubility. A possible explanation for this is that <sup>69</sup>in aqueous environments, bile salts aggregate to form micelles, which, under physiological conditions, are transformed into mixed micelles with lecithin and glycerides.

These colloidal structures facilitate the solubilization of the drug, as previously reported in the literature<sup>70,71</sup>.

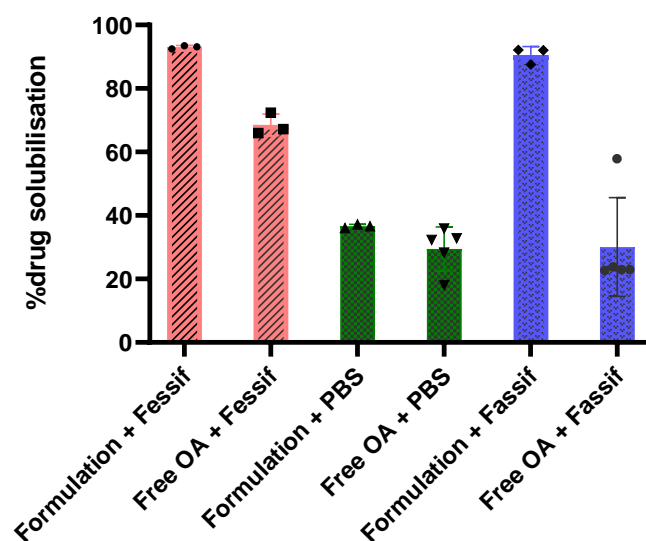


**Figure 8:** Equilibrium solubility of OA in different dissolution media.

In particular, the solubilization of OA in mixed micelles is likely attributed to two main interactions. Firstly, the hydrophobic interaction between the hydrophobic  $\beta$ -side of the steroid nucleus of the bile acids and the OA molecule. Secondly, a hydrogen bond between the carboxyl group of the bile acids and the OH group of the OA molecule.<sup>67,68</sup> In conclusion, our findings confirm the importance of considering the presence of bile acids in the design of oral dosage forms and highlight that, in these biorelevant conditions, our formulation can provide additional benefits in terms of drug solubilization, potentially via the formation of more stable mixed colloidal structures and increased number of interactions.

#### 4. Conclusions

In our study, we have successfully demonstrated the potential of lipid mesophases as a printable material suitable for semi solid extrusion at room temperature. By carefully controlling the ink composition, its rheology, and printing parameters, we were able to produce printlets with arbitrary infill densities and overall physical parameters. Our formulation is characterized by a high percentage of pure lipid with antifibrotic properties, rendering it an exceptional candidate for the delivery of water-insoluble drugs. Upon contact with intestinal fluids, the printlets

disintegrated within 2 h, forming colloidal structures that enhanced the solubility of the water-insoluble drug, OA. These results suggest that our printlets have potential for the treatment of liver fibrosis and can serve as a platform for printing other water-insoluble drugs for oral delivery. The use of additive manufacturing of lipid mesophases presents a new avenue for producing not only oral dosage forms but also other functional structures based on this material.

## 5. References

1. Porter, C. J. H., Trevaskis, N. L., Charman, W. N. Enterocyte Dissolution rate Lipids and lipid-based formulations: optimizing the oral delivery of lipophilic drugs. *Nat Rev Drug Discov* **6**, (2007).
2. Feeney, O. M., Crum, M. F., McEvoy, C. L., Trevaskis, N. L., Williams, H. D., Pouton, C. W., Charman, W. N., Bergström, C. A. S., Porter, C. J. H. 50 years of oral lipid-based formulations: Provenance, progress and future perspectives. *Adv Drug Deliv Rev* **101**, 167–194 (2016).
3. Porter, C. J. H., Charman, W. N. Intestinal lymphatic drug transport: An update. *Adv Drug Deliv Rev* **50**, 61–80 (2001).
4. Trevaskis, N. L., Charman, W. N., Porter, C. J. H. Lipid-based delivery systems and intestinal lymphatic drug transport: A mechanistic update. *Adv Drug Deliv Rev* **60**, 702–716 (2008).
5. Abdalla, A., Klein, S., Mäder, K. A new self-emulsifying drug delivery system (SEDDS) for poorly soluble drugs: Characterization, dissolution, in vitro digestion and incorporation into solid pellets. *Eur J Pharm Sci* **35**, 457–464 (2008).
6. Strickley, R. Currently Marketed Oral Lipid-Based Dosage Forms: Drug Products and Excipients. *Oral Lipid-Based Formulations*, CRC Press (2007).
7. Tang, T. O., Holmes, S., Boyd, B. J., Simon, G. P. Extrusion and 3D printing of novel lipid-polymer blends for oral drug applications. *Bio Adv* **137**, 212818 (2022).
8. Koch, N., Jennotte, O., Toussaint, C., Lechanteur, A., Evrard, B. Production challenges of tablets containing lipid excipients: Case study using cannabidiol as drug model. *Int J Pharm* **633**, 122639 (2023).
9. Sander, C., Holm, P. Porous magnesium aluminometasilicate tablets as carrier of a cyclosporine self-emulsifying formulation. *AAPS PharmSciTech* **10**, 1388–1395 (2009).
10. Gumaste, S. G., Dalrymple, D. M., Serajuddin, A. T. M. Development of solid SEDDS, V: Compaction and drug release properties of tablets prepared by adsorbing lipid-based formulations onto neusilin® US2. *Pharm Res* **30**, 3186–3199 (2013).
11. Bertoni, S., Albertini, B., Passerini, N. Different BCS Class II drug-gelucire solid dispersions prepared by spray congealing: evaluation of solid state properties and In Vitro Performances. *Pharmaceutics* **12**, 548 (2020).
12. Tracy, T., Wu, L., Liu, X., Cheng, S., Li, X. 3D printing: Innovative solutions for patients and pharmaceutical industry. *Int J Pharm* **631**, 122480 (2023).
13. Goyanes, A., Madla, C. M., Umerji, A., Duran Piñeiro, G., Giraldez Montero, J. M., Lamas Diaz, M. J., Gonzalez Barcia, M., Taherali, F., Sánchez-Pintos, P., Couce, M. L., Gaisford, S., Basit, A. W. Goyanes. Automated therapy preparation of isoleucine formulations using 3D printing for the treatment of MSUD: First single-centre, prospective, crossover study in patients. *Int J Pharm* **567**, 118497 (2019).
14. Yi, H. G., Choi, Y. J., Kang, K. S., Hong, J. M., Pati, R. G., Park, M. N., Shim, I. K., Lee, C. M., Kim, S. C., Cho, D. W. A 3D-printed local drug delivery patch for pancreatic cancer growth suppression. *Journal of Controlled Release* **238**, 231–241 (2016).
15. Seoane-Viaño, I., Ong, J. J., Luzardo-Álvarez, A., González-Barcia, M., Basit, A.W., Otero-Espinar, F. J., Goyanes, A. 3D printed tacrolimus suppositories for the treatment of ulcerative colitis. *Asian J Pharm Sci* **16**, 110–119 (2021).
16. Sandler, N., Preis, M. Printed Drug-Delivery Systems for Improved Patient Treatment. *Trends Pharmacol Sci* **37**, 1070–1080 (2016).
17. Khaled, S. A., Burley, J. C., Alexander, M. R., Yang, J., Roberts, C. J. 3D printing of five-in-one dose combination polypill with defined immediate and sustained release profiles. *J Control Release* **217**, 308–314 (2015).
18. Goh, W. J., Tan, S. X., Pastorin, G., Ho, P. C. L., Hu, J., Lim, S. H. 3D printing of four-in-one oral polypill with multiple release profiles for personalized delivery of caffeine and vitamin B analogues. *Int J Pharm* **598**, (2021).
19. Windolf, H., Chamberlain, R., Breitreutz, J., Quodbach, J. 3D Printed Mini-Floating-Polypill for Parkinson's Disease: Combination of Levodopa, Benserazide, and Pramipexole in Various Dosing for Personalized Therapy. *Pharmaceutics* **14**, 931 (2022).
20. Barber, B. W., Dumont, C., Caisse, P., Simon, G. P., Boyd, B. J. A 3D-printed polymer-lipid-hybrid tablet towards the development of bespoke SMEDDS formulations. *Pharmaceutics* **13**, 2107 (2021).
21. Zhang, B., Teoh, X. Y., Yan, J., Gleadall, A., Belton, P., Bibb, R., Qi, S. Development of combi-pills using the coupling of semi-solid syringe extrusion 3D printing with fused deposition modelling. *Int J Pharm* **625**, (2022).
22. Jeong, H. M., Weon, K.-Y., Shin, B. S., Shin, S. 3D-Printed Gastroretentive Sustained Release Drug Delivery System by Applying Design of Experiment Approach. *Molecules* **25**(10), 2330 (2020).
23. Charoenying, T., Patrojanasophon, P., Ngawhirunpat, T., Rojanarata, T., Akkaramongkolpor, P., Opanasopit P. Fabrication of floating capsule-in-3D-printed devices as gastro-retentive delivery systems of amoxicillin. *J Drug Deliv Sci Technol* **55**, (2020).
24. Melocchi, A., Ubaldi, M., Briatico-Vangosa, F., Moutaharrik, S., Cerea, M., Foppoli, A., Maroni, A., Palugan, L., Zema, L., Gazzaniga, A. The Chronotopic™ System for Pulsatile and Colonic Delivery of Active Molecules in the Era of Precision Medicine: Feasibility by 3D Printing via Fused Deposition Modeling (FDM). *Pharmaceutics* **13**, 759 (2021).
25. Haring, A. P., Tong, Y., Halper, J., Johnson, B. N. Programming of Multicomponent Temporal Release Profiles in 3D Printed Polypills via Core-Shell, Multilayer, and Gradient Concentration Profiles. *Adv Healthc Mater* **7**, 1800213 (2018).
26. Yang, Y., Wang, X., Lin, X., Xie, L., Ivo, R., Shen, J., Yang, G. A tunable extruded 3D printing platform using thermo-sensitive pastes. *Int J Pharm* **583**, 119360 (2020).
27. SPRITAM (levetiracetam) Tablets. <https://spritam.com> Accessed Mar. 13, 2023.
28. National Center for Biotechnology Information. PubChem Patent Summary for US-9669009-B2. <https://pubchem.ncbi.nlm.nih.gov/patent/US-9669009-B2>. Accessed Mar. 13, 2023.

29. Krueger, L., Miles, J. A., Popat, A. 3D printing hybrid materials using fused deposition modelling for solid oral dosage forms. *J Control Release* **351**, 444–455 (2022).
30. Cader, H. K., Rance, G. A., Alexander, M. R., Gonçalves, A. D., Roberts, C. J., Tuck, C. J., Wildman, R. D. Water-based 3D inkjet printing of an oral pharmaceutical dosage form. *Int J Pharm* **564**, 359–368 (2019).
31. de Gans, B. J., Duineveld, P. C., Schubert, U. S. Inkjet Printing of Polymers: State of the Art and Future Developments. *Adv Materials* (**16**), 203-213 (2004).
32. Firth, J., Basit, A. W., Gaisford, S. The role of semi-solid extrusion printing in clinical practice. *AAPS* **31**, 133–151 (2018).
33. Seoane-Viaño, I., Januskaite, P., Alvarez-Lorenzo, C., Basit, A. W., Goyanes, A. Semi-solid extrusion 3D printing in drug delivery and biomedicine: Personalised solutions for healthcare challenges. *J Control Release* **332**, 367–389 (2021).
34. Aleandri, S., Mezzenga, R. The physics of lipidic mesophase delivery systems. *Phys Today* **73**, 38 (2020).
35. Fong, W. K., Hanley, T., Boyd, B. J. Stimuli responsive liquid crystals provide ‘on-demand’ drug delivery in vitro and in vivo. *J Control Release* **135**, 218–226 (2009).
36. Lee, K. W. Y., Nguyen, T. H., Hanley, T., Boyd, B. J. Nanostructure of liquid crystalline matrix determines in vitro sustained release and in vivo oral absorption kinetics for hydrophilic model drugs. *Int J Pharm* **365**, 190–199 (2009).
37. Negrini, R., Mezzenga, R. pH-responsive lyotropic liquid crystals for controlled drug delivery. *Langmuir* **27**, 5296–5303 (2011).
38. Valentino, G., Zivko, C., Weber, F., Brülisauer, L., Luciani, P. Synergy of Phospholipid–Drug Formulations Significantly Deactivates Profibrogenic Human Hepatic Stellate Cells. *Pharmaceutics* **11**, 676 (2019).
39. Dong, Y. Da, Larson, I., Hanley, T., Boyd, B. J. Bulk and dispersed aqueous phase behavior of phytantriol: Effect of vitamin E acetate and F127 polymer on liquid crystal nanostructure. *Langmuir* **22**, 9512–9518 (2006).
40. Bitan-Cherbakovsky, L., Yuli-Amar, I., Aserin, A., Garti, N. Structural rearrangements and interaction within H(II) mesophase induced by cosolubilization of vitamin E and ascorbic acid. *Langmuir* **25**, 13106–13113 (2009).
41. Sagalowicz, L., Guillot, S., Acquistapace, S., Schmitt, B., Maurer, M., Yagmur, A., de Campo, L., Rouvet, M., Leser, M., Glatter, O. Influence of vitamin E acetate and other lipids on the behavior of metaphases based on unsaturated. *Langmuir* **29**, 8222–8232 (2013).
42. Mezzenga, R., Meyer, C., Servais, C., Romoscanu, A. I., Sagalowicz, L., Hayward, R. C. Shear Rheology of Lyotropic Liquid Crystals: A Case Study. *Langmuir* **21**, 3322–3333 (2005).
43. Montalvo, G., Valiente, M., Rodenas, E. Rheological Properties of the L Phase and the Hexagonal, Lamellar, and Cubic Liquid Crystals of the CTAB/Benzyl Alcohol/Water System. *Langmuir* **12**, 5202–5208 (1996).
44. Bandarra, N. M., Campos, R. M., Batista, I., Nunes, M. L., Empis, J. M. Antioxidant synergy of  $\alpha$ -tocopherol and phospholipids. *J Amer Oil Chem Soc* **76**, 905–913 (1999).
45. Smith, S. M., Pegram, A. H. Obeticholic Acid: A Farnesoid X Receptor Agonist for Primary Biliary Cholangitis. *J Pharm Technol* **33**(2), 66-71 (2017).
46. Verbeke, L., Mannaerts, I., Schierwagen, R., Govaere, O., Klein, S., Vander Elst, I., Windmolders, P., Farre, R., Wenes, M., Mazzone, M., Nevens, F., van Grunsven, L. A., Trebicka, J., Laleman, W. FXR agonist obeticholic acid reduces hepatic inflammation and fibrosis in a rat model of toxic cirrhosis. *Sci Rep* **6**, 33453 (2016).
47. Fan, Y. Y., Ding, W., Zhang, C., Fu, L., Xu, D. X., Chen, X. Obeticholic acid prevents carbon tetrachloride-induced liver fibrosis through interaction between farnesoid X receptor and Smad3. *Int Immunopharmacol* **77**, 105911 (2019).
48. Younossi, Z. M., Ratziu, V., Loomba, R., Rinella, M., Anstee, Q. M., Goodman, Z., Bedossa, P., Geier, A., Beckebaum, S., Newsome, P. N., Sheridan, D., Sheikh, M. Y., Trotter, J., Knapple, W., et al. on the behalf of the REGENERATE study investigators. Obeticholic acid for the treatment of non-alcoholic steatohepatitis: interim analysis from a multicentre, randomized, placebo-controlled phase 3 trial. *The Lancet* **394**, 2184–2196 (2019).
49. Rinella, M. E., Dufour, J. F., Anstee, Q. M., Goodman, Z., Younossi, Z., Harrison, S. A., Loomba, R., Sanyal, A. J., Bonacci, M., Trylesinski, A., Natha, M., Shringarpure, R., Granston, T., Venugopal, A., Ratziu, V. Non-invasive evaluation of response to obeticholic acid in patients with NASH: Results from the REGENERATE study. *J Hepatol* **76**, 536–548 (2022).
50. Younossi, Z. M., Stepanova, M., Nader, F., Loomba, R., Anstee, Q. M., Ratziu, V., Harrison, S., Sanyal, A. J., Schattenberg, J. M., Barritt, A. S., Noureddin, M., Bonacci, M., Cawkwell, G., Wong, B., Rinella, M. Obeticholic Acid Impact on Quality of Life in Patients With Nonalcoholic Steatohepatitis: REGENERATE 18-Month Interim Analysis. *Clin Gastroenterol Hepatol* **20**, 2050–2058 (2022).
51. Ratziu, V., Sanyal, A. J., Loomba, R., Rinella, M., Harrison, S., Anstee, Q. M., Goodman, Z., Bedossa, P., MacConell, L., Shringarpure, R., Shah, A., Younossi, Z. REGENERATE: Design of a pivotal, randomised, phase 3 study evaluating the safety and efficacy of obeticholic acid in patients with fibrosis due to nonalcoholic steatohepatitis. *Contemp Clin Trials* **84**, 105803 (2019).
52. Randomized Global Phase 3 Study to Evaluate the Impact on NASH With Fibrosis of Obeticholic Acid Treatment. *ClinicalTrials.gov*. <https://clinicaltrials.gov/ct2/show/NCT02548351>.
53. Martiel, I., Baumann, N., Vallooran, J. J., Bergfreund, J., Sagalowicz, L., Mezzenga, R. Oil and drug control the release rate from lyotropic liquid crystals. *J Control Release* **204**, 78–84 (2015).
54. Karfeld-Sulzer, L. S., Ghayor, C., Siegenthaler, B., de Wild, M., Leroux, J. C., Weber, F. E. N-methyl pyrrolidone/bone morphogenetic protein-2 double delivery with in situ forming implants. *J Control Release* **203**, 181–188 (2015).
55. Abdalla, A., Klein, S., Mäder, K. A new self-emulsifying drug delivery system (SEDDS) for poorly soluble drugs: Characterization, dissolution, in vitro digestion and incorporation into solid pellets. *Eur J Pharm Sci* **35**, 457–464 (2008).
56. Tang, T. O., Holmes, S., Boyd, B. J., Simon, G. P. Extrusion and 3D printing of novel lipid-polymer blends for oral drug applications. *Biomaterials Advances* **137**, 212818 (2022).
57. Hoppe, P. P., Krennrich, G. Bioavailability and potency of natural-source and all-racemic  $\alpha$ -tocopherol in the human: a dispute. *Eur J Nutr* **39**, 183–193 (2000).
58. Ocaliva <https://www.ema.europa.eu/en/documents/product->



- [information/ocaliva-epar-product-information\\_it.pdf](#)  
Accessed Mar. 13, 2023
59. Hag, L., Gras, S. L., Conn, C. E., Drummond, C. J. Lyotropic liquid crystal engineering moving beyond binary compositional space ordered nanostructured amphiphile self-assembly materials by design. *Chem Soc Rev* **46**, 2705-2731(2017).
  60. Zidan, A., Alayoubi, A., Coburn, J., Asfari, S., Ghamraoui, B., Cruz, C. N., Ashraf, M. Extrudability analysis of drug loaded pastes for 3D printing of modified release tablets. *Int J Pharm* **554**, 292–301 (2019).
  61. Mendoza, M., Caselli, L., Montis, C., Orazzini, S., Carretti, E., Baglioni, P., Berti, D. Inorganic nanoparticles modify the phase behavior and viscoelastic properties of non-lamellar lipid mesophases. *J Colloid Interface Sci* **541**, 329–338 (2019).
  62. Jones, J. L., Mcleish, T. C. B. Rheological Response of Surfactant Cubic Phases. *Langmuir* **11**, 785–792 (1995).
  63. Radiman, S., Toprakcioglu, C., McLeish, T. Rheological Study of Ternary Cubic Phases. *Langmuir* **10**, 61-67 (1994).
  64. Johnsson, M., Edwards, K. Phase Behavior and Aggregate Structure in Mixtures of Dioleoylphosphatidylethanolamine and Poly(Ethylene Glycol)-Lipids. *Biophys J* **80**, 313–323 (2001).
  65. Riethorst, D., Baatsen, P., Remijn, C., Mitra, A., Tack, J., Brouwers, J., Augustijns, P. An In-Depth View into Human Intestinal Fluid Colloids: Intersubject Variability in Relation to Composition. *Mol Pharm* **13(10)**, 3484-3493 (2016).
  66. De Campo, L., Yagmur, A., Sagalowicz, L., Leser, M. E., Watzke, H., Glatter, O. Reversible phase transitions in emulsified nanostructured lipid systems. *Langmuir* **20**, 5254–5261 (2004).
  67. Lupo, N., Steinbring, C., Friedl, J. D., Le-Vinh, B., Bernkop-Schnürch, A. Impact of bile salts and a medium chain fatty acid on the physical properties of self-emulsifying drug delivery systems. *Drug Dev Ind Pharm* **47**, 22–35 (2021).
  68. Boyd, B. J., Khoo, S. M., Whittaker, D. v., Davey, G., Porter, C. J. H. A lipid-based liquid crystalline matrix that provides sustained release and enhanced oral bioavailability for a model poorly water soluble drug in rats. *Int J Pharm* **340**, 52–60 (2007).
  69. Lancaste ar al. United States Patent Patent No.: US 10,751,349 B2. Aug. 25, 2020.
  70. Lalde, R., Kaur, N., Duggirala, N. K., Suryanarayanan, R. Dual Functionality of Bile Acid: Physical Stabilization of Drugs in the Amorphous Form and Solubility Enhancement in Solution Published as part of a Molecular Pharmaceutics joint virtual special issue on Crystallizing the Role of Solid-State Form in Drug Delivery. *Mol. Pharmaceutics* **19**, 2595–2606 (2022).
  71. Atanacković, M., Poša, M., Heinle, H., Gojković-Bukarica, L., Cvejić, J. Solubilization of resveratrol in micellar solutions of different bile acids. *Colloids Surf B Biointerfaces* **72**, 148–154 (2009).

**Chapter 5**  
**Conclusions and Outlook**

Chronic inflammatory diseases are a major global health concern, accounting for more than 50% of all deaths worldwide. Inflammation is a complex process involving a cascade of immune responses that can result in chronic tissue damage and organ dysfunction. One of the consequences of prolonged or chronic inflammation is fibrosis, a progressive condition characterized by the deposition of extracellular matrix, which is responsible for around 45% of deaths in the global north. Despite the high mortality rates associated with fibrosis, only two drugs - pirfenidone (PFD) and nintedanib - have been approved as antifibrotics in Europe and the US, both for the management of idiopathic pulmonary fibrosis. Therefore, the development of drug delivery systems that can specifically target inflammation and fibrosis at the site of tissue damage holds immense promise for the treatment of chronic inflammatory diseases. This dissertation consists of three distinct research units each with its own set of findings. The first unit focuses on the development of a localized treatment for ulcerative colitis (UC). The second research unit presents a novel strategy for achieving ultrahigh drug loading of pirfenidone, along with the development of a localized treatment for intestinal fibrosis and endometriosis. The third and final unit of this dissertation investigates the utility of lipid mesophases as 3D printable ink for the manufacturing of solid oral dosage form, specifically for the treatment of liver fibrosis.

UC is a chronic inflammatory disorder of the large intestine. It always includes the rectal mucosa and may spread upwards in a continuous manner to involve partially or entirely the colon. Maximizing first-line rectal therapies to achieve high drug concentration at the site of inflammation might be a valuable strategy for both patients and healthcare providers. However, the efficacy of conventional enema-based formulations is limited by their low retention in the colon and the discomfort associated with administering large volumes. To address these drawbacks, a gel platform (TIF-Gel) was developed that uses rectal temperature as a trigger to form a highly viscous, water insoluble spongelike structure which adhere to the mucosa (**Chapter 2**). TIF-Gel is a lipidic mesophase based formulation loaded with two clinically relevant drugs, tofacitinib citrate and tacrolimus, and has been validated *in vivo* with two models of IBD. Results indicate that TIF-Gel can host and release drugs of different polarity in a sustained manner, and that rectal temperature can trigger the formation of the gel *in situ*. TIF-Gel adheres to the colon wall, and it is retained for 6 h, reducing leakage and systemic drug absorption and significantly local inflammation. Such a low systemic drug absorption indicates that TIF-Gel could be a suitable drug delivery platform for potent drugs, as it may minimize systemic toxicity. The results obtained from preclinical studies conducted on TIF-Gel have been utilized as a strong scientific foundation to file a European patent Euro (No 22197842.3). In order to enhance the clinical translation of TIF-Gel, I suggest conducting further evaluations of its local efficacy in larger animals with similar gastrointestinal transit times to humans, such as minipigs. This

will serve as the next step towards achieving a more decisive clinical translation of TIF-Gel. To accomplish this, it is imperative to scale up the manufacturing process in order to ensure the correct doses required for the next preclinical study while minimizing variability between batches. Therefore, a robust and reproducible preparation must be developed to achieve this goal. One approach is to create the less viscous precursor immediately prior to administration using a dual syringe system. The first syringe would contain the molten lipid doped with the drug. While the second syringe would be loaded with the necessary volume of water, and just before application, the two syringes could be connected to form the gel. To further simplify this step of the scale-up process, one possible approach would be to validate the addition of the drug directly into the molten lipid, which would eliminate the lyophilization step. Furthermore, to expand the range of applications for TIF-Gel, it would be worthwhile to investigate subcutaneous administration for the development of alternative treatments such as extended-release drug delivery systems for female contraceptives and chronic pain.

Effective antifibrotic therapies represent a critically important unmet need. Investigational use of PFD across various organs showed promising results. Since fibrotic diseases share common mechanisms and pathways, drug repurposing may offer a viable approach for treating a range of fibrotic diseases. To address this unmet need, in **Chapter 3** of this thesis, we aimed to develop a local delivery system for PFD in order to deliver the drug directly to the fibrotic site, reducing systemic exposure and collateral or end-organ adverse effects. Firstly, we were able to develop ultra-high concentrated PFD-loaded liposomes. Later, we successfully formed multiple-layered liposomes using layer-by-layer (LbL) electrostatic deposition technique with commercially available biopolymers without the need for purification steps. We rapidly fabricated an alginate hydrogel cross-linked by zinc chloride with a potential mucoadhesive property. Lastly, we produced a LbL liposomal gel releasing PFD in a sustained and tunable manner ranging from hours to several days by tuning the layer thickness. I propose two areas of investigation for future research. Firstly, an exploration of the underlying mechanisms that enable the remarkable ultrahigh drug loading achieved with PFD could potentially pave the way for increasing the drug loading of other drugs in liposome-based technology. Secondly, a validation of the efficacy of the local delivery system could be conducted through *in vivo* fibrotic animal models. The lack of reliable animal models for intestinal fibrosis and endpoints for clinical trials present significant obstacles to research. However, the efficacy of the formulation can be tested in various animal models, for example those that induce intestinal fibrosis through chemical factors (e.g., the skin bleomycin model), ischemia (e.g., bowel transplantation model), and thermal (e.g., swine GI stricture model). Although these models are not perfect surrogates for fibrosis in the gastrointestinal tract, they establish a crucial foundation for future investigations.

**Chapter 4** of this thesis focused on the development of a lipid-based oral dosage form for the treatment of hepatic fibrosis. Lipid-based formulations offer an attractive approach for enhancing the oral bioavailability of lipophilic and water-insoluble drugs. Lipid-based tablets are preferred because they minimise issues related to capsule compatibility, handling, and portability, while also improving patient compliance and drug stability. However, developing solid lipid-based systems in tablet form has proven challenging due to the lack of flexibility of lipids required to produce stable and uniform tablets. To address these limitations, 3D-printing has emerged as a promising tool to overcome the constraints posed by conventional dosage forms. Our objective was to develop an oral lipid-based formulation delivering both a high content of lipids with antifibrotic properties and efficiently a water-insoluble drug through self-emulsification. To achieve this, we selected a lipid mixture, S80, which has demonstrated beneficial effects in hepatic fibrosis, and a water-insoluble drug, obeticholic acid, to assess solubility enhancement. By carefully controlling the ink composition, its rheology, and printing parameters, our approach has led to the identification and development of a printable lipid mesophase ink with a high percentage of pure lipid, S80, which possess flexural strength and rigidity suitable to produce 3D-printed oral dosage forms. Further, we were able to incorporate the drug into the printable lipid mesophase ink at a dose comparable to the marketed one. The 3D-printed tablets disintegrated in colloidal structures while increasing the solubility of the drug. To bridge the gap between formulation development and *in vivo* effect, I suggest further studies on a more in-depth investigation of drug precipitation in biorelevant media, along with a suitable lipid digestion study to predict the chances of *in vivo* precipitation from the formulation. A suitable approach could be coupling the *in vitro* lipolysis model with SAXS and WAXS to study the formation of liquid crystalline structures and to track solid-state and drug solubilization by monitoring drug-related diffraction peaks during digestion in real time. Additive manufacturing of lipid mesophases represents a promising new avenue for producing not only innovative dosage forms but also a wide range of other functional structures based on this material.

## Appendix

## *A1: Temperature-triggered in situ forming lipid mesophase gel for local treatment of ulcerative colitis*

### *A1.1: Dead volume of the syringe and cannula*

To calculate the dead volume of the syringe 1 ml: Injekt®-F (Fine Dosage) Luer Solo (Luer Slip) (Braun) with the cannula (size 20G, L × diam. 1.5 in. × 1.9 mm), the syringe was filled with different amount of formulation MLO + MilliQ water (84% lipid and 16% water) and the amount that came out of the syringe was recorded.

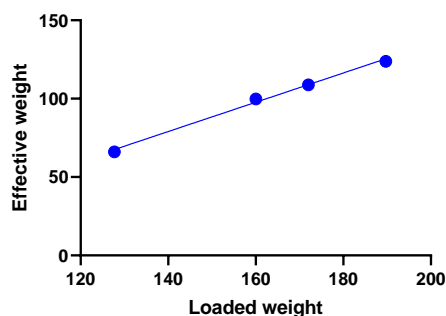


**Figure A1.1:** Calibration curve used to calculate the amount of formulation that has to be loaded into the syringe to obtain exactly 100 mg of formulation from the syringe with the cannula.

### *A1.2: HPLC method: Tofacitinib Citrate and Tacrolimus*

Tofacitinib citrate (TOFA) was detected by reverse-phase liquid chromatography using a Macherey-Nagel Nucleosil 100-5 C18 (4.0 x 250 mm; 5.0  $\mu\text{m}$  particle size) column. The mobile phase consisted of acetonitrile/methanol/water (13:13:74 v/v) + 0.1% trifluoroacetic acid at a flow rate of 1 mL/min, temperature 25 °C and UV detection at  $\lambda = 278$  nm. An internal standard (caffeine, 20  $\mu\text{g}/\text{mL}$ ) was added to each sample to correct for inter-injection variation and UV detection at  $\lambda = 278$  nm. Data were collected and analyzed using the software Chromeleon 7 (Thermo Fisher).

Tacrolimus (TAC) was detected by reverse-phase liquid chromatography using a Macherey-Nagel Nucleosil 100-5 C18 (4.0 x 250 mm; 5.0  $\mu\text{m}$  particle size) column. The mobile phase consisted of methanol/water (80:20 v/v) + 0.1% trifluoroacetic acid at a flow rate of 1 mL/min, temperature 50 °C and UV detection at  $\lambda = 214$  nm. An internal standard (ketoconazole, 20  $\mu\text{g}/\text{mL}$ ) was added to each sample to correct for inter-injection variation and UV detection at  $\lambda = 278$  nm. Data were collected and analyzed using the software Chromeleon 7 (Thermo Fisher).

### *A1.3: LC-MS/MS analysis*

Samples, standards and QC were extracted by protein precipitation and analyzed by LC-MS/MS using the following method. For plasma samples, 10  $\mu\text{L}$  of plasma was mixed with 25  $\mu\text{L}$  of precipitation

solution (80:20 Acetonitrile: Methanol + 0.1 $\mu$ M loperamide). The samples were centrifuged at 10000g for 10min and 20 $\mu$ L of supernatant was diluted with 40 $\mu$ L of H<sub>2</sub>O+0.1%FA. The samples were centrifuged at 3400rpm for 10min and 50 $\mu$ L of supernatant was diluted with 100 $\mu$ L of H<sub>2</sub>O+0.1%FA. All the samples were analyzed by LC-MS/MS (Shimadzu prominence HPLC coupled to an AB/SCIEX 4000 QTRAP) in positive MRM mode. The samples were separated on a Cortecs RP shield column (3x50mm 2.6 $\mu$ ) using a fast gradient of 10mM ammonium formate in water (A) and methanol (B). The gradient starts at 20%B and increases to 98%B in 2 minutes, hold for 0.5min and equilibrates for 1.4min. The MRM parameters were optimized for each analyte; the MRM transition 313. to 149.3 was selected for tofacitinib, 822.3 to 770.1 for tacrolimus and 477.1 to 266.0 for loperamide (internal standard). The samples were quantified using a calibration curve prepared in matrix using the area ration of analyte to internal standard.

#### A1.4: Reversibility of the transition

Small-angle X-ray scattering (SAXS) was used to determine the lipid phase, and thus the reversibility of the transition.

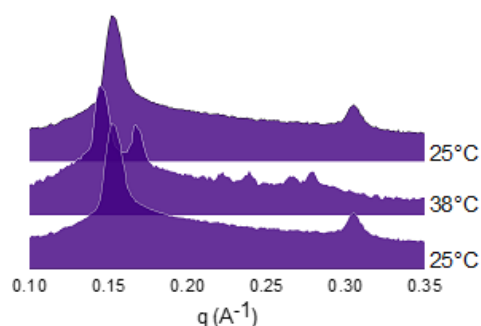


**Figure A1.4:** *In vitro* characterizations of the TIF-Gel: SAXS spectra acquired at different temperatures: at 25°C (bottom), after 30 minutes equilibration at 38°C (middle) and after 30 minutes equilibration at 25°C (top).

#### A1.5: Amplitude sweep experiments

A stress-controlled rheometer (Modular Compact Rheometer MCR 72 from Anton Paar, Graz, Austria) was used in cone-plate geometry, 0.993° angle and 49.942 mm diameter. The temperature control was set either at 25 or 38 °C. An amplitude sweep was performed at 1 Hz between 0.002 and 100% strain to determine the linear viscoelastic regime (LVR), the yield and flow points.



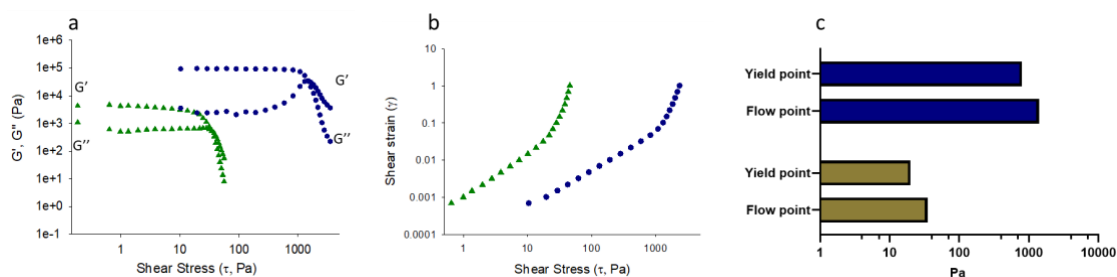


**Figure A1.5:** Amplitude sweep experiments acquired at 25°C (green symbols and bars) and at 38°C (blue symbols and bars) on empty gel. a) Storage moduli ( $G'$ ) and loss of moduli ( $G''$ ) are plotted versus the shear stress. The yield point is the value of the shear stress at the limit of the LVE region while the flow point is the value of the shear stress at the crossover point  $G' = G''$ . b) Shear strain is plotted versus the stress, and the yield point is exceeded at the point where the deformations start to deviate from linearity. c) The bar plots (also present in the main text as panel e in Figure 1) summarize the yield and flow point obtained from the amplitude sweep experiments.

*A1.6: In vivo/ex vivo experiments to evaluate the adhesion of the TIF-Gel to the colon wall*

For *in vivo* adhesion testing, healthy animals ( $n= 11$ ) received an enema of 100 ml DiR (1,1'-dioctadecyl-3,3,3',3'-tetramethylindotricarbocyanine iodide) loaded gel (DiR-TIF-Gel) under anesthesia as described in the experimental section. Animals were sacrificed after 30 minutes ( $n= 3$ ), 2 and 6 hours ( $n=4$ ). The distal 3 cm of the colon (including the rectum) was harvested and freshly imaged after a gentle washing with PBS. Intensity of the fluorescent signal was measured using the IVIS SpectrumCT *In Vivo* Imaging System (PerkinElmer, MA, US). DiR fluorescent signal (excitation 754 nm, emission 778 nm) was detected in the distal part of dissected colons at 3 time points post gel injection. An untreated control mouse was included in each measurement ( $n=3$ ). Acquired images were analysed using the Living Image® software (PerkinElmer, MA, US). Backgrounds (untreated tissue samples) were measured for each time point. Obtained signal was analysed as radiant efficiency (RE), which is a calibrated unit that compensates for device settings and non-uniform light excitation pattern.

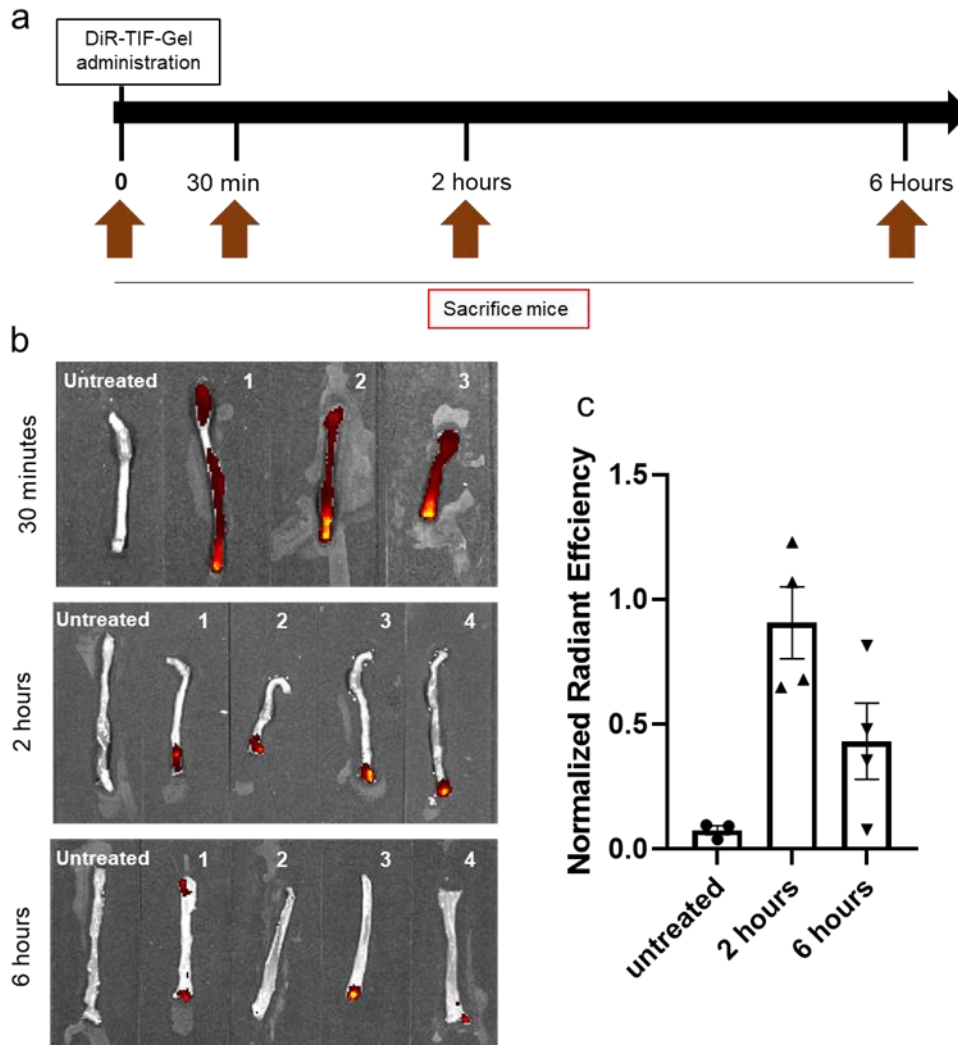


**Figure A1.6:** The TIF-Gel adheres to healthy colonic tissue for at least 6 hours. a) Experimental scheme: Healthy animals received an enema of 100 mL of DiR-TIF-Gel. Animals were sacrificed after 30 min, 2 and 6 h and the colon was harvested and imaged (b). c) The obtained signal was analysed as radiant efficiency (RE), which was normalized to radiant efficacy recorded at 30 min.

#### A1.7: Phase transition identification after *in vivo* applications

Healthy animals were administered with 100 mL of TIF-Gel and either the excreted gel (with stool after 30 min) or the residual gel present in the colon after 6 h was collected and analyzed by SAXS (the animal was sacrificed, colon harvested, and the residual gel washed 3x with PBS before analysis). As shown in Fig. S3, the Bragg reflections characteristic of L phase were present before administration at 25 °C, whereas the gel excreted with the stool showed the L → Ia3d transition. Moreover, the lamellar phase absorbed heat and water during the experiment reaching a cubic (pn3m) phase as was already observed in the *in vitro* investigations.

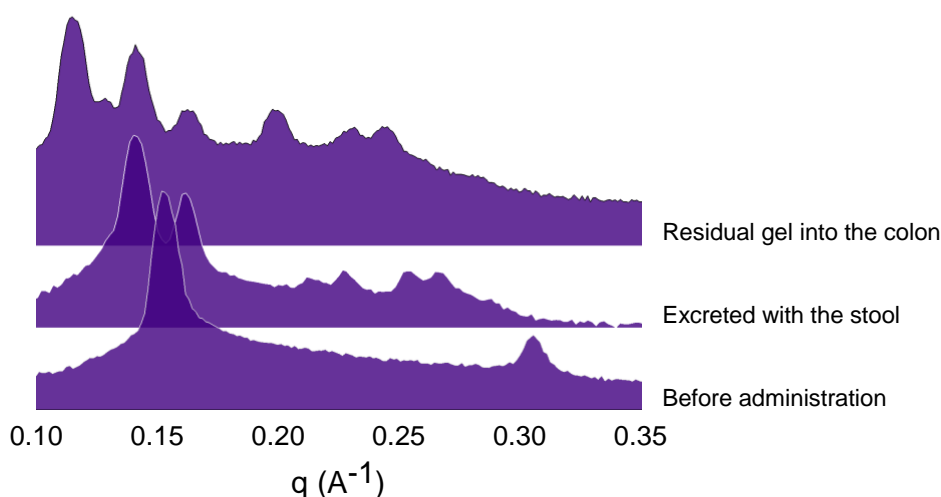


**Figure A1.7:** *In vivo* characterization of the TIF-Gel: SAXS spectra acquired at different time points (before administration, excreted with the stool, and the residual gel present in the colon) at 38 °C.

#### A1.8: Gels' phase identity with 10 % w/w amounts of drugs

Measurements were performed on a Bruker AXS Micro, as described in the main text. MLO was used as the lipid component of the mesophases and mixed with weighed amounts of drugs (10% w/w) in sealed Pyrex tubes and alternatively centrifuging (10 min, 5000 g) several times at room temperature until a homogenous mixture was obtained. The mesophase was then equilibrated for 48 h at room temperature.

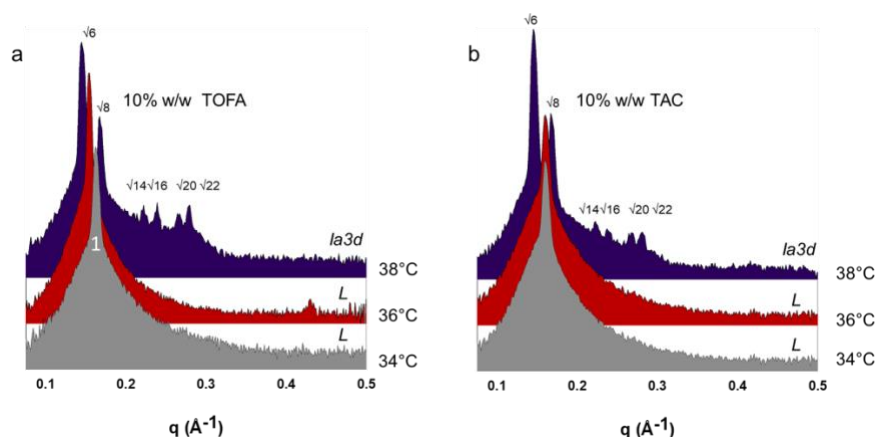


**Figure A1.8:** SAXS spectra acquired at different temperatures on gels containing 10% w/w of TOFA (a) and 10% w/w of TAC (b).

#### A1.9: Drug homogeneity into the gel structures

Both drugs are dissolved into the gel matrix and they do not form crystals once incorporated into the lipidic gel (at least at the drug concentrations used in this study), as proven by the absence of reflections associated with a drug crystallization in the WAXS spectra at high  $q$  (see Figure S4, panel

a). We carried out additional experiments to assess whether both drugs were homogeneously distributed into the gel matrix. To determine this, the gel (loaded with TAC or TOFA) was prepared as described in the manuscript and transferred into a 2 mL Eppendorf tube. The tube was centrifuged and kept at rest for 24 hours. Subsequently, the gel was divided into 3 different layers (Top, Middle, and Bottom), and the drug content evaluated in each. As shown in Figure S4 (panel b), each layer contains the same drug amount, confirming that TOFA and TAC were homogeneously distributed.

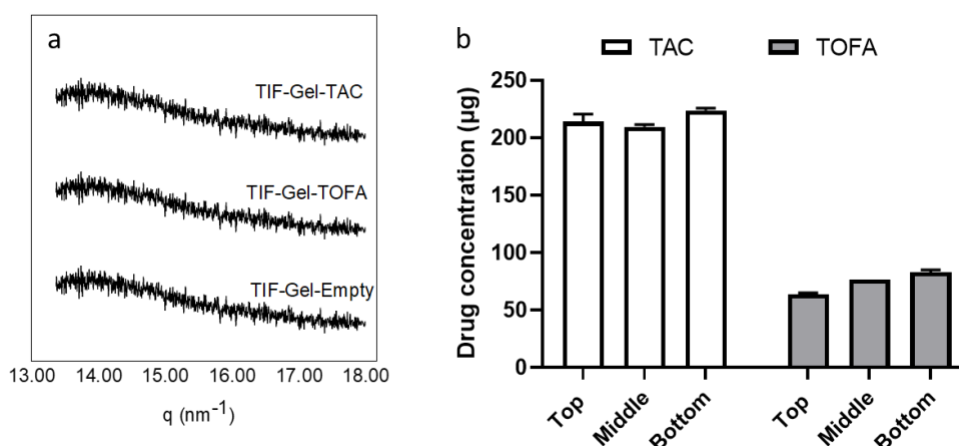


**Figure A1.9:** Drugs distribution into TIF-Gel. a) WAXS spectra obtained for empty gel (bottom), TOFA loaded gel (middle) and TAC loaded-gel (top). All the WAXS spectra (acquired for 30 minutes at 25°C) show only a broad shoulder (and no evident peak) which indicates the amorphous state of the lipidic chain and the absence of crystalline structures. b) Homogeneity of drugs in the gel. The amount of drug present in 3 different gel layers (Top, Middle and Bottom) was evaluated by HPLC.

#### A1.10: Stability Study of TAC and TOFA

The stability of the drugs – TOFA and TAC – was monitored over one month. At specific time points, an aliquot of the formulation was analyzed at the HPLC, and the content of the drug recorded. Data are expressed as relative percentage referred to day 0.

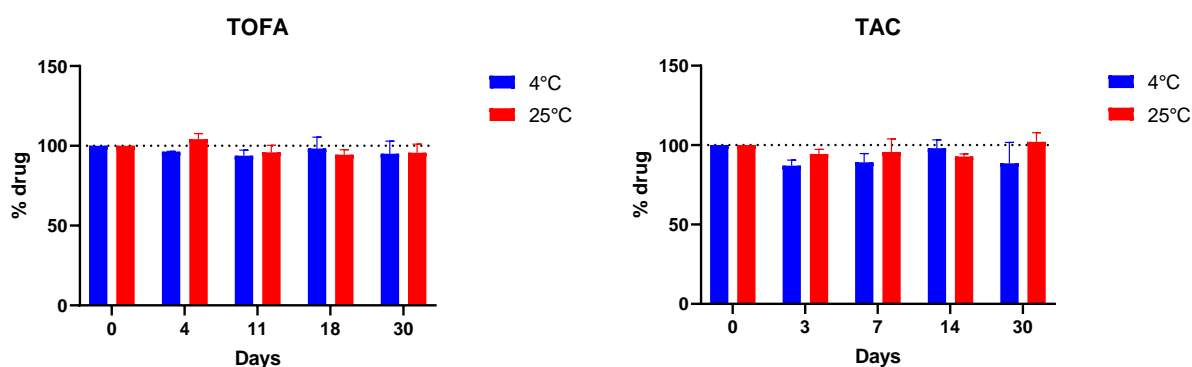


**Figure A1.10:** Long-term stability of TOFA loaded into TIF-gel and TAC loaded into TIF-gel over one month. Data are expressed as percentage  $\pm$  SD.

### A1.11: Stability study of TIF-Gel

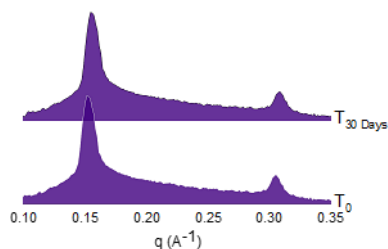


**Figure A1.11:** The lamellar geometry obtained immediately after the preparation of the gel does not change after 30 days of storage. *In vitro* characterizations of the TIF-Gel: SAXS spectra acquired at 25 °C immediately after the preparation ( $T_0$ ) and after 30 days ( $T_{30 \text{ days}}$ ). The calculated lattice parameters at  $T_0$  and  $T_{30 \text{ Days}}$  are 4.8 and 4.6 nm, respectively. The slight decrease in the measured lattice parameter can be explained by the loss of a minimal amount of water from the sample which was stored in a 2 mL microcentrifuge conical tube.

### A1.12: Daily application of TIF-Gel-TOFA

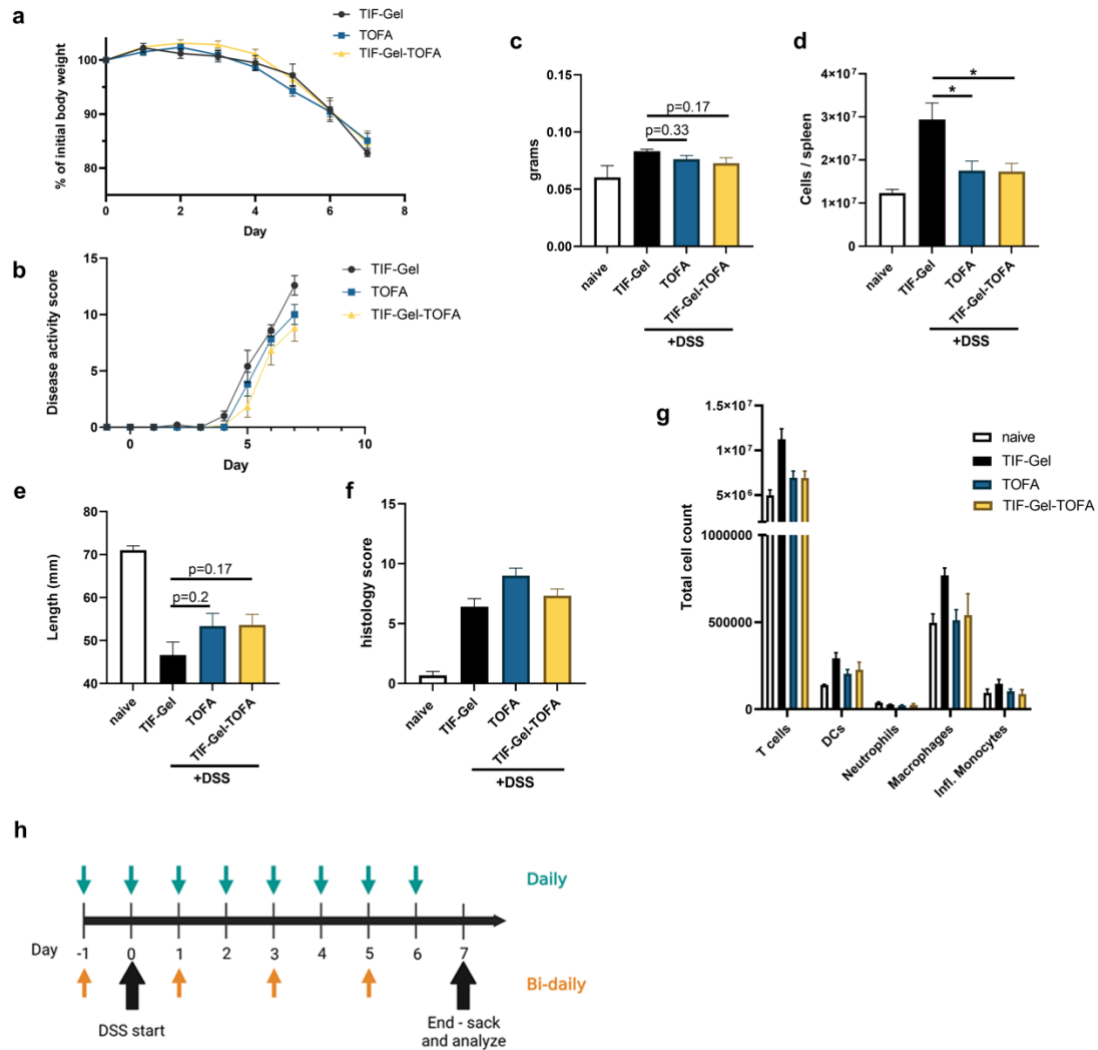
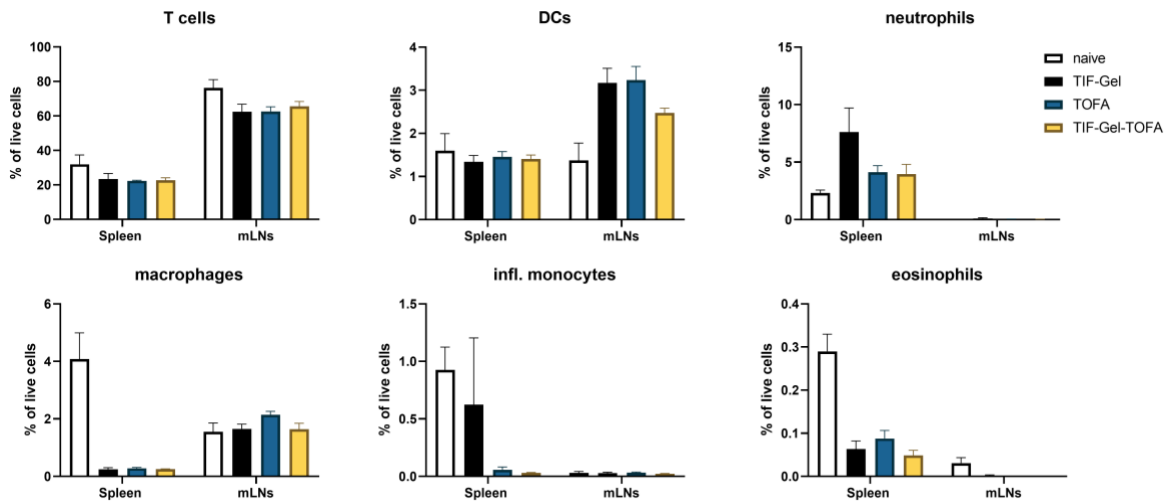


**Figure A1.12:** Daily application of TIF-Gel-TOFA did not improve animal health compared to TOFA in vehicle. Mice were treated rectally with empty gel (TIF-gel), TOFA in vehicle (TOFA) or drug-loaded gel (TIF-Gel-TOFA) daily from 1 day before the start of DSS treatment until day 6). During the treatment, mice were weighed (a), and the severity of their illness was assessed (b). At day 7, mice were euthanized, and various disease parameters were recorded included spleen weight and cellularity (c and d), colon length and pathology (e and f), and the total populations of various immune cells from spleens were calculated (g). h) An application scheme detailing the timeline for the daily and bi-daily rectal applications of the various compounds. Statistical values were calculated by one-way ANOVA (c, d, e, f), multiple T tests per group with Holm-Sidak correction (g) or two-way ANOVA (a and b). \*:  $p < 0.05$ , where no value is indicated,  $p > 0.05$ . Naïve values were excluded from analyses. Error bars are  $\pm$  SEM.



TIF-gel-TOFA does not rescue the changes to cell frequencies of spleen and mLN in DSS-treated mice. The relative numbers of various cell types in mouse spleens and mesenteric lymph nodes (mLNs) were quantified. No statistically significant differences in percentages were observed between the different treatment groups. Data were analyzed using one-way ANOVAs. DCs, dendritic cells. Error bars are  $\pm$  SEM.

## A2: Composite layer-by-layer liposomal gel for mucosal delivery of pirfenidone

### Preparation of biopolymer solutions

For the coating of liposomes, 50 mM acetate buffer solution was prepared with sodium acetate trihydrate in distilled water. The pH value of the acetate buffer solution was adjusted to 5.5 using glacial acetic acid. The buffer was then used to prepare 2% (w/v) stock solutions of chitosan (CHI) and alginate (ALG) by dissolving and stirring for 24 h to ensure a homogenous dispersion. Stock solutions of biopolymers were then diluted with acetate buffer (50 mM) to prepare a range of concentrations (0.01 to 0.1% w/v) that would be then used for the coating of liposomes. For the ALG hydrogel, the alginate was dissolved in 30 mM HEPES (pH 7.4) to have a final 5% (w/v) concentration.

### A2.1: Concentrations of biopolymer used for the preparation of LbL-LIP

Prior to the subsequent biopolymer's deposition, an experiment was performed to determine the concentration needed to ensure a complete liposomal coating. Z-potential was used to monitor the change in surface charge.

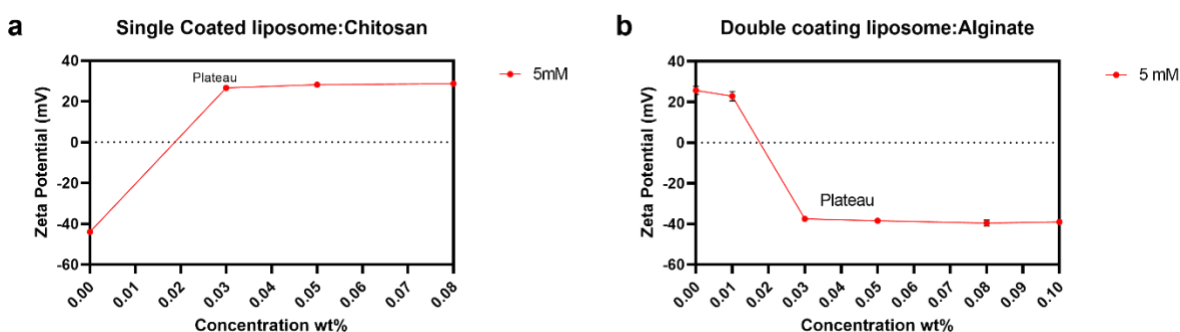


**Figure A2.1:** Liposomes are diluted to 0.5 mM with pure water to avoid multiple scattering effects. Panel a) increasing concentration of CHI on PFD-liposomes; panel b) increasing concentration of ALG on single coated PFD-liposomes with CHI. Data are presented as mean  $\pm$ SD (n=3).

Increasing concentrations of ALG and CHI were tested and the value 0.04 wt% was chosen. This value had previously been shown to be equivalent to the saturation concentration, i.e., the concentration where the charge of the interface was completely reversed since the interface had been fully covered by the next biopolymer.<sup>1</sup>

### A2.2: Purification method

Free PFD was removed by dialysis with a Slide-A-Lizer MINI Dialysis device (Thermo Scientific; MW cutoff 20 MWCO) against 45 mL of acetate buffer 30 mM, pH 5.5 at room temperature. To determine the dialysis time needed to remove the free drug, aliquots after specific timepoints (1, 2, 4



and 24 h) were collected and analysed via HPLC. Data were collected and analyzed using the software Chromeleon 7 (Thermo Fisher). Further experiments were performed by using a dialysis time of 2 h.

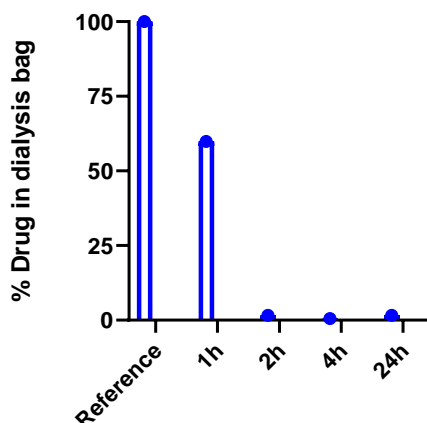


**Figure A2.2:** Determination of PFD in the dialysis bag after specific timepoints.

#### A2.3: UHPLC-CAD method for lipid

The method was previously developed by our group.<sup>2</sup> The instrument (Ultimate 3000, Thermo Fisher Scientific, Switzerland) was equipped with a quaternary pump (LPG-3400SD), an autosampler (WPS-3000), a thermostatted column compartment (TCC-3000), a DAD (DAD-3000) and a CAD (Corona Veo RS). A hypersil Gold™ (C18, 150 x 2.1 mm) with a particle size of 1.9  $\mu\text{m}$  and a pore size of 175 Å (Thermo Fisher Scientific, Switzerland) was used at a temperature of 50°C. The injection volume was 5  $\mu\text{L}$  and the flow rate at 0.7  $\text{mL min}^{-1}$ . Three different eluents, eluent A: acetonitrile +0.2% v/v trifluoroacetic acid (TFA), eluent B: methanol (MeOH) +0.2% v/v TFA and eluent C: ultrapure water +0.2% v/v TFA were used to create a linear gradient in the mobile phase. The analysis started with 35% eluent A, 50% eluent B and 15% eluent C at time point 0 min. After 20 min, the mobile phase was composed of 5% eluent A and 95% eluent B and kept constant for 1.5 min. At 23 min, the composition of eluents was brought back to the initial state and the column was equilibrated for additional 3 min. For the Corona Veo RS, the gas evaporation temperature was adjusted to 45 °C and the response rate was set to 100 pA. Data were collected and analyzed using the software Chromeleon 7 (Thermo Fisher).

#### A2.4: Membrane selection for *in vitro* release studies

To determine the membrane to use during the *in vitro* release studies, a preliminary experiment using a 3000 nm polycarbonate membrane (Sterlitech Corporation, USA) was carried out. As shown in figure A2.4, a solution of free PFD reaches approximately 100% within 3 h. Further release study experiments were carried out using the mentioned membrane.

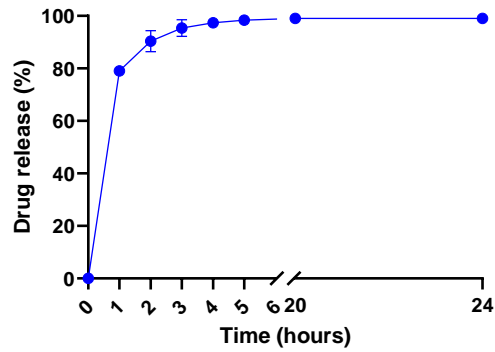


**Figure A2.4:** Release study of a solution of free PFD using a 3000 nm polycarbonate membrane. Data are shown as mean  $\pm$ SD (n=3).

#### A2.5: Release studies of PFD-liposomes and free PFD-Gel

As shown in figure A2.5, release studies of PFD-liposomes and free PFD-gel are comparable to the free-PFD's profile. These results highlight the fact that PFD has weak interaction with alginate hydrogel and liposomes.

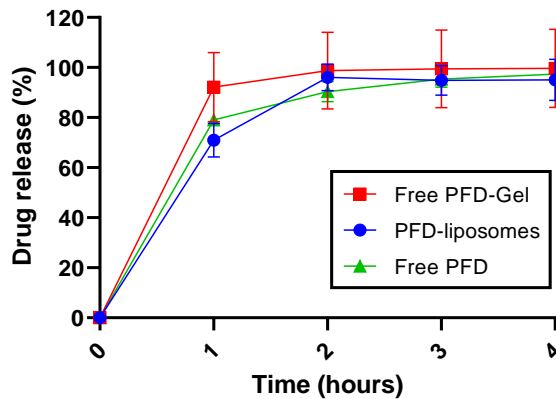


**Figure A2.5:** Release study of free PFD, PFD-liposomes, and free PFD-Gel. Results are shown as mean  $\pm$  SD (n=3).

#### A2.6: Amplitude Sweep

The amplitude sweep describes the deformation behaviour of samples in the non-destructive deformation range and determine the upper limit of this range. For amplitude sweeps, the amplitude is increased stepwise while keeping the frequency at a constant value. An angular frequency of  $\omega = 10$  rad/s is used. The linear viscoelastic region is the range in which the test can be carried out without destroying the structure of the sample. As shown in figure A2.6, storage modulus  $G'$  and loss modulus  $G''$  show a constant value, the so-called plateau value. For the next frequency tests, the measurements are carried out at strain levels within the linear viscoelastic region.

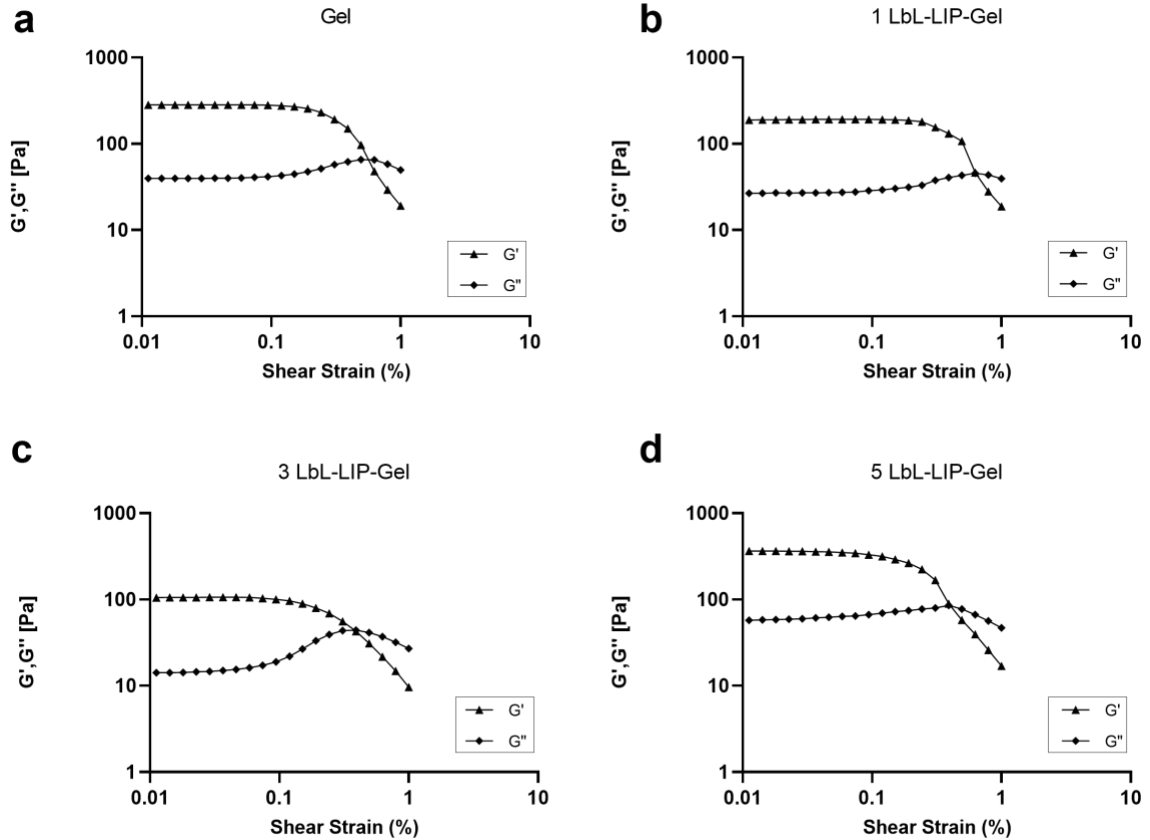


**Figure A2.6:** Amplitude sweeps of a) ALG gel; b) 1 LbL-LIP-Gel; c) 3 LbL-LIP-Gel; d) 5 LbL-LIP-Gel. The results are presented as a diagram with shear strain plotted on the x-axis and storage modulus  $G'$  and loss modulus  $G''$  plotted on the y-axis; both on a logarithmic scale.

### A2.7: Controls of *in vitro* release studies

Several controls were carried out to confirm that the layer-by-layer strategy was necessary for the final *in vitro* release studies. As shown in figure A2.7, PFD release studies are comparable to the free PFD's profile and the presence of ALG and CHI – at the same concentration used during the LbL-LIPs formation- doesn't affect the drug release. In conclusion, the subsequent deposition of CHI and ALG on the liposomes' surface is a necessary step for the controlled release of PFD.

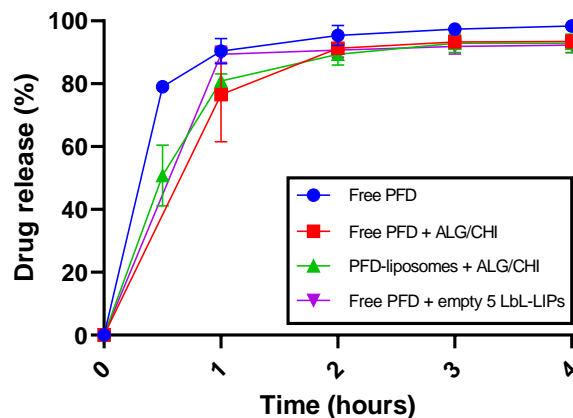


**Figure A2.7:** Release study of free PFD, free PFD in presence of alginate and chitosan, PFD-liposomes in presence of alginate and chitosan and free PFD in presence of empty 5 LbL-LIPs. Results are presented as mean  $\pm$ SD (n=3).

### A3: Design and use of 3D-printable lipid mesophase as oral dosage form

Table A3.1: Formulation screening of the water content

We systematically screened different formulations by varying one critical parameter at a time, namely the water or tocopherol content, and evaluated their printability and shape retention as key criteria for selection. Subsequently, a single formulation was identified as optimal and selected for further analysis.

Formula Code	Water content (%)	$\alpha_{oil}$	Printing temperature	printability	Shape retention
F1	10	0.35	25	no	-
F2	15	0.35	25	yes	no
F3	20	0.35	25	yes	<i>Optimization needed*</i>
F4	25	0.35	25	yes	no
F5	30	0.35	25	yes	no
F6	35	0.35	25	no	-
F7	40	0.35	25	no	-
F8	45	0.35	25	no	-

\* *Shape retention improved, but more optimization is required.*

Table A3.2: Formulation screening of the tocopherol content

Formula Code	Water content (%)	$\alpha_{oil}$	Printing temperature	printability	Shape retention
F9	20	0.15	25	yes	yes
F10	20	0.20	25	yes	<i>Optimization needed*</i>
F11	20	0.25	25	yes	<i>Optimization needed*</i>
F12	20	0.30	25	yes	<i>Optimization needed*</i>
F13	20	0.35	25	yes	<i>Optimization needed*</i>
F14	20	0.40	25	no	-

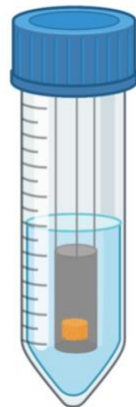
\* *Shape retention improved, but more optimization is required.*

Figure A3.1: Representation of 3D-printed tablets during lipid mesophase ink optimization



Figure A3.1: 3D-printed tablets depicted in the figure are representative of the lipid mesophase ink detailed in Table A3.2.

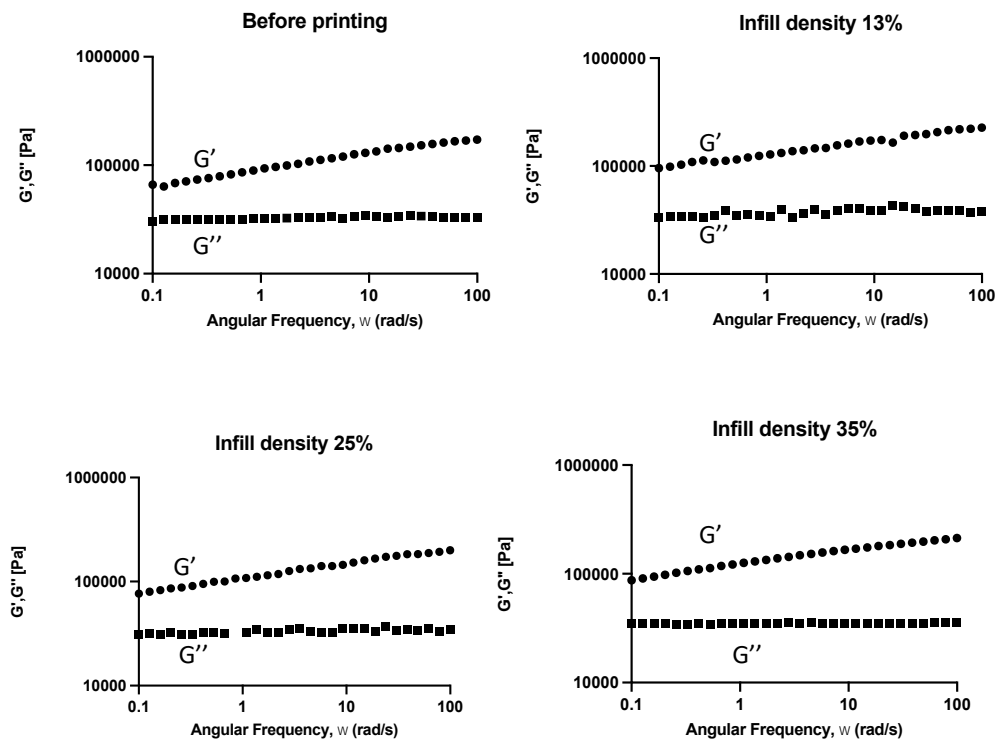
Figure A3.2: Experimental setup for assessment of self-emulsification adapted from Karfeld-Sulzer et al.<sup>3</sup>



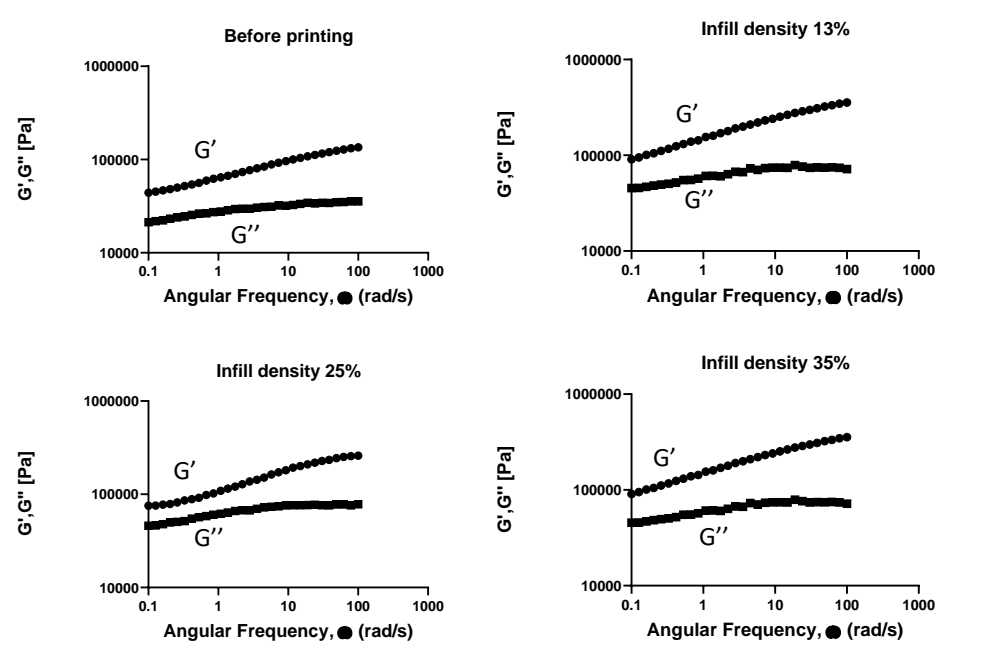
- 50 mL tube
- Custom-made metallic basket

Figure A3.3: Frequency sweeps of lipid mesophase inks and 3D-printed tablets

(a)



(b)



**Figure A3.3:**(a) shows the frequency sweep results of 3D-printed ink samples before and after printing at different infill densities, while Figure A3.3(b) displays the frequency sweep outcomes of OA-3D-printed ink samples before and after printing at varying infill densities.

*Figure A3.4: Assessment of self-emulsification*

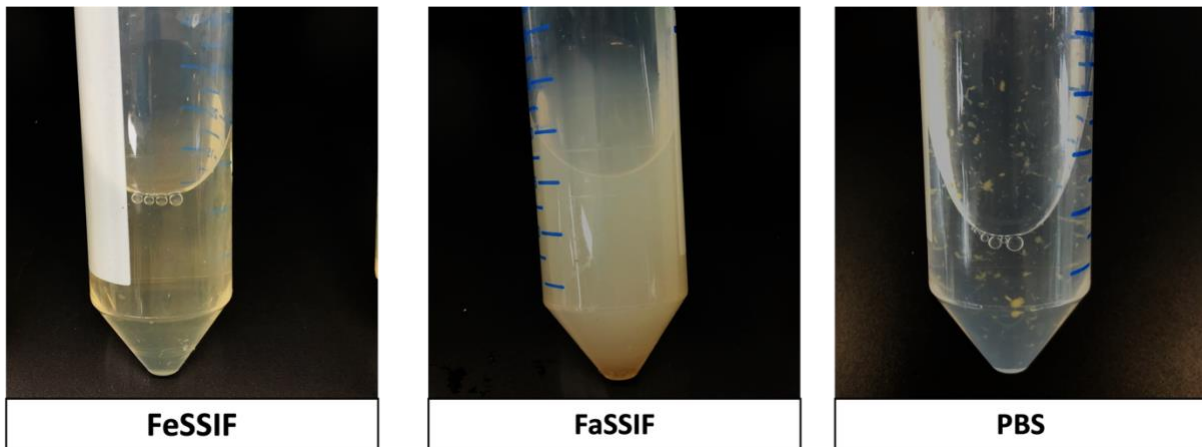


**Figure A3.4:** A qualitative evaluation was performed to assess the self-emulsification in FeSSIF, FaSSIF and PBS after a period of 2h.

*Figure A3.5: Visual assessment of inverse hexagonal and lamellar phase in PBS*

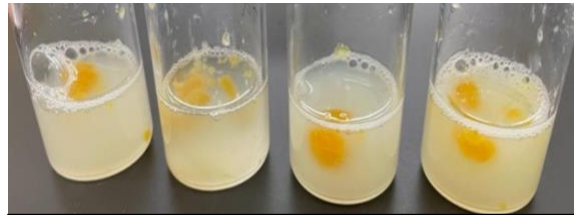
In the table is indicated the composition of the inverse hexagonal and lamellar phase used for this study.

<b>Surfactant</b>	<b>Oil</b>	<b><math>\alpha</math> oil</b>	<b>Water content (wt.%)</b>	<b>Phase</b>
S80	Tocopherol	25	15	Hexagonal
<b>S80</b>	<b>Tocopherol</b>	<b>12</b>	<b>20</b>	<b>Hexagonal + Lamellar</b>
S80	--	--	20	Lamellar

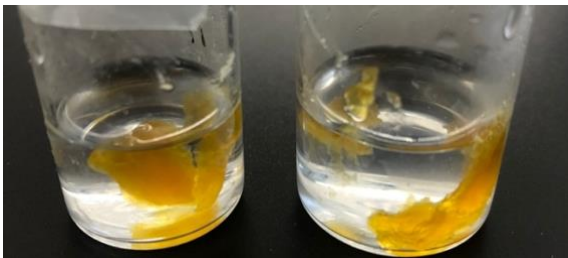




T 0: inverse hexagonal phase



T 0: lamellar phase



T 24: inverse hexagonal phase



T 24: lamellar phase

## References

1. Chun, J., Choi, M., Min, S.G., Weiss, J. Formation and stability of multiple-layered liposomes by layer-by-layer electrostatic deposition of biopolymers. *Food Hydrocoll* **30(1)**, 249-257 (2013).
2. Weber, F., Rahmfeld, L., Luciani, P. Analytical profiling and stability evaluation of liposomal drug delivery systems: A rapid UHPLC-CAD-based approach for phospholipids in research and quality control. *Talanta* **220(1)**, 121320 (2020).
3. Karfeld-Sulzer, L. S., Ghayor, C., Siegenthaler, B., de Wild, M., Leroux, J. C., Weber, F. E. N-methyl pyrrolidone/bone morphogenetic protein-2 double delivery with in situ forming implants. *J Control Release* **203**, 181-188 (2015).

## Abbreviations

<b>ALG</b> alginate	<b>H</b> inverse hexagonal
<b>5-ASA</b> 5-aminoalicylic acid	<b>IND</b> investigational new drug
<b>AUC</b> area under the curve	<b>IBD</b> Inflammatory Bowel Disease
<b>CPP</b> critical packing parameter	<b>LUV</b> large unilamellar vesicles
<b>CHI</b> chitosan	<b>L<math>\alpha</math></b> lamellar
<b>DPPC</b> 1,2-dipalmitoyl- <i>sn</i> -glycero-3-phosphocholine	<b>LbL</b> layer-by-layer
<b>DSPG</b> 1,2-distearoyl- <i>sn</i> -glycero-3-phospho-(10- <i>rac</i> -glycerol) sodium salt	<b>LbL-LIPs</b> layer-by-layer liposomes
<b>DiD</b> 1,1'-dioctadecyl-3,3,3',3'-tetramethylindodicarbocyanine, 4-chlorobenzenesulfonate salt	<b>LbL-LIP-Gel</b> layer-by-layer liposomal gel
<b>DL</b> drug loading	<b>LVE</b> linear viscoelastic region
<b>DLS</b> dynamic light scattering	<b>LMP</b> lipidic mesophase
<b>DSS</b> dextran sodium sulfate	<b>MLO</b> monolinolein
<b>FaSSIF</b> fasted state simulated intestinal fluid	<b>MLV</b> multilamellar vesicle
<b>FeSSIF</b> fed state simulated intestinal fluid	<b>MVV</b> multivesicular vesicle
<b>GRAS</b> generally recognized as safe	<b>MVD<sup>+</sup></b> methyl viologen dichloride
<b>GIT</b> gastrointestinal tract	<b>NASH</b> nonalcoholic steatohepatitis
<b>G'</b> storage modulus	<b>OA</b> obeticholic acid
<b>G''</b> loss modulus	<b>OA-printlet</b> 3D-printed tablets with OA
<b>GRAS</b> Generally Recognized as Safe	<b>PEG</b> polyethylene glycol
<b>GUV</b> giant unilamellar vesicles	<b>PVA</b> polyvinyl acetate
	<b>PBS</b> phosphate buffer saline
	<b>PFD</b> pirfenidone
	<b>Printlets</b> 3D-printed tablets
	<b>PPC</b> polyenylphosphatidylcholine

**Q** inverse cubic

**SSE** semi solid extrusion

**S80** Soybean phospholipid with 75%  
polyenylphosphatidylcholines

**SUV** small unilamellar vesicles

**SAXS** small angle X ray

**TOFA** tofacitinib

**TAC** tacrolimus

**TIF-Gel** temperature triggered in situ  
forming gel

**THF** tetrahydrofuran

**UC** ulcerative colitis

## Declaration of consent

on the basis of Article 18 of the PromR Phil.-nat. 19

Name/First Name: Marianna Carone

Registration Number: 19-136-704

Study program: Chemistry and molecular sciences

Bachelor

Master

Dissertation

Title of the thesis: Lipid-based drug delivery systems for inflammatory and fibrosis therapies

Supervisor: Prof. Dr. Paola Luciani

I declare herewith that this thesis is my own work and that I have not used any sources other than those stated. I have indicated the adoption of quotations as well as thoughts taken from other authors as such in the thesis. I am aware that the Senate pursuant to Article 36 paragraph 1 litera r of the University Act of September 5th, 1996 and Article 69 of the University Statute of June 7th, 2011 is authorized to revoke the doctoral degree awarded on the basis of this thesis.

For the purposes of evaluation and verification of compliance with the declaration of originality and the regulations governing plagiarism, I hereby grant the University of Bern the right to process my personal data and to perform the acts of use this requires, in particular, to reproduce the written thesis and to store it permanently in a database, and to use said database, or to make said database available, to enable comparison with theses submitted by others.

Bern, 20/02/2023

Place/Date

Signature

*Marianna Carone*